



DISSERTATION

Investigation of the electron momentum density of solids by electron energy loss spectroscopy

ausgeführt zum Zwecke der Erlangung des akademischen Grades eines
Doktors der technischen Wissenschaften
unter der Leitung von

Univ. Prof. Peter Schattschneider

E138
Institut für Festkörperphysik

Eingereicht an der
Technischen Universität Wien
Fakultät für Physik

von

Dipl.-Ing. Zhenbao Feng

e1028917
Quellenstraße 128/13
A-1100 Wien

Wien, im December 2013

Kurzfassung

Elektronen-Energieverlustspektroskopie der Kantenfeinstruktur (ELNES – electron energy loss near edge structure) ist eine nützliche Methode zur Untersuchung der elektronischen Struktur unbesetzter Zustände. Elektronen-Energieverlustspektroskopie im Bereich hoher Energieverluste und großer Impulsüberträge – Elektronencomptonstreuung an Festkörpern (ECOSS – electron Compton scattering on solids) ist eine einzigartige Technik, um die Impulsdichteverteilung des elektronischen Grundzustandes in einem Material zu bestimmen. Beide Techniken können in einem Experiment angewendet werden. Diese Arbeit behandelt die experimentelle und theoretische Untersuchung von Energieverlustspektren mit Bezug auf diese beiden Aspekte.

Die Verwendung von Elektronen anstelle von Photonen in der Comptonstreuung, um Impulsdichteverteilungen in Atomen und Molekülen zu bestimmen, geht auf das Jahr 1938 zurück, als Elektronen-Comptonstreuexperimente erstmals an Gasen durchgeführt wurden. 1981 wurde von Williams et al. gezeigt, dass Elektronen-Comptonstreuung im Elektronenmikroskop an Festkörpern durchgeführt werden kann. Die schwerwiegendsten Probleme mit dieser Technik waren Mehrfachstreuung, Bragg-Beugung und das extrem schwache Comptonssignal. Die instrumentellen Verbesserungen der letzten Jahre bezüglich Auflösung, statistischer Genauigkeit und Reproduzierbarkeit ermöglichen es heute, Experimente durchzuführen, die vor einem Jahrzehnt nicht möglich gewesen wären. In modernen Elektronenmikroskopen kann ein Comptonprofil innerhalb von einigen zehn Sekunden aufgenommen werden, während dies vor 20 Jahren noch einige hundert Sekunden erforderte. Desgleichen wurden die numerischen Methoden zum Untergrundabzug wesentlich verbessert. Diese Fortschritte rechtfertigen eine Neubelebung der ECOSS-Technik.

Die Vorteile, Compton-Profile in sehr kurzer Zeit aufzunehmen, sind offensichtlich. Neue systematische Studien der Impulsdichteverteilung und der elektronischen Struktur technologisch interessanter Materialien werden ermöglicht. Mit den kurzen Aufnahmezeiten und der verbesserten Energie- und Ortsauflösung und Statistik können Comptonprofile in Abhängigkeit von Kristallorientierung, Zusammensetzung und Temperatur gemessen werden. In dieser Arbeit werden ELNES- und ECOSS-Spektren von Silizium (kubisch), Graphit (hexagonal) und amorphen Kohlefilmen im Elektronenmikroskop systematisch untersucht, wobei der Streuwinkel variiert wird. Die Abhängigkeit der ECOSS-Spektren vom Impulsübertrag wurde im Bereich 6.0 bis 9.0 atomaren Einheiten untersucht. Das primär interessierende Profil der Valenzelektronen wurde durch Abzug der Beiträge der inneren Schalen gewonnen, welche in einer Hartree-Slater Näherung theoretisch berechnet wurden. Die Elektronen-Comptonsspektren stimmen gut mit konventionellen Photon-Comptonsspektren als auch mit theoretischen Vorhersagen überein. Comptonprofile von Graphit wurden in zwei Orientierungen aufgenommen: die c-Achse einerseits parallel zum einfallenden Strahl und andererseits unter 30 Grad gekippt. Die signifikante Anisotropie der ermittelten Impulsdichteverteilung stimmt recht gut mit früheren Messungen überein. Zusätzlich konnten die winkelabhängigen ELNES Spektren von Graphit in Übergänge in die π - und σ -Niveaus zerlegt werden; die Ergebnisse stimmen ebenfalls gut mit theoretischen Vorhersagen überein.

Abstract

Electron energy-loss spectroscopy in the near ionized edge region (electron energy-loss near-edge structure, ELNES) is a useful tool for the investigation of the electronic structure of the unoccupied state. Electron energy-loss spectroscopy in the high energy-loss region at large momentum transfer—electron Compton scattering from solids (ECOSS)—is a unique technique to determine the momentum distribution of the electronic ground state in a material. Therefore, the investigation of both the occupied and unoccupied states in a material can be done in one experiment. This thesis covers experimental and theoretical investigation of electron energy-loss spectroscopy, emphasizing the combination of those two aspects.

The use of electron Compton scattering instead of photon Compton scattering to determine electron momentum distributions in atoms and molecules can be traced back to 1938. At that time, electron Compton scattering experiments were carried out on gases. In 1981, B.G. Williams et al showed that electron Compton scattering from solids can be carried out in the transmission electron microscope by means of measuring electron energy-loss spectra at large scattering angle in the diffraction mode. The most severe problems of the technique were multiple scattering, strong contributions from Bragg scattering and the low signal in the Compton scattering region. The instrumental improvements in energy and spatial resolution, statistical accuracy, and reproducibility of recent years make it is possible to carry out experiments which could hardly work a decade ago. On modern electron microscopes, one can get an electron Compton profile in tens of seconds which is much shorter than several hundred seconds required 20 years ago. Also the methods of background subtraction have improved. These motivate a revival of the ECOSS technique.

The benefits of recording Compton profiles in a very short time are obvious. It opens up new possibilities: systematic studies of technological interesting materials become possible. The recording time is usually minutes, not hours or days, making a study of momentum transfer, orientation, composition and temperature dependence of Compton profiles feasible. The resolution and statistical accuracy have been improved simultaneously.

In this thesis, electron energy-loss near edge structures (ELNES) and electron Compton scattering from solids (ECOSS) of silicon (cubic crystal), natural graphite (hexagonal crystal) and amorphous carbon film (structureless) are systematically studied in the transmission electron microscope (TEM) by means of recording electron energy-loss spectra (EELS) at different scattering angles. The momentum transfer dependence of ECOSS for silicon and graphite was studied in the range from 6.0 to 9.0 a.u.. The valence Compton profile was obtained after a theoretical core profile subtraction was performed based on the Hartree-Slater model. The electron Compton profiles coincide well with other conventional Compton profile measurements, as well as with theory, thus establishing the validity of the technique. Electron Compton profiles of graphite have been recorded from the crystal with the c axis parallel and at 30° to the beam direction. A significant anisotropy has been found, which agrees fairly well with previous measurements on graphite. The angular and energy dependences of the π^* and σ^* structures of ELNES of graphite were completely separated, the results were also in fair agreement with theory.

Contents

Chapter 1 Introduction	3
1.1 The Compton effect.....	3
1.2 Photon Compton scattering	5
1.3 Electron Compton scattering.....	6
Chapter 2 Theory.....	8
2.1 The double differential scattering cross section (DDSCS).....	8
2.1.1 Electron inelastic scattering	8
2.1.2 Photon inelastic scattering.....	10
2.2 The Impulse Approximation.....	11
2.2.1 Kinematics of the scattering.....	11
2.2.2 Definition of an electron Compton profile	14
2.2.3 The validity of the impulse approximation.....	16
2.3 Hartree-Slater method	18
2.3.1 The dynamic form factor (DFF).....	18
2.3.2 Cowan code.....	19
2.3.3 $E \sim$ and $q \sim$ dependence of the GOS	22
2.3.4 The electron Compton profile	29
Chapter 3 Experiment.....	32
3.1 Transmission electron microscope (TEM)	32
3.1.1 Basics of the TEM.....	32
3.1.2 Electron-specimen interaction.....	34
3.2 EELS instrumentation	35
3.2.1 The magnetic-prism spectrometer	36
3.2.2 Operation modes	37
3.3 ECOSS in TEM.....	38
3.3.1 Momentum resolution	39
3.3.2 Background subtraction.....	40
Chapter 4 Application on Solids	50
4.1 Silicon.....	50
4.1.1 Experimental details.....	50

4.1.2 Results	53
4.2 Graphite	58
4.2.1 TEM sample preparation	59
4.2.2 Experimental details	63
4.2.3 Data analysis and results	66
4.2.4 Anisotropy of ECOSS in graphite	79
4.3 Amorphous carbon film	85
4.3.1 Experimental details	86
4.3.2 Results	88
4.4 Summary	89
Chapter 5 Conclusions and Outlook.....	90
Bibliography.....	92
Acknowledgements	98
Curriculum vitae	99

Chapter 1

Introduction

Much of our understanding about the structure of matter is extracted from scattering of photons, electrons, positrons, neutrons or other particles [1]. Had it not been for scattering experiments, the structure of the microphysical world would have remained inaccessible to us. It is convenient to divide the scattering of probes into elastic and inelastic components. Major forms of elastic scattering (involving negligible energy transfer) are Rayleigh scattering and Mie scattering. While, inelastic scattering includes Brillouin scattering, Raman scattering and Compton scattering [2]. Each scattering technique plays an important role in the investigation of the microphysical world. For example, Compton scattering is a unique and a highly useful tool for the electron momentum distribution investigations [3].

This thesis details how the Compton scattering experiments in the modern transmission electron microscope are performed, data are analyzed and results are discussed. The present section constitutes of a brief review on the history and literature of Compton scattering. In the Section 2, Fundamentals of electron inelastic scattering will be presented which relate the intensity for an scattering electron beam measured as function of scattering angle and energy loss to the electron energy loss spectroscopy (EELS). Section 3 briefly presents experimental instrument and the processing of experimental data. Experimental results and analysis are shown in the Section 4. In Section 5, a short summary and an outlook of future research are given.

1.1 The Compton effect

In the years 1922-1923, A.H. Compton allowed X-rays of monochromatic wavelength λ_0 to illuminate on a graphite block and measured the intensity of the scattered X-rays at different scattering angles [4, 5]. The scattered X-rays at any scattering angle show two wavelengths, the original wavelength λ_0 and a new larger wavelength λ' . This phenomenon of the increase in wavelength is known as Compton effect. In the early 20th century, the Compton effect served as an important evidence, in addition to photoelectric effect, of the particle nature of light, as it was successfully interpret by Compton as a collision between a photon and an electron at rest. In such a collision, the total energy and momentum remain conserved. In terms of the scattering angle θ , the wavelength increase, called the Compton shift, is given by

$$\Delta\lambda = \frac{h}{m_0c}(1 - \cos\theta), \quad (1.1)$$

where m_0 is the rest mass of the electron. The quantity h/m_0c is referred to as the Compton wavelength. The formula shows that the Compton shift is independent from the wavelength of incident radiation and the scatterer. The result was confirmed by experiment. Recasting formula (1.1) in terms of initial (E_0) and final (E') energies of photon yields the expression

$$\frac{E'}{E_0} = \frac{1}{1 + \alpha(1 - \cos \theta)}, \quad (1.2)$$

where

$$\alpha = \frac{E_0}{m_0c^2} = \frac{E_0}{511\text{keV}}.$$

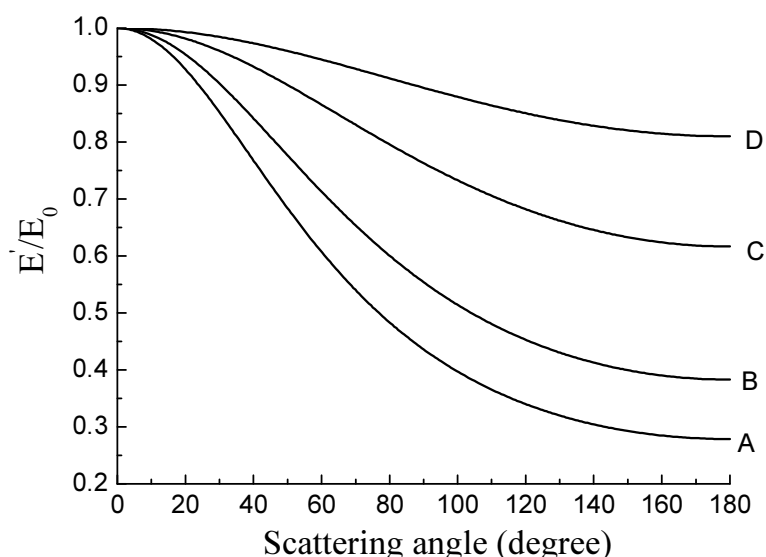


Figure 1.1 The degradation of photon energy for Compton scattering through the scattering angle 0-180° for a selection initial energies: A, 662 keV, ^{137}Cs ; B, 412 keV, ^{198}Au ; C, 159 keV, ^{123}Te ; D, 60keV, ^{241}Am [3].

The equation (1.2) is plotted in Fig. 1.1 for some selection initial energies. These curves emphasize the fact that Compton scattering is a major energy loss process for high-energy particles [3]. This effect is amplified at higher incident particle energies.

From equation (1.2), it can be seen that there is a one-to-one relationship (Compton line) between the scattering angle θ and the scattered final energy E' for a given incident energy E_0 . The experimental line was not sharp, i.e. there was not a complete one-to-one correspondence between the scattering angle and scattering final energy. This was interpreted as the electron momentum of scatterer prior to the scattering event should cause a Doppler broadening of the Compton line [6]. DuMond was the first who explained that the broadening of the Compton lineshape, usually

referred to as the Compton profile, results from the momentum distribution of the bound electrons [7-9]. In his model, now known as the impulse approximation (IA), the electrons involved in the scattering can be treated as free; their binding can be seen in the spread of their momenta. Apparently, the impulse approximation is valid only when the energy transfer in the scattering process greatly exceeds the binding energy [3]. As we shall discuss in Chapter 2 the motion of the bound electrons give rise to a second term in the Compton equation (1.1):

$$\Delta\lambda = (2h/m_0c)\sin^2(\theta/2) + 2(\lambda\lambda')^{1/2}(p_q/m_0c)\sin(\theta/2), \quad (1.3)$$

where p_q is the projection of the scattering electron's momentum along the direction of the scattering vector. This complete expression of Compton effect now shows that the process depends upon the physical nature of the target and opened the field of studying the electron momentum distributions by means of Compton scattering.

1.2 Photon Compton scattering

The term ‘‘Compton scattering’’ is traditionally associated with photon inelastic scattering at large momentum transfer. In its simplest way, a Compton scattering experiment involves a source of X-rays or γ -rays, a sample, an energy analyzer and a detector to record the scattered radiation [2]. Although the first observations of Compton effect were made using radioactive sources, early Compton scattering experiments were carried out with low-energy X-rays. There are several reasons for this. Firstly, at that time, X-ray generators typically produce photon fluxes four orders of magnitude larger than radioisotopes. Secondly, in any event there were no available detectors for performing a spectral analysis of high-energy radiation. On the other hand, X-rays tube, generators and crystal spectrometers had been extensively developed during the X-rays studies in the 1920s and 1930s [3]. Indeed, almost all photon Compton scattering experiments before 1970 were performed using X-rays [10, 11]. When an X-ray tube is used, the resolution is not a problem but the recorded count rates were so low that one experiment could take as long as 1 month [12]. DuMond and Kirkpatrick took 2000 hours to measure the Compton profile of helium [13]. The relatively low X-rays energy limits Compton experiments to materials with low atomic number elements.

In the late 1960s, the improvement of solid state detectors made it possible to use γ -rays sources in quantitative Compton scattering works [10, 14]. Although the resolution was lower than in X-rays measurements, the whole energy distribution could be measured simultaneously. Also the use of higher energies made it is possible to study heavier elements as well. Eisenberger et al took 3 days to obtain the Compton profile of krypton by γ -rays technique while to get the same resolution and signal to noise with X-rays source it would have taken more than one year [15]. The advantage of γ -rays technique was described briefly by M. Cooper et al in 1976 [16]. The Compton profiles of germanium have been measured with 412 keV γ -rays in 100 hours [16]. A number of γ -ray sources using radioactive isotopes offer a high, single

energy. Examples include ^{241}Am (60 keV) [10], $^{123}\text{Te}^m$ (159 keV) [10], ^{51}Cr (320 keV) [2], ^{198}Au (412 keV) [16] and ^{137}Cs (667 keV) [2]. The best momentum resolution in γ -ray measurements was limited to about 0.4 a.u., that is substantially worse than that of a high-resolution X-ray technique using an analyzing crystal [2].

The best source of X-rays is synchrotron radiation, which commonly offer a ten orders fold improvement in brilliance compared to X-ray tubes [12]. The advantages of synchrotron radiation source are obvious: a broad, continuous energy region extending up to hard X-rays can be obtained. The first operating Compton scattering experiment at a synchrotron radiation was introduced in 1980 at LURE [14]. The resolution was 0.15 a.u. but the energy range was limited to 5-15 keV. It was later followed by using new versions of high resolution Compton scattering spectrometers installed in synchrotron radiation source and almost all synchrotrons working at high X-ray energies. The spectrometers at synchrotron radiation apparatus acquire better than 0.1 a.u. momentum resolution, and several statistically precise Compton profiles can be obtained in one day [17]. Most Compton scattering experiment based on synchrotron radiation are currently performed at the European Synchrotron Radiation Facility (ESRF, located in Grenoble, France) or at Spring-8 (Japan) [18-20].

1.3 Electron Compton scattering

The use of electron instead of photon to study electron momentum distributions in atoms and molecules can be traced back to 1938 [21]. Between 1938 and 1941, Hughes and coworkers reported a series of publications on Compton profiles using electrons [22-24]. In 1938, Hughes and Mann obtained the energy loss spectrum of helium using high energy incident electrons showed the same characteristic Compton profile [22]. The electron Compton scattering technique is more sensitive to the local electronic structure than photon Compton scattering. The cross-section of electron scattering is roughly 10^4 times greater than it is for photons [11]. Subsequently, Hughes and Enns measured a series of Compton profiles using electron scattering [24]. However, the experimental electron Compton profiles are significantly broader than the calculation by using variation functions [25]. This discrepancy was ascribed to multiple scattering [26]. Along with multiple scattering problem there were difficulties in measuring the accurate scattering angle. Furthermore, the electron scattering technique requires high vacuum conditions, so it is not as easy to employ as the photon Compton scattering technique. Consequently, because of experimental difficulties and lack of agreement with theory, electron Compton scattering technique stopped and was not revived for 30 years.

A major improvement in the electron Compton scattering experiment was made by Wellenstein and Bonham in 1973, they obtain an energy resolution 20 times better than that feasible by photon Compton scattering [27]. The problem of multiple scattering can be controlled and high energy electron scattering can be carried out for Compton profile measurements for targets in gas phase. Since then electron Compton profiles of H_2 , D_2 , He, N₂, Ne, Ar, CH₄ and C₂H₄ reported in the literature [28-30].

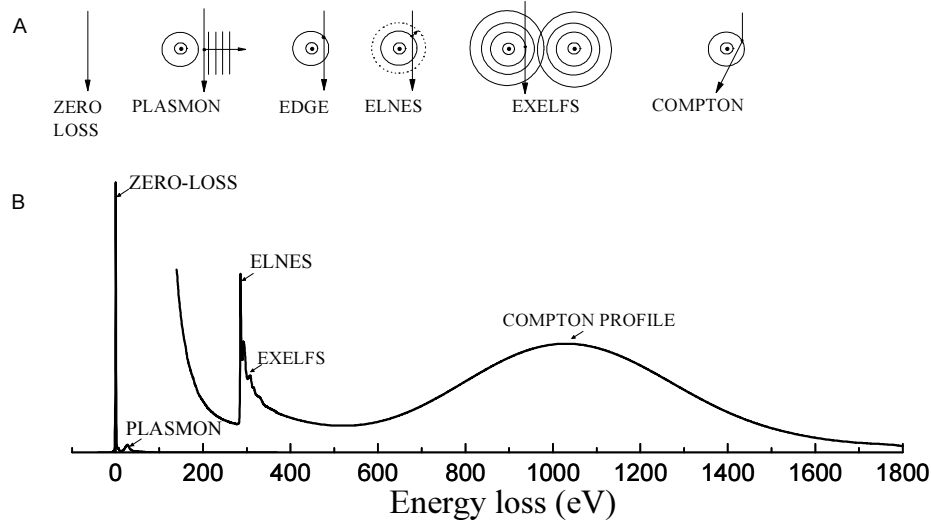


Figure 1.2 Schematic diagram of (A) the process of electron scattering in target and (B) the corresponding electron energy-loss spectrum (EELS). ELNES is electron energy-loss near edge structure and EXELFS is extended energy-loss fine structure. Figure adapted from Thomas [31].

Electron Compton scattering from solid (ECOSS) was recorded in transmission electron microscope equipped with an electron energy-loss spectrometer by Williams et al in 1981 [32]. The electron Compton profile of amorphous carbon was obtained in 1 hour compared with several days using photons. The advantages of this technique are obvious. In addition to all other informations from electron energy-loss spectroscopy are available (Fig. 1.2), it also made possible to combine the momentum distribution with image, diffraction pattern and energy-dispersive spectrometer experiments [31]. The major drawback of ECOSS relates to the background subtraction and the strong Bragg scattering. These may be the reasons that no real progress has been reported on ECOSS in the following decade.

In the last 20 years, the improvements in instrumentation have been dramatic. Field emission sources and monochromators are commonly used in TEMs. The energy-loss spectrometer has been improved with a fast electrostatic shutter [33]. On modern transmission electron microscopes, one can get an electron energy-loss spectrum in the Compton scattering region in 1 min which is much shorter than the thousand seconds required 20 years ago [34]. Also the method of background subtraction has been improved [35, 36]. These motivate a revival of the ECOSS technique.

Chapter 2

Theory

Fundamentals of electron inelastic scattering will be presented in this chapter. Compton scattering will occur when the energy loss is much larger relative to the binding energy of an electron at large momentum transfer. The Compton profile is interpreted as the momentum distribution of the electronic ground state by the impulse approximation. The cross section for each orbit of an atom can be calculated by the Hartree-Slater method in the Compton regime.

2.1 The double differential scattering cross section (DDSCS)

The quantity measured in a typical inelastic scattering experiment is the double differential scattering cross section (DDSCS) $d^2\sigma/dEd\Omega$, which is defined as the number of particles scattered into the energy-loss interval dE , respective the solid angle $d\Omega$ (at a fixed momentum transfer \mathbf{q}). In other words, the DDSCS is a function of momentum transfer \mathbf{q} and energy loss E .

2.1.1 Electron inelastic scattering

In order to calculate DDSCS in theory, we may start with Fermi's golden rule. It is assumed that the interaction is weak between the probing electron and the target in the limit of high incident energies, so that the first order perturbation theory is valid. The probability for transitions from an initial state $|a\rangle$ into a final state $|b\rangle$ is proportional to the square of the transition matrix element. The transition rate dW_{ab} (probability of transition per unit time) can be defined as [37]

$$dW_{ab} = \frac{2\pi}{\hbar} |\langle b|V|a\rangle|^2 d\rho_b \delta(E_a - E_b), \quad (2.1)$$

here, V is the interaction potential, i.e. V is small for fast collisions. $d\rho_b$ is the differential phase space element around the final state $|b\rangle$, and the delta term guarantees the conservation of energy. If assuming the potential V is weak enough, we may approximate the scattered electron as a free plane wave with an energy $E = \hbar^2 k_b^2 / 2m$, k_b is the wave vector of the final state; the differential phase space element for this plane wave is

$$d\rho_b = k_b^2 dk_b d\Omega = k_b \frac{m}{\hbar^2} dE d\Omega. \quad (2.2)$$

Now, the differential electron current of free electrons scattered into $(d\Omega, dE)$ is gained, using Eq. (2.1) and (2.2), summing over all final states $|b\rangle$

$$dj = \frac{\partial W}{\partial E \partial \Omega} dE d\Omega = dj(dE, d\Omega) = \sum_b \frac{2\pi}{\hbar} |\langle b|V|a\rangle|^2 \frac{k_b m}{\hbar^2} dE d\Omega \delta(E_a - E_b). \quad (2.3)$$

On the other hand,

$$dj = d\sigma(E, \Omega) \cdot j_i, \quad (2.4)$$

where $d\sigma(E, \Omega)$ is the scattering cross section and j_i is the incident current density of the plane wave $\varphi_{k_a}(\vec{r}) = (2\pi)^{-3/2} e^{i\vec{k}_a \cdot \vec{r}}$, \vec{k}_a is the wave vector of the incident electrons. From Eqs. (2.3) and (2.4), one obtains:

$$\frac{\partial^2 \sigma}{\partial E \partial \Omega} = \sum_b \frac{2\pi k_b m}{\hbar^3 j_i} |\langle b | V | a \rangle|^2 \delta(E_a - E_b), \quad (2.5)$$

using the relation

$$j_i = \frac{i\hbar}{2m} (\varphi \vec{\nabla} \varphi^* - \varphi^* \vec{\nabla} \varphi). \quad (2.6)$$

We obtains the incident current density

$$j_i = \frac{\hbar k_a}{m} (2\pi)^{-3} \quad (2.7)$$

and the double differential scattering cross section

$$\frac{\partial^2 \sigma}{\partial E \partial \Omega} = \left(\frac{2\pi}{\hbar} \right)^4 m^2 \sum_b \frac{k_b}{k_a} |\langle b | V | a \rangle|^2 \delta(E_a - E_b). \quad (2.8)$$

As already mentioned, the validity of Eq. (2.8) requires a weak interaction potential, i.e. the potential V must be sufficiently small compared with the energy of the scattered electrons. In the absence of the perturbation or interaction, the system “probe+target” can be factorized a product state contracted from eigenstate of “probe alone” and “target alone”, respectively, where the exchange effects are negligible.

$$|a\rangle = |k_a\rangle \otimes |i\rangle \quad |b\rangle = |k_b\rangle \otimes |f\rangle, \quad (2.9)$$

$|k_a\rangle, |k_b\rangle$ are free states for probe and $|i\rangle, |f\rangle$ are the eigenstates of electrons before and after scattering for the target, the corresponding eigenfunctions are $\varphi_i(\vec{r}_1, \dots, \vec{r}_n)$ and $\varphi_f(\vec{r}_1, \dots, \vec{r}_N)$ for the N-electron target system. The matrix element $\langle b | V | a \rangle$ is obtained in \vec{r} -space by inserting the unity operator

$$\int d^3 r_1 \dots d^3 r_N |r\rangle \otimes |r_1 \dots r_N\rangle \langle r_1 \dots r_N| \otimes \langle r| d^3 r = 1. \quad (2.10)$$

Hence

$$\langle b | V | a \rangle = \frac{1}{(2\pi)^3} \int d^3 r_1 \dots d^3 r_N \varphi_f^*(\vec{r}_1 \dots \vec{r}_N) \varphi_i(\vec{r}_1 \dots \vec{r}_N) V(\vec{r}, \vec{r}_1 \dots \vec{r}_N) e^{i(\vec{k}_a - \vec{k}_b) \cdot \vec{r}} d^3 r. \quad (2.11)$$

To the system of our interest, a fast probe electron and its atomic target, the interaction is Coulombic. Below an incident energy of about 300 keV, the interaction potential can be written as [33]

$$V = -\frac{Ne^2}{4\pi\epsilon_0 r} + \frac{1}{4\pi\epsilon_0} \sum_{i=1}^N \frac{e^2}{|\vec{r} - \vec{r}_i|} \quad (2.12)$$

and by virtue of

$$\int d^3r e^{i\vec{q}\cdot\vec{r}} \frac{1}{|\vec{r}-\vec{r}_i|} = \frac{4\pi}{q^2} e^{i\vec{q}\cdot\vec{r}_i}, \quad (2.13)$$

where $\hbar\vec{q} = \hbar(\vec{k}_a - \vec{k}_b)$ is the momentum transfer during interaction, The transition matrix element becomes

$$\begin{aligned} \langle b|V|a\rangle &= \frac{1}{(2\pi)^3} \frac{e^2}{4\pi\epsilon_0} \int d^3r_1 \dots d^3r_N \varphi_f^*(\vec{r}_1 \dots \vec{r}_N) \varphi_i(\vec{r}_1 \dots \vec{r}_N) \left(-\frac{N}{r} + \sum_{i=1}^N \frac{1}{|\vec{r}-\vec{r}_i|} \right) e^{i(\vec{k}_a - \vec{k}_b)\cdot\vec{r}} d^3r \\ &= \frac{1}{(2\pi)^3} \frac{e^2}{4\pi\epsilon_0} \int d^3r_1 \dots d^3r_N \varphi_f^*(\vec{r}_1 \dots \vec{r}_N) \varphi_i(\vec{r}_1 \dots \vec{r}_N) \sum_{i=1}^N \frac{1}{|\vec{r}-\vec{r}_i|} e^{i(\vec{k}_a - \vec{k}_b)\cdot\vec{r}} d^3r \\ &= \frac{1}{(2\pi)^3} \frac{e^2}{4\pi\epsilon_0} \frac{4\pi}{q^2} \int d^3r_1 \dots d^3r_N \varphi_f^*(\vec{r}_1 \dots \vec{r}_N) \varphi_i(\vec{r}_1 \dots \vec{r}_N) \sum_{i=1}^N e^{i\vec{q}\cdot\vec{r}_i} d^3r. \end{aligned} \quad (2.14)$$

Considering electronic excitations of the target in Born-Oppenheimer approximation, i.e. the eigenfunctions are independent of the nuclei, the first part of the interaction potential vanishes since $|\varphi_f\rangle$ and $|\varphi_i\rangle$ are orthogonal.

We may define a well known quantity in nuclear physics and solid state physics

$$\begin{aligned} S(\vec{q}, E) &:= \sum_f \left[\int d^3r_1 \dots d^3r_N \varphi_f^*(r_1 \dots r_N) \sum e^{i\vec{q}\cdot\vec{r}} \varphi_i(r_1 \dots r_N) \right]^2 \delta(E_i - E_f + E) \\ &= \sum_f \left| \langle f | \sum_i e^{i\vec{q}\cdot\vec{r}_i} | i \rangle \right|^2 \delta(E_i - E_f + E). \end{aligned} \quad (2.15)$$

$S(\vec{q}, E)$ is known as dynamic form factor (DFF). The δ -function selects transitions with the energy-loss $E = E_f - E_i$. Finally, considering relativistic corrections by $m = \gamma m_e$ and recurring to the Bohr radius $a_0 = 4\pi\epsilon_0 \hbar^2 / m_e e^2 = 0.529 \times 10^{-10} m$, from Eqs. (2.8), (2.14) and (2.15) one obtains:

$$\frac{\partial^2 \sigma}{\partial E \partial \Omega} = \left(\frac{4\gamma^2}{a_0^2 q^4} \right) \frac{k_b}{k_a} S(\vec{q}, E) = \left(\frac{d\sigma}{d\Omega} \right)_R \frac{k_b}{k_a} S(\vec{q}, E), \quad (2.16)$$

where the first term is the Rutherford scattering cross section.

2.1.2 Photon inelastic scattering

For photon scattering, the Hamiltonian of an electron in an electromagnetic field can be described by $\vec{p} \cdot \vec{A}$ and A^2 terms (\vec{A} = the vector potential). If the incident photon energy is much larger than the binding energy of the electron, then the $\vec{p} \cdot \vec{A}$ term is negligible. In this limit, the DDSCS mainly comes from A^2 . Under these assumptions, the DDSCS for the photon inelastic scattering can be written as [38]

$$\frac{\partial^2 \sigma_p}{\partial E \partial \Omega} = \left(\frac{d\sigma}{d\Omega} \right)_{Th} \frac{\omega_2}{\omega_1} S(\vec{q}, E), \quad (2.17)$$

here, ω_1 and ω_2 are energies of the photon before and after scattering, the Thomson cross section

$$\left(\frac{d\sigma}{d\Omega} \right)_{Th} = \left(\frac{e^2}{mc^2} \right)^2 |\vec{\epsilon}_1 \cdot \vec{\epsilon}_2|^2, \quad (2.18)$$

where c is the velocity of light in vacuum, $\vec{\epsilon}_1$ and $\vec{\epsilon}_2$ are the incident and scattered photon polarization vectors.

From Eqs. (2.16) and (2.18), the ratio of electron to photon scattering cross section in atomic units ($c = 137$) is

$$R = \frac{d^2 \sigma_e}{dE d\Omega} \bigg/ \frac{d^2 \sigma_p}{dE d\Omega} = \frac{k_b}{k_a} \frac{\omega_2}{\omega_1} \left(\frac{4c^4}{q^4} \right), \quad (2.19)$$

which is typically greater than 10^4 as long as the momentum transfer for electron scattering doesn't exceed 14 a.u. [21].

The physical and chemical information of the DFF (or the DDSCS) depends on the region of \vec{q} and E . For example, by expanding the exponential transition operator $\exp(i\vec{q} \cdot \vec{r}) = 1 + i\vec{q} \cdot \vec{r} + (i\vec{q} \cdot \vec{r})^2 / 2 + \dots$. One sees that at low q , this reduces to a dipole operator. In this limit, electron energy-loss spectrum contains information about the unoccupied density of states of the material. When the momentum transfer increases, other terms in the expansion become more important, giving the opportunity to investigate dipole-forbidden transitions. In this work, we will focus on the Compton scattering region, in which the momentum transfer is larger compared to the inverse electronic orbital size of the scattered electron and the energy loss is much larger relative to the binding energy. The Compton profile provides information about the ground-state electron momentum density distribution. These will be discussed in the following sections.

2.2 The Impulse Approximation

In order to understand the Compton lineshape, some approximations are made [39]. These approximations have come to be known as the impulse approximation for the photon Compton scattering and the binary encounter theory for electron Compton scattering [28]. The impulse approximation gives a simple connection between the DDSCS (observable) and the Compton profile.

2.2.1 Kinematics of the scattering

Consider an experiment in which an electron is scattered from one electron in the sample as shown schematically in Fig. 2.1. The equations for energy and momentum conservation are

$$\vec{p}_1 + \vec{p}_i = \vec{p}_2 + \vec{p}_f, \quad (2.20)$$

$$E_1 + E_i = E_2 + E_f, \quad (2.21)$$

where the subscripts 1 and 2 denote the incident and scattered probe electron and i and f refer to the initial and final states of the sample electron. The electron Compton scattering experiments in the TEM only the scattered electron not the ejected electron is detected, so one must solve Eqs (2.20) and (2.21) simultaneously

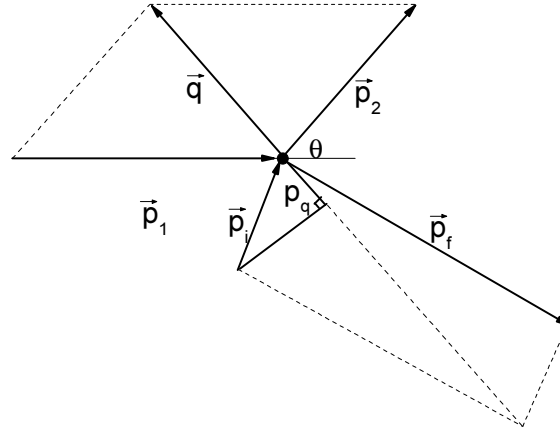


Figure 2.1 Momentum conservation diagram for electron Compton scattering. \vec{p}_1 and \vec{p}_2 are the momentum of the incident and scattered electrons; \vec{p}_i and \vec{p}_f are the momentum of the initial and final state of the sample electron, respectively.

to eliminate the momentum \vec{p}_f and energy E_f of final states. Assuming E_i and E_f are the kinetic energies of the initial and final states for the sample electron, these equations lead directly to an expression for energy loss E , the energy transferred from the incident electron to the electron in the sample is:

$$\begin{aligned} E = E_f - E_i &= p_f^2/2m - p_i^2/2m \\ &= q^2/2m + \vec{p}_i \cdot \vec{q}/m, \end{aligned} \quad (2.22)$$

where q is the momentum transferred in the scattering interaction. The first term on the right side of Eq. (2.22) gives the energy loss of Compton peak or line for scattering from stationary—free electron. The second term is proportional to the component in the direction of the momentum transfer of the ground state momentum of the sample electron and gives the Doppler broadening of the Compton line. Schematically, the Compton profile is plotted in Fig. 2.2. Since, to observe the Compton profile, the energy transfer must be greater than the binding energy E_B of the electrons in the sample.

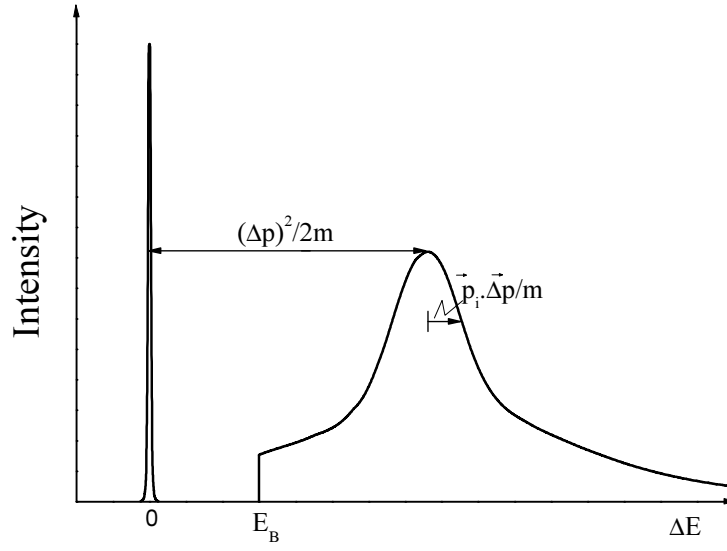


Figure 2.2. Schematic diagram of an experimental Compton profile plotted with respect to the energy loss. The peak shift and the broadening are given by Eq. (2.22). The cutoff occurs at the binding energy E_B .

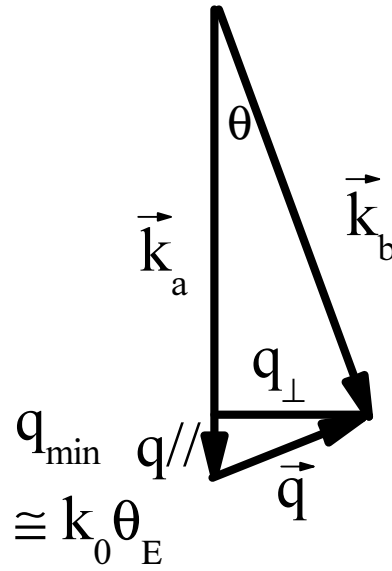


Figure 2.3. Momentum transfer components for a fast electron showing the incident and scattered electron with wave vectors \vec{k}_a and \vec{k}_b , and the momentum transfer \vec{q} for scattering angle θ . The minimum (parallel) momentum transfer is also indicated.

The incident electron beam with primary energy 200 keV, one has to include relativistic terms in the expressions of energy and momentum respectively. Equation (2.19) is the exact nonrelativistic expression as long as $E \ll mc^2$. The relativistic relation between kinetic energy and momentum for the incident electron is

$$p_a^2 = E_a (E_a + 2). \quad (2.23)$$

Further simplification can be made by neglecting the momentum transfer variation, $|\vec{p}_a| \simeq |\vec{p}_b|$, thus the modulus of the momentum transfer q is related scattering angle θ as (see Fig. 2.3):

$$q = 2|\vec{p}_a| \sin \frac{\theta}{2}. \quad (2.24)$$

Finally, we get an expression for the energy-loss spectrum as a function of scattering angle θ and the momentum component p_q from Eq. (2.22)

$$\begin{aligned} E &= E_{\max} + p_q (2E_{\max}/m)^{1/2}, \\ E_{\max} &= E_a \left(1 + \frac{E_a}{2mc^2} \right) \cdot \sin^2 \theta, \end{aligned} \quad (2.25)$$

where E_{\max} is the energy loss of Compton peak at a fixed scattering angle, and p_q is the projection of the ground-state momentum of the sample electron in the direction of the momentum transfer. Eq. (2.25) is used as starting point for electron Compton profile analysis within the binary encounter impulse approximation since they serve to convert the energy scale of a measured energy loss spectrum to a momentum scale.

2.2.2 Definition of an electron Compton profile

In this section, we will derive an approximate expression of DDSCS for collisions upon which the incident electron has a sufficiently large energy to one of the atomic electrons and the binding energy of the atomic electron plays a secondary role, so that the energy and momentum transfer are correlated nearly as if the scattering electron was free. We shall call this treatment of DDSCS as the binary encounter impulse approximation.

In order to derive the impulse result, let us assume in the δ function of DFF (Eq. (2.15)) that the scattered electron can be treated as free (but moving) during the entire collision. Before the collision set the electron has the momentum \vec{p}_i and after the collision momentum \vec{p}_f . Then

$$E_i = \frac{p_i^2}{2m}, \quad E_f = \frac{p_f^2}{2m}. \quad (2.26)$$

Momentum conservation for this free electron collision gives

$$\vec{p}_f = \vec{p}_i + \hbar \vec{q}; \quad p_f^2 = p_i^2 + 2\hbar \vec{p}_i \cdot \vec{q} + \hbar^2 q^2 \quad (2.27)$$

and δ function in Eq. (2.15) can be written as

$$\delta\left[-(2\hbar\vec{p}_i \cdot \vec{q} + \hbar^2 q^2)/2m + E\right] = \delta\left\{\frac{\hbar q}{m}\left[\frac{\vec{p}_i \cdot \vec{q}}{q} - \left(\frac{mE}{\hbar q} - \frac{\hbar q}{2}\right)\right]\right\}. \quad (2.28)$$

Within the impulse approximation the final state $|f\rangle$ is taken to be a plane wave

$$\varphi_f(\vec{r}) = e^{i\vec{p}_f \cdot \vec{r}/\hbar}. \quad (2.29)$$

In the momentum space, the ground state wave function $\chi_i(\vec{p}_i)$ is the Fourier transform of the corresponding wave function in real space, so that

$$\chi_i(\vec{p}_i) = (2\pi\hbar)^{-3/2} \int \varphi_i(\vec{r}) e^{-i\vec{p}_i \cdot \vec{r}/\hbar} d^3r \quad (2.30)$$

and the sum over final states is

$$\sum_f \rightarrow \int (2\pi\hbar)^{-3} d^3p_f. \quad (2.31)$$

Choosing the momentum transfer \vec{q} to lie in the z direction and using momentum conservation, we obtain the following expression for DFF

$$\begin{aligned} & \sum_f |\langle f | e^{i\vec{q} \cdot \vec{r}} | i \rangle|^2 \delta(E_i - E_f + E) \\ &= \int d^3p_f \left| (2\pi\hbar)^{-3/2} \int d^3r e^{i\vec{p}_i \cdot \vec{r}/\hbar} \varphi_i(\vec{r}) \right|^2 \delta\left\{\frac{\hbar q}{m}\left[p_{iz} - \left(\frac{mE}{\hbar q} - \frac{\hbar q}{2}\right)\right]\right\}. \end{aligned} \quad (2.32)$$

Defining

$$p_q = \frac{mE}{\hbar q} - \frac{\hbar q}{2}, \quad (2.33)$$

Eq. (2.32) reduces to

$$\int d^3p_f |\chi_i(\vec{p}_i)|^2 \delta\left[\frac{\hbar q}{m}(p_{iz} - p_q)\right]. \quad (2.34)$$

Noting that for the incident energy E_a , scattering angle θ and energy loss E , momentum transfer q is also fixed, it follows from Eq. (2.27) that the integral over d^3p_f is equivalent to an integration over $d^3p_i = dp_{ix} dp_{iy} dp_{iz}$. Utilizing the properties of the delta function, Eq. (2.34) becomes

$$\frac{m}{\hbar q} \iint |\chi_i(p_{ix}, p_{iy}, p_q)|^2 dp_{ix} dp_{iy}, \quad (2.35)$$

which is an integration over the plane in the momentum space $p_{iz} = p_q$. Consider a spherically symmetric momentum density distribution; it is convenient to rewrite Eq. (2.35) in cylindrical coordinates

$$S(\vec{q}, E) = \frac{m}{\hbar q} J(p_q), \quad (2.36)$$

where $J(p_q)$ is taken as the definition of Compton profile

$$J(p_q) = 2\pi \int_{p_q}^{\infty} |\chi_i(p_i)|^2 p_i dp_i, \quad (2.37)$$

where the momentum wave function $\chi(\vec{p})$ can be obtained either from a Fourier transformation of the wave function $\varphi(\vec{r})$ in real space or directly by solution of the Schrödinger equation in the momentum representation. In the last step of the derivation we use the relationship Eq.(2.16) between the DDSCS and the dynamic form factor to obtain

$$\frac{\partial^2 \sigma}{\partial E \partial \Omega} = \frac{4\gamma^2 k_b}{\hbar a_0^2 k_a} \frac{J(p_q)}{q^5}. \quad (2.38)$$

A closely related quantity is the generalized oscillator strength (GOS), defined as

$$\frac{df(\vec{q}, E)}{dE} = \frac{E S(\vec{q}, E)}{R (qa_0)^2}, \quad (2.39)$$

where E has the units eV and R is the Rydberg energy. If we take Rydberg atomic units ($\hbar = 2m_e = e^2/2 = 1$, and energy : $1 a.u. = 13.6 eV$), we obtain

$$J(p_q) = \frac{2q^3}{E} \frac{df(\vec{q}, E)}{dE}, \quad (2.40)$$

$$p_q = \frac{E - q^2}{2q}. \quad (2.41)$$

Equations (2.16) and (2.39) can be used to convert relative measured intensities to relative measurement of GOS which can be placed on an absolute scale by use of the Bethe sum rule. The absolute GOS is then converted to Compton profile by Eq. (2.40) within the binary theory.

2.2.3 The validity of the impulse approximation

From the forgoing analysis it appears quite clear that if the impulse approximation holds, the energy transfer must greatly exceed the binding energy of an electron, and the momentum transfer must be large relative to the inverse electronic orbital size. In the other words, in electron Compton scattering experiments the energy loss E_{\max} of Compton peak should be located far away from the ionized edge of the electron shell of interest. The energy loss of Compton peak depends on the scattering angle through the electron Compton equation (2.22). These equations indicate that the electron Compton profile should be recorded at scattering angle as large as possible. On the other hand, the DDSCS for electron scattering decreases as the fourth power of the scattering angle [40], so it is important to keep the scattering angle as small as possible for inelastic electrons to obtain maximize the recorded intensity. Therefore it is necessary to check the validity of the impulse approximation to the ratio of (the energy transfer E_{\max})/(the binding energy E_B).

Wong et al [41] have shown that if one uses a frozen-core approximation and an

accurate wavefunction for the final state electron (rather than a free electron plane wave as in the impulse approximation), the Compton defect and asymmetry can be accurately calculated. An examination of the validity of impulse approximation to the ratio of the energy loss (E_{\max}) at the Compton peak to binding energy (E_B) of the sample electrons particular for electron Compton scattering on solid has been reported by Williams et al [40]. Analytic results based on the hydrogenic expression, we shall refer to the correct results as the “exact hydrogenic (EH)” results, $J_{EH}(p_q)$ and the impulse approximation results as the “impulse hydrogenic (IH)”, $J_{IH}(p_q)$. A comparison of the impulse hydrogenic and exact hydrogenic for K-shell is written as

$$J_{EH}(p_q) = C J_{IH}(p_q), \quad (2.42)$$

where

$$C = 2\pi \left(1 + \frac{1}{4} p'_q \right) r^{-1/2} \frac{e^{-2\beta(r-1)^{-1/2}}}{1 - e^{-2\pi/s}},$$

with

$$p'_q = p_q \left(\frac{2}{E_{\max}} \right)^{1/2}, \quad E = E_{\max} (1 + p'_q), \quad r = \frac{E_{\max}}{E_B},$$

$$s^2 = r + r p'_q - 1, \quad \tan \beta = \frac{2s}{r p'_q + 2}.$$

The result is parameterized in terms of the ratio r of the energy loss of Compton peak to the binding energy of the electron. By writing the equation in this form, it is obvious that for $r \rightarrow \infty$, $C \rightarrow 1$, thus the IH Compton profile is equivalent to the EH Compton profile for large energy loss. To confirm the validity of these expressions, the EH calculation for helium is compared in Fig. 2.4 (a) with electron scattering measurements and with the more accurate calculations from Wong et al [41]. ΔJ

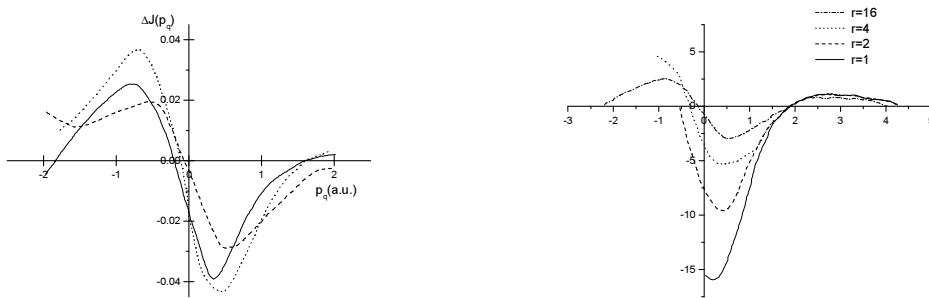


Figure 2.4 (a) The difference between the exact and impulse approximation Compton profile of Helium. The solid line is obtained from the experimental data and the dashed line gives the calculation from Wong et al. The dotted line is obtained from Eq (2.40). (b) Corrections to the impulse approximation calculation of carbon as a percentage of the peak height of the profile. Solid line $E_{\max} = E_B$, dashed line $E_{\max} = 2E_B$, dotted line $E_{\max} = 4E_B$ and dash dotted line $E_{\max} = 16E_B$. The data comes from Williams et al [40].

denotes the difference between the exact and impulse approximation Compton profile. The agreement is quite good across the whole momentum range. In Fig. 2.4 (b), the results of $\Delta J/J(0)$ for carbon have been plotted for several values of r , respectively [40]. It showed that when $r=4$, the maximum error in the estimation of the contribution from the K-shell will be 6% which corresponds to 1% of the total Compton peak height. This indicates that the impulse approximation is generally valid if the energy transfer (energy-loss) at the Compton peak is more than about four times the binding energy of the scattered electron. Since valence electrons have binding energy in the order of 10 eV, this condition is not difficult to attain in electron Compton scattering experiment.

2.3 Hartree-Slater method

In a typical Compton scattering experiment, the valence Compton profile is obtained only after the core Compton profile subtraction is performed by theoretical calculations. A Hartree-Slater central field model is used in this work. In solids where valence electrons undergo pronounced changes in their momentum distributions from free atoms while the core electrons differ very little between free-atom and solid, so that a Hartree-Slater free atom calculation for the core electrons should suffice to determine their contribution to the total Compton spectra.

2.3.1 The dynamic form factor (DFF)

We replace states $|i\rangle$ and $|f\rangle$ in Eq. (2.15) by wave functions $|nl\rangle$ and $|\epsilon l'\rangle$, the DFF becomes

$$S(\vec{q}, E) = \sum_{l'} \left| \langle \epsilon l' | \exp(i\vec{q} \cdot \vec{r}) | nl \rangle \right|^2 \delta(E_{nl} - \epsilon + E). \quad (2.43)$$

Here, n and l refer to the initial-state principal and angular momentum quantum numbers, respectively. The final state is described by the continuum energy ϵ and the angular momentum number l' . In the following, we shall neglect the delta function, implicitly including the energy conservation by setting $E = \epsilon - E_{nl}$, where E_{nl} (negative) is the binding energy of the initial state. In order to calculate the transition matrix element of the DFF, following Manson [42], we use the well-known expansion

$$e^{i\vec{q} \cdot \vec{r}} = \sum_{\lambda} i^{\lambda} (2\lambda + 1) j_{\lambda}(qr) P_{\lambda}(\cos \theta), \quad (2.44)$$

where $j_{\lambda}(qr)$ is the λ -th order spherical Bessel function, $P_{\lambda}(\cos \theta)$ is the Legendre polynomials and θ is the angle between \vec{q} and \vec{r} . Then the expression for the transition matrix element (for transition $|nlm\rangle \rightarrow |\epsilon l' m'\rangle$) after integrating out the wave functions of the nonparticipating electrons and using the Wigner-Eckart theorem becomes

$$\langle \epsilon l' m' | \exp(i\vec{q} \cdot \vec{r}) | nlm \rangle = \sum_{\lambda} i^{\lambda} (2\lambda + 1) [(2l + 1)(2l' + 1)]^{1/2} (-1)^{m'} \begin{pmatrix} l' & \lambda & l \\ 0 & 0 & 0 \end{pmatrix} \begin{pmatrix} l' & \lambda & l \\ -m' & 0 & m \end{pmatrix}$$

$$\times \int_0^\infty \phi_{nl}(r) j_\lambda(qr) \phi_{\epsilon l'} dr, \quad (2.45)$$

where $\begin{pmatrix} l' & \lambda & l \\ 0 & 0 & 0 \end{pmatrix}$ and $\begin{pmatrix} l' & \lambda & l \\ -m' & 0 & m \end{pmatrix}$ are Wigner $3-j$ symbols and the sum over λ goes from $|l'-l|$ to $l'+l$ in steps of twos, due to the $3-j$ symbol $\begin{pmatrix} l' & \lambda & l \\ 0 & 0 & 0 \end{pmatrix}$ equals zero for other values of λ . ϕ_{nl} and $\phi_{\epsilon l'}$ are the radial component of initial ground state and unbound continuum final state of the atom in scattering procedure. The absolute square of the DFF for an $|nlm\rangle \rightarrow |\epsilon l' m'\rangle$ transition from a closed subshell, summed over all final degenerate magnetic substrates m' and average over initial substates m , can be written

$$\begin{aligned} \left| \langle \epsilon l' m' | \exp(i\vec{q} \cdot \vec{r}) | nlm \rangle \right|^2 &= \sum_{\lambda, \lambda'} i^{\lambda-\lambda'} (2\lambda+1)(2\lambda'+1)(2l'+1) \begin{pmatrix} l' & \lambda & l \\ 0 & 0 & 0 \end{pmatrix} \begin{pmatrix} l' & \lambda & l \\ 0 & 0 & 0 \end{pmatrix} \\ &\times \int_0^\infty \phi_{nl}(r) j_\lambda(qr) \phi_{\epsilon l'} dr \times \int_0^\infty \phi_{nl}(r) j_{\lambda'}(qr) \phi_{\epsilon l'} dr \\ &\times \sum_{m, m'} \begin{pmatrix} l' & \lambda & l \\ -m' & 0 & m \end{pmatrix} \begin{pmatrix} l' & \lambda' & l \\ -m' & 0 & m \end{pmatrix}. \end{aligned} \quad (2.46)$$

The sum over $\sum_{m, m'}$ is, considering the properties of Wigner $3-j$ symbols,

$\delta_{\lambda\lambda'}/(2\lambda+1)$, so that the DFF becomes

$$S(\vec{q}, E) = \sum_{l'} \sum_{\lambda} (2l'+1)(2\lambda+1) \left| \begin{pmatrix} l' & \lambda & l \\ 0 & 0 & 0 \end{pmatrix} \right|^2 \left[\int_0^\infty \phi_{nl}(r) j_\lambda(qr) \phi_{\epsilon l'}(r) dr \right]^2. \quad (2.47)$$

In writing this equation, we have assumed the initial and final states in the transition can be expressed as products of one-electron wave functions for the same central potential. Thus, wave functions of the electrons not directly involved in the transition remain unchanged. This means that many-body effects such as electron-electron correlation or core relaxation are not taken into account [43, 44]. In our works, the wave functions are obtained by Cowan code (<http://www.tcd.ie/Physics/people/Cormac.McGuinness/Cowan/>). The integrations were carried out using Mathematica 8.

2.3.2 Cowan code

Cowan's code was used to calculate atomic structures and spectra via the superposition-of-configuration method. This code is a set of FORTRAN 77 programs for the calculation of atomic radial wave function (bound or free) and of various radial integrals involved in the calculation of atomic energy levels and spectra. A full description of the programs is given by R.D. Cowan [45]. The Cowan code includes

the following programs:

1. RCN Mod 36 – calculates one-electron radial wave functions (bound or free) for each of any number of specified electron configurations.
2. RCN2 – accepts radial wave functions from RCN and calculates multiple-configuration radial integrals. Prepares the input files for RCG.
3. RCG – calculates angular matrix elements, energy levels, and atomic spectra.
4. RCE – can be used to make a least-squares fitting of experimental energy levels by an iterative procedure.

Program RCN Mod 36 can be run singly, but RCN2 requires the output wave functions from RCN Mod 36, and the two are commonly run in succession to provide input for the third program RCG to calculate atomic energy levels and spectra. In program RCN Mod 36, there is a choice of four approximations to the Hartree-Fock method, namely, (1) Hartree, (2) Hartree-Fock-Slater, (3) Hartree-plus-statistical-exchange and (4) Hartree-Slater. In our works, we have chosen Hartree-Slater method. A sample input file (name: in36) for program RCN Mod 36 is

```

14 6 9 2 10 0.2 5.e-08 1.e-11-2 090 1.0 0.65 0.0 0.0 -6
14 1Si I 2p6 3s2 3p2 2p6 3s2 3p2
14 1Si I 2p6 3s2 3p2 2s1 2p6 3s2 3p2 99s 41.00
14 1Si I 2p6 3s2 3p2 2s1 2p6 3s2 3p2 99p 41.00
14 1Si I 2p6 3s2 3p2 2s1 2p6 3s2 3p2 99d 41.00
14 1Si I 2p6 3s2 3p2 2s1 2p6 3s2 3p2 99f 41.00
14 1Si I 2p6 3s2 3p2 2s1 2p6 3s2 3p2 99g 41.00
14 1Si I 2p6 3s2 3p2 2s1 2p6 3s2 3p2 99h 41.00
14 1Si I 2p6 3s2 3p2 2s1 2p6 3s2 3p2 99i 41.00
14 1Si I 2p6 3s2 3p2 2s1 2p6 3s2 3p2 99k 41.00
14 1Si I 2p6 3s2 3p2 2s1 2p6 3s2 3p2 99l 41.00
14 1Si I 2p6 3s2 3p2 2s1 2p6 3s2 3p2 99m 41.00
14 1Si I 2p6 3s2 3p2 2s1 2p6 3s2 3p2 99n 41.00
-1

```

The Cowan code was originally a Fortran punch-card program and is extremely specific about formatting, so every parameter has to be in the right column, or the code won't work. This sample input file for RCN Mod 36 to get ground and continuum states radial wave function of silicon, the continuum state with $\varepsilon = 41Ry$ for eleven ($l' = 0-10$) final angular momentums, separately. The first line is an almost universal control card, except that the "090" should be changed to "190" if relativistic corrections are desired. The radial wave function of ground electrons of silicon are shown in Fig. 2.5. The solid lines were calculated by Cowan code while the dotted lines were calculated by the well-known Herman-Skillman code for Hartree-Slater method. The wave functions are equal for each electron orbital. C. Dwyer calculated the bound and continuum wave functions of silicon by numerically integrating the radial Schrodinger equation for a Hartree-Slater potential using a

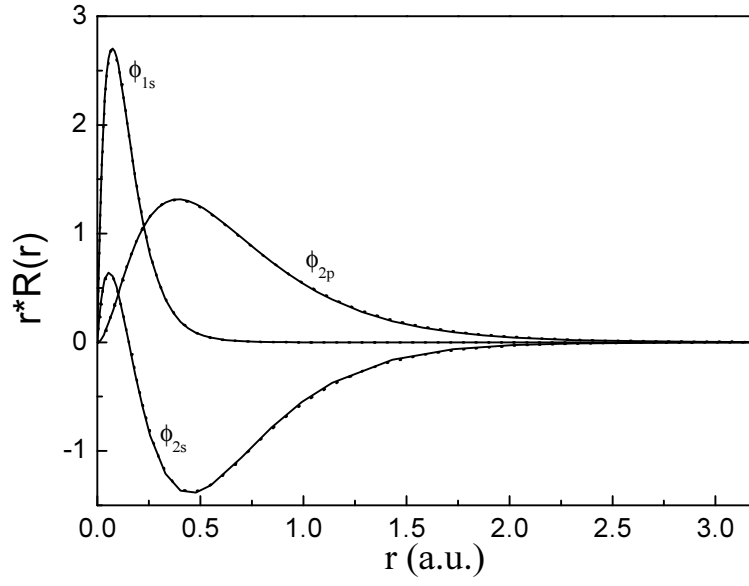


Figure 2.5 The radial wave function of silicon for core electrons 1s, 2s and 2p. The solid line obtained from Cowan code. The dotted line obtained from Herman-Skillman code.

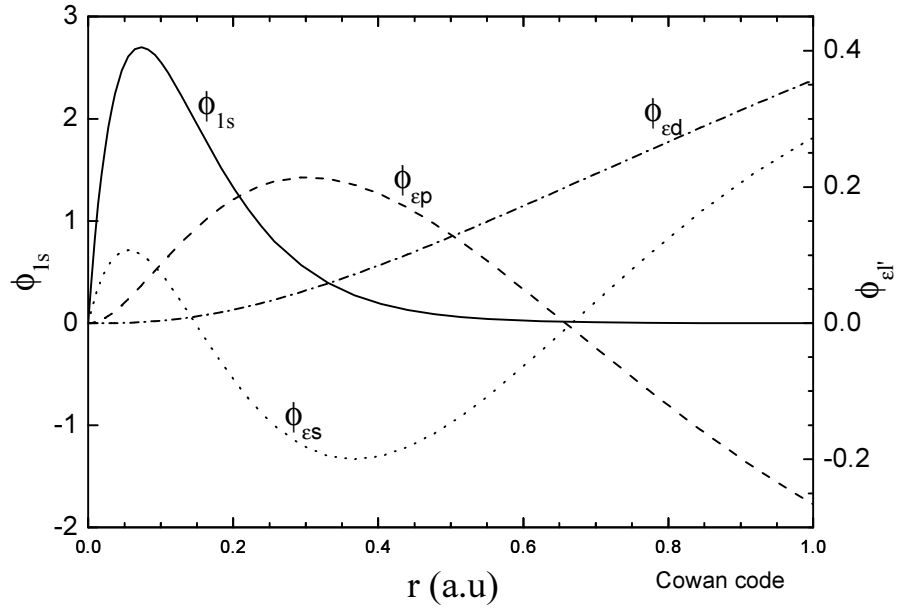


Figure 2.6 Radial wave function ϕ_{1s} for the silicon (solid line) and the continuum radial wave functions $\phi_{\epsilon l'}$ for an energy ϵ of 10 eV and angular momentum number $l' = 0, 1, 2$ obtained from Cowan code. The unit of length is the Bohr and Rydberg units energy. The same result has been obtained by numerically integrating the radial Schrodinger equation for a Hartree-Slater potential using a fourth-order Runge-Kutta method[46].

fourth-order Runge-Kutta method [46]. So we calculated the corresponding radial wave functions for silicon by Cowan code to verify their correctness. The results are displayed in Fig.2.6. Dwyer got the same figure in his publication [46]. From all of the foregoing, it is safe to conclude that we can trust our radial wave functions using Cowan code by the Hartree-Slater method.

2.3.3 $E \sim$ and $q \sim$ dependence of the GOS

The key quantity in electron inelastic scattering is the generalized oscillator strength (GOS) which is a function of both the energy loss E and momentum transfer q supplied to the atom.

The total GOS is calculated in terms of Eqs. (2.39) and (2.47) by summing over the final angular momentum l' , the number of partial waves of the final state can be estimated as follows : The final continuum wave function feels an effective potential can be written as:

$$V_{eff} = V(r) + \frac{l'(l'+1)\hbar^2}{2m_0 r^2}. \quad (2.48)$$

For large angular momentum l' , the second term is dominated. If the continuum energy is smaller than the centrifugal potential, the overlap between the initial wave function and the final continuum wave function is small and therefore these values of l' will contribute little to the total GOS. For example, if we assume most of the initial state is located within a distance a_0 (the first Bohr radius), then

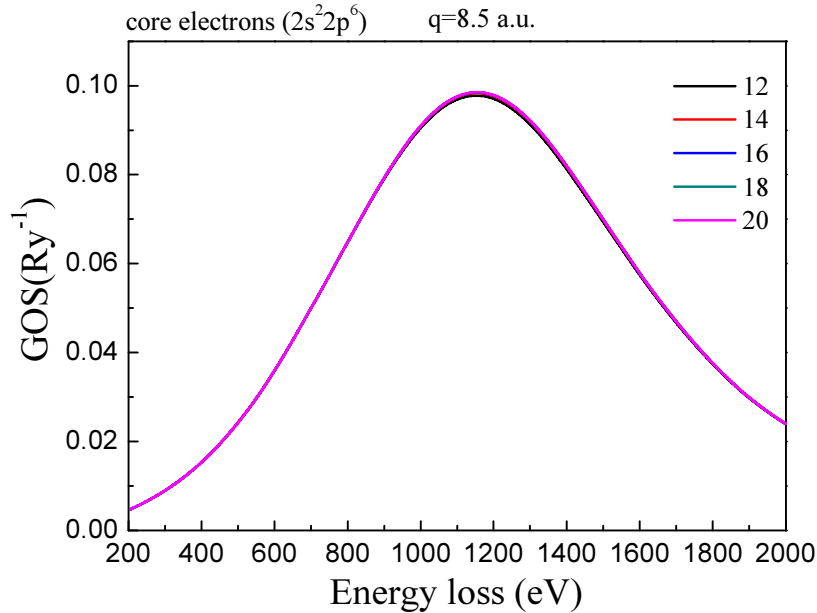


Figure 2.7 The GOS of silicon for transitions of core electrons at momentum transfer $q=8.5$ a.u., are shown for using the number of partial wave functions from 12 ($l'=0-11$) to 20 ($l'=0-19$).

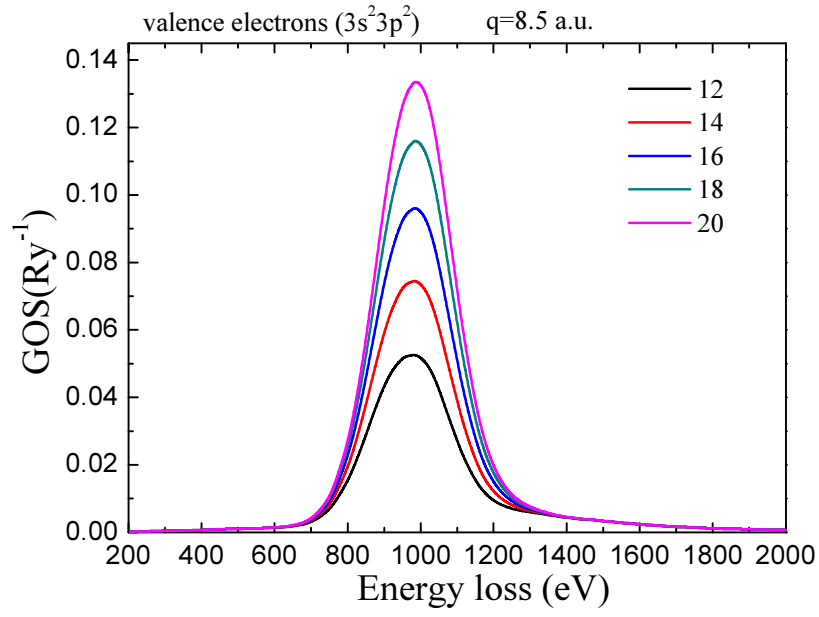


Figure 2.8 The GOS of silicon for transitions of valence electrons at momentum transfer $q=8.5$ a.u., are shown for using the number of partial wave functions from 12 ($l'=0-11$) to 20 ($l'=0-19$).

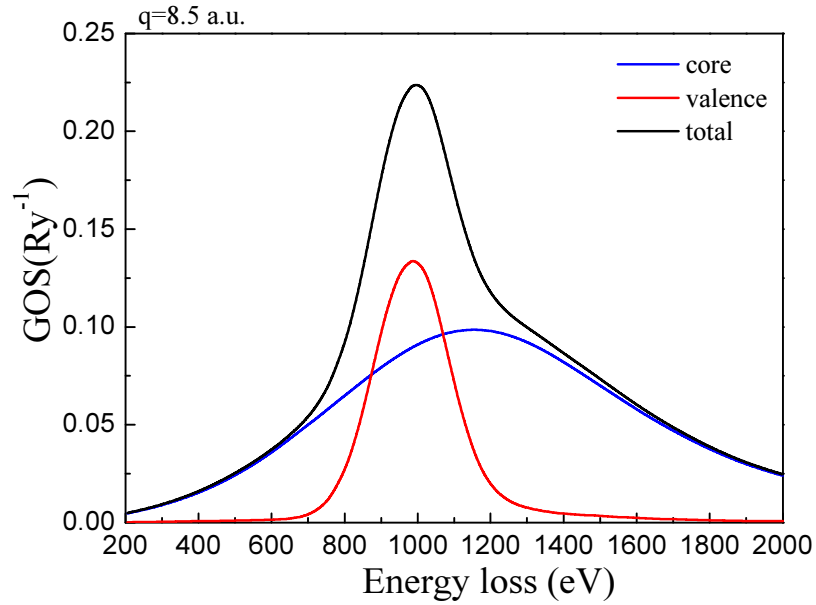


Figure 2.9 The total GOS of silicon for at momentum transfer $q=8.5$ a.u. along with the contributions of core electrons and valence electrons. The calculations for core electrons consider $l'=0-11$, while for valence electrons contributions consider $l'=0-19$.

$$\frac{l'(l'+1)\hbar^2}{2m_0r^2} \leq \varepsilon. \quad (2.49)$$

So, 10 partial wave functions are sufficed to describe the final continuum state with energy $\varepsilon = 1000eV$.

Fig 2.7 shows the calculated GOS for the core electrons of silicon using different number of final wave functions. The lineshapes don't change after using 12 final wave functions. The amplitude of valence orbitals is much larger than the size of core orbitals. It requires much more final wave functions for valence GOS calculation. In Fig. 2.8, the valence GOS of silicon is still not convergent, even we took 20 final wave functions. We can't obtain more than 20 final wave functions ($l' = s, p, d, f, g, h, i, k, l, m, n, o, q, r, t, u, v, w, x, y$) in the Cowan's code. Although the valence GOS of silicon isn't convergent at 20 final wave functions, the position of peak of the GOS doesn't shift after using 16 final wave functions. The total GOS of silicon at momentum transfer $q=8.5$ a.u along with core and valence contributions are shown in Fig. 2.9. Here we find that at so large momentum transfer the central peak of the total GOS mainly comes from transitions of valence electrons; conversely, core electrons contribute mainly to the wings of the spectrum. This is a typical characteristic of the Compton scattering [38, 47].

In Fig. 2.10 the Silicon 2p GOS's for $\varepsilon = 0.1eV$ and $120eV$ are shown along with the contributions from each individual final continuum angular momentum state (l'). For small ε , Fig.2.10(a), we can see the contributions from higher partial waves ($l' \geq 3$) are negligible, because their high angular momentum number makes the centrifugal barrier insurmountable at low energies. The $l'=3$ wave, which has essentially no effect at near threshold ($\varepsilon = 0.1eV$), penetrates far enough to have a significant effect at large momentum transfer for high continuum energy as shown in Fig. 2.10(b). At higher energies, the continuum wave function can penetrate the barrier much more easily; on the other hand, the continuum function moves further results in the overlap with the initial wave function becomes small. Typically, different numbers of partial waves are required for final state with different continuum energy.

The transition from an initial state with the angular momentum l to a final state with the angular momentum l' is called a "channel". In the limit $q \rightarrow 0$, only the optical dipole selection rule with $\Delta l = \pm 1$ ($\Delta l = l - l'$) make contribution to the GOS. In Fig. 2.10, we can find that the dipole transition channels $2p \rightarrow \varepsilon s (l' = 0)$ and $2p \rightarrow \varepsilon d (l' = 2)$ give contributions to the GOS, as $q \rightarrow 0$. While the monopole transition $2p \rightarrow \varepsilon p (l' = 1)$ produces significantly contribution only at large momentum transfer. These behaviors can be easily understood by expanding the exponential operator in the transition matrix element as:

$$\exp(i\vec{q} \cdot \vec{r}) = 1 + i(\vec{q} \cdot \vec{r}) - \frac{1}{2!}(\vec{q} \cdot \vec{r})^2 + \dots. \quad (2.50)$$

The transition matrix element can be split in three componets. The first term in the

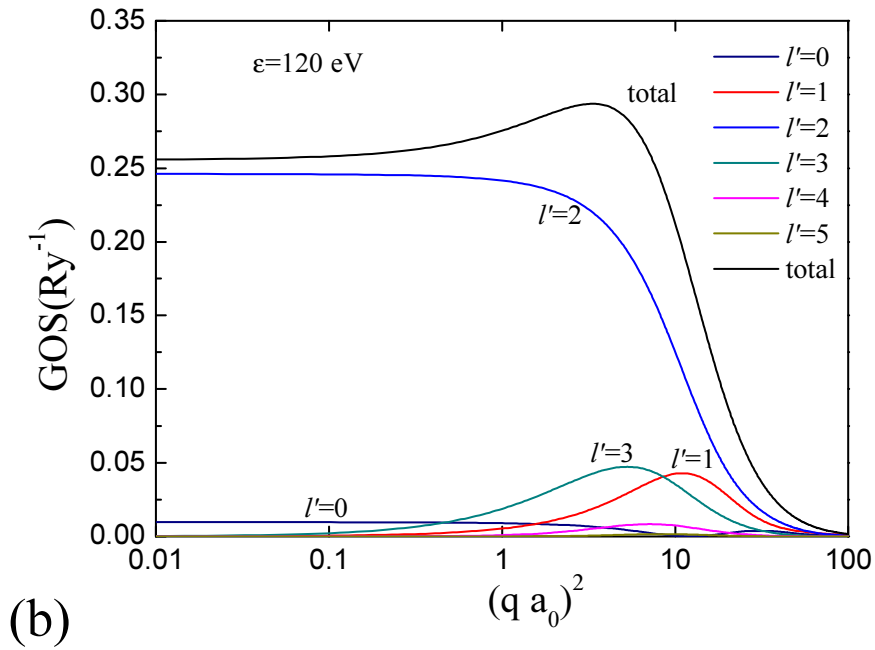
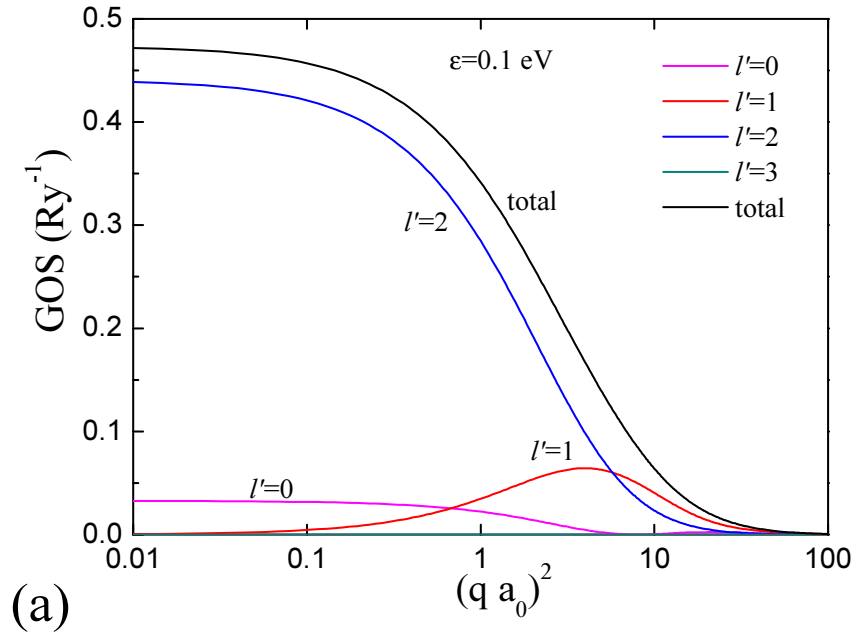


Figure 2.10 Contribution to the Silicon 2p GOS by various continuum angular momentum channels for ionization at (a) $\varepsilon = 0.1 \text{ eV}$ and (b) $\varepsilon = 120 \text{ eV}$.

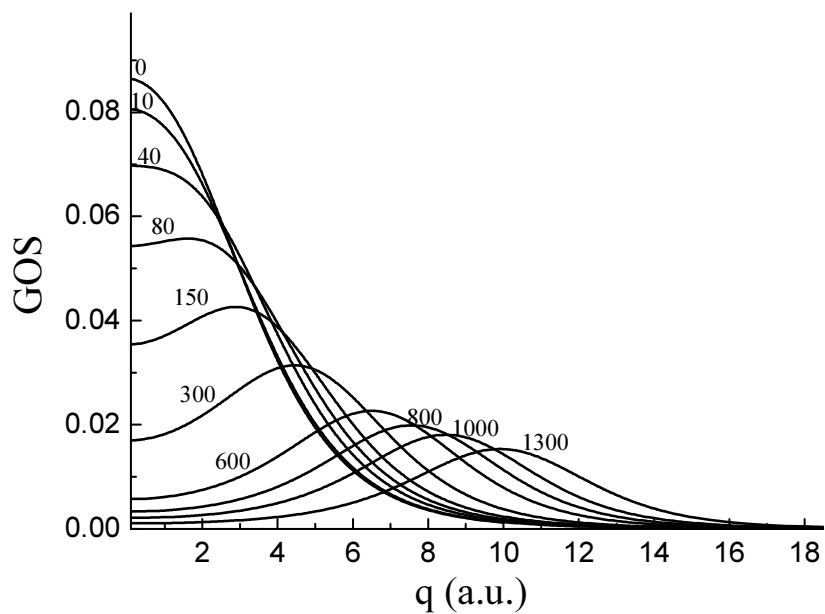


Figure 2.11 The GOS of carbon for the transition from 1s shell to the continuum energy $\mathcal{E}=0, 10, 40, 80, 150, 300, 600, 800, 1000$ and 1300 eV.

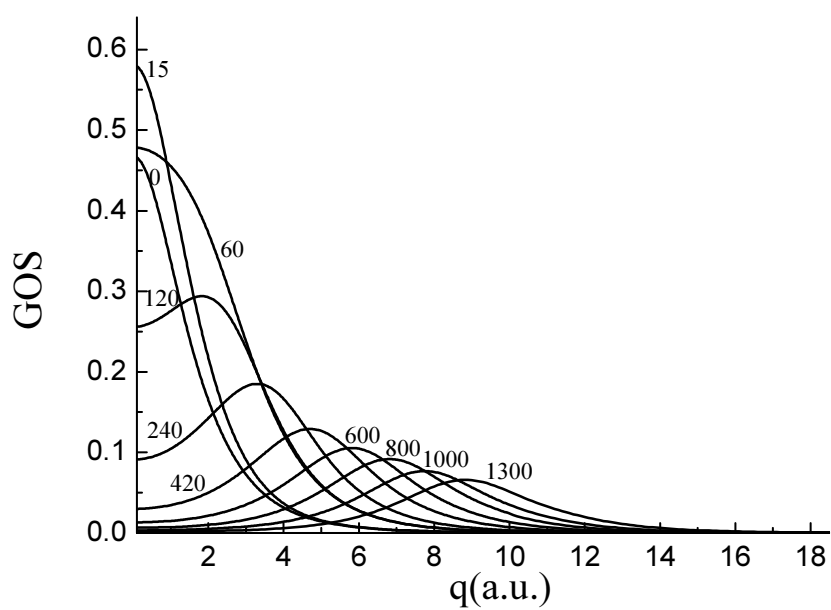


Figure 2.12 The GOS of silicon for the transitions from 1s shell to the continuum energy $\mathcal{E}=0, 15, 60, 120, 240, 420, 600, 800, 1000$ and 1300 eV.

matrix element is zero due to the initial state $|nl\rangle$ and final state $|\epsilon l'\rangle$ are orthogonal. The second term is zero if the initial state $|nl\rangle$ and the final state $|\epsilon l'\rangle$ have same symmetry about the center of the excited atom ($r=0$) such that their product is even; and $\vec{q}\cdot\vec{r}$ is an odd function. The integration of the second term will be canceled. In the case of the initial state and final state have differential symmetry, like the initial state $|nl\rangle$ is an s -state (even symmetry) and the final state $|\epsilon l'\rangle$ is a p -state (odd symmetry), the second term is nonzero and transitions are observed. In the low momentum transfer limit ($qa_0 \ll 1$), only the second term is important, so mostly dipole allowed transition are recorded. When the momentum transfer is increased, other terms in Eq. (2.50) become more important, dipole-forbidden transitions can be probed [44, 48, 49]. When the momentum transfer is larger than the inverse of electronic orbital size and energy transfer is much large relative to the binding energy of the electron shell, the Compton scattering peak appears locating at far away from ionization edge. The ground state electron momentum density distribution can be probed in the experiment [3, 32].

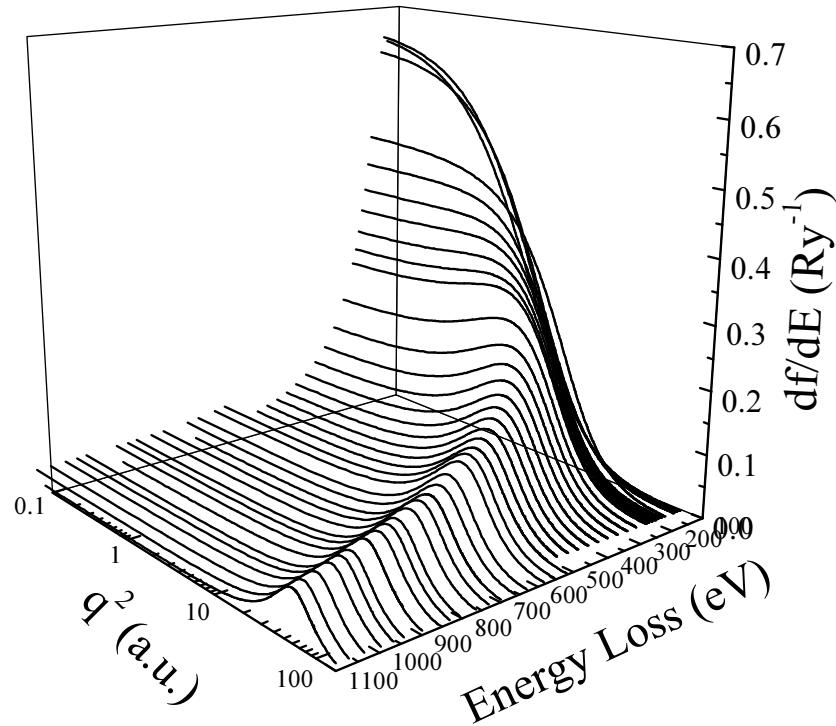


Figure 2.13 Bethe surface for 2p-shell ionization of silicon, calculated by a Hartree-Slater method.

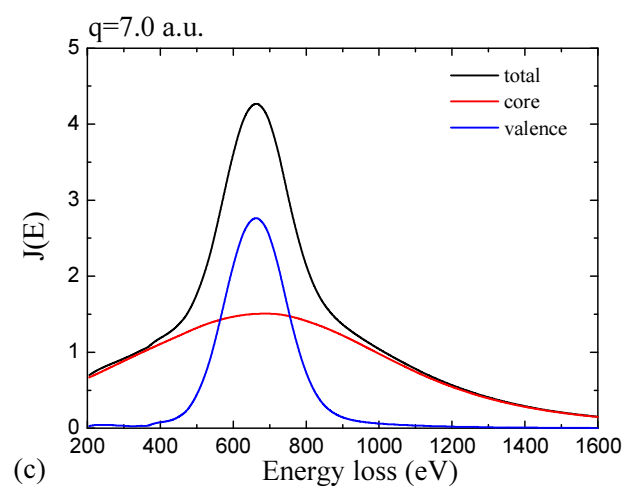
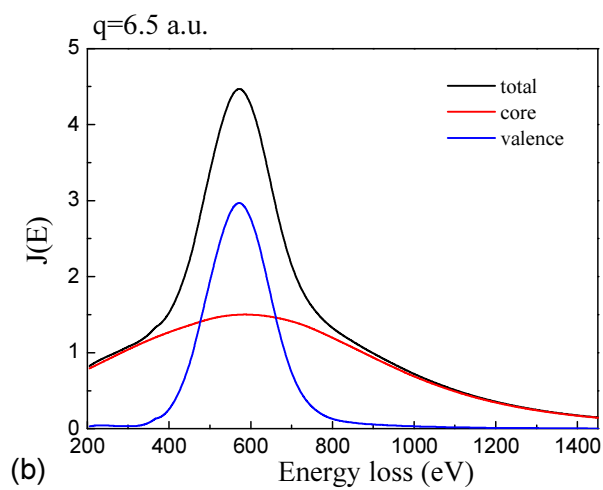
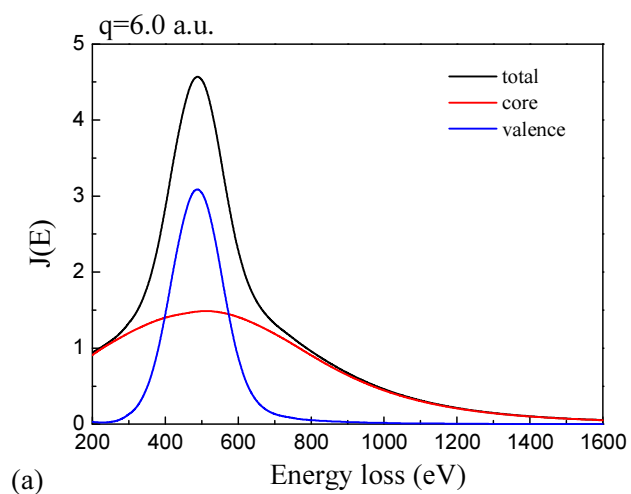
Fig.2.11 shows the calculated GOS for 1s electrons transition of carbon at a series of continuum energies ϵ . For small ϵ , the maximum of each curves is at $q=0$, so the contributions mainly come from dipole transition $1s \rightarrow \epsilon p$. The GOS's at $q=0$ decrease monotonously with increase the continuum energy ϵ . This behavior results in a sawtooth-shape of K edge in EELS. Fig. 2.12 shows the computed GOS for 2p shell transitions of silicon at a number of continuum energies ϵ . For small ϵ , the maximum of each curves is also at $q=0$, as shown in Fig. 2.10, the dominance of the peak comes for dipole transition $2p \rightarrow \epsilon s(l'=0)$ and

$2p \rightarrow \varepsilon d (l' = 2)$. Note that not as K shell transition of carbon, the GOS of silicon at $q = 0$ rises till $\varepsilon \sim 20 \text{ eV}$ then decreases when continuum energy increases. This is the origin of a delayed maximum in EELS for L edge.

For larger ε — large energy loss — the optically forbidden channels become important, the maximum of curve is out of $q = 0$ and moves to higher momentum transfer with increasing continuum energy. If the GOS is plotted in three-dimensional as a function of energy transfer and momentum transfer, these maximums consist the famous Bethe surface. The Bethe surface for 2p shell ionization of silicon is shown in Fig. 2.13. A cross section of the Bethe surface at a fixed momentum transfer is Compton profile [50]. So these maximums can be interpreted in the impulse approximation. First, consider a scattering process in which energy transfer is much larger than the binding energy of atomic electrons. Then, role of the binding energy must plays relatively insignificant, and scattering electron will receive the energy transfer as same it was free. The GOS of the scattering electrons are then peaked at a momentum transfer given by

$$\frac{\hbar^2 q^2}{2m_e} \simeq \varepsilon. \quad (2.51)$$

2.3.4 The electron Compton profile



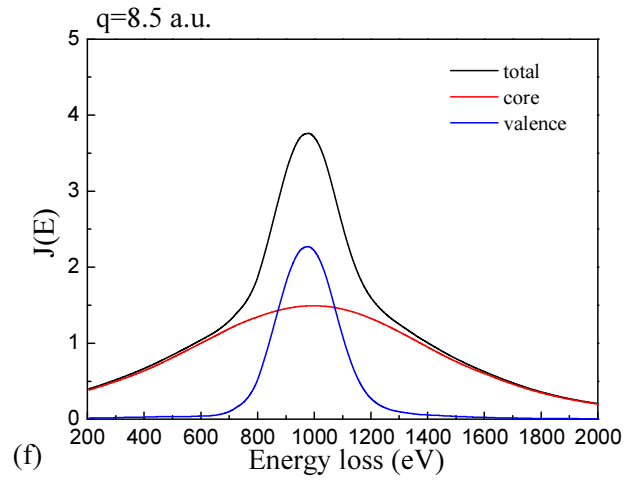
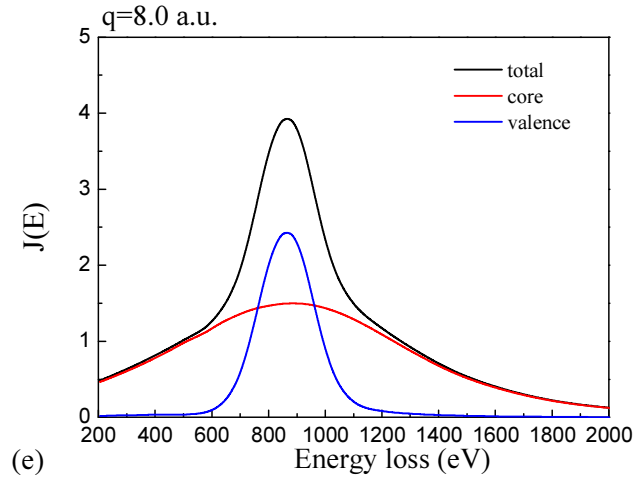
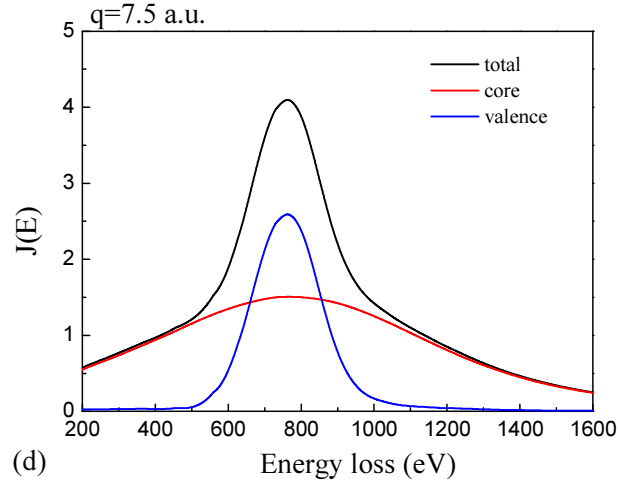


Figure 2.14 The Compton profile of Silicon as a function of energy loss at momentum transfer $q=6.0, 6.5, 7.0, 7.5, 8.0$ and 8.5 a.u. The red line is the core Compton profile, the blue is the valence Compton profile and the black line is the total Compton profile.

In a typical Compton scattering experiment, the valence Compton profile is obtained from experimental data only after a theoretical core electron contribution subtraction is performed. It is a substantial procedure to separate the core Compton profile from that of the valence electrons. We calculated the Compton profile of silicon for both core and valence electrons as shown in Fig. 2.14 at momentum transfers from 6.0 to 8.5 a.u.. 12 final wave functions were used for core Compton profile calculation while for valence Compton profile we took 20 final wave functions. From Fig. 2.14, we see that when the scattering is observed summed over all electrons in the atom, the center of the peak is largely determined by the narrow momentum density distribution of the valence electrons ($3s^2$ and $3p^2$), whereas the wings are mainly due to the broad core electrons ($2s^2$ and $2p^6$) distributions. In solids, the momentum distribution of the valence electrons is substantially different from that of electrons in a free atom. The momentum distributions of the core electrons, however, are very similar for solids and free atoms. Therefore, a Hartree-Slater free atom calculation is sufficient to determine the contributions of the core electrons to the total Compton profile. The theoretical core contribution of the Compton profile is then normalized by fitting at the tails of

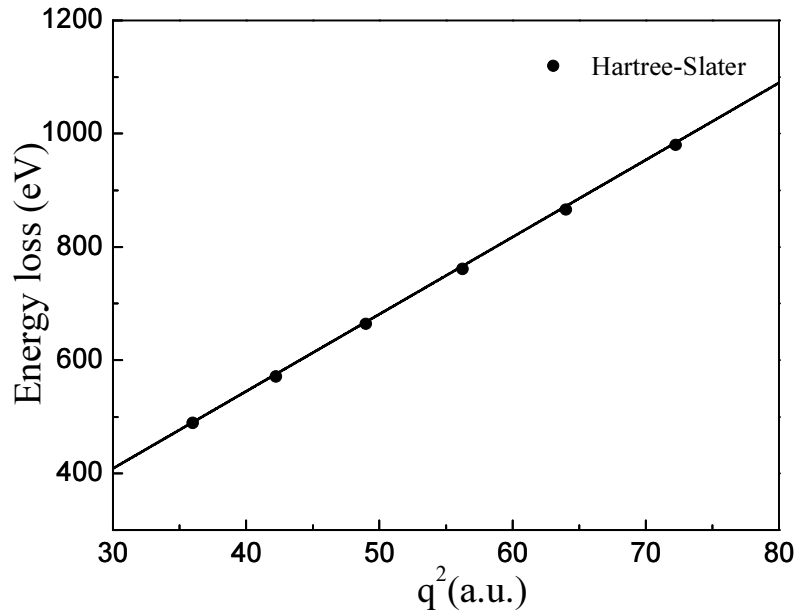


Figure 2.15 The momentum transfer dependence of the energy-loss of electron Compton peak by

Hartree-Slater calculations. The black line comes from free electron model $E = \frac{q^2}{2m_e}$.

the total Compton profile where the valence contributions are negligible. The Compton profile shift to higher energy loss with increasing momentum transfer. The energy-loss of Compton peaks with respect to square of the momentum transfers are plotted in Fig. 2.15. Note that the dispersion relation looks much like that the scattering from a free electron.

Chapter 3

ECOSS experiment

In this chapter, an overview is given of the transmission electron microscope for the electron Compton scattering from solids. Bragg scattering provides an accurate scaleplate in recording EELS at chosen angle. ECOSS measurement can be carried out by the spectrometer at large scattering angle. The background subtraction is also introduced in this chapter.

3.1 Transmission electron microscope (TEM)

The transmission electron microscope (TEM) has proven to be a very powerful tool to study the structure of matter in nanometer range. In 1932, the first TEM was constructed by Ernst Ruska. Fifty-four years later, Ruska received the Nobel Prize in physics in 1986 for his work on developing the electron microscope and microscopy. Here we briefly summarize the basic design of TEM, which has relevance to the experimental use of EELS measurement. Most of experimental results in this thesis have been obtained in Tecnai F20 microscope.

3.1.1 Basics of the TEM

Fig. 3.1 shows the basic components inside of the Tecnai F20 microscope. Firstly, at the top of the column is the electron source, which is one of the most important parts of a TEM. There are two major types of electron source: thermionic and field emission sources (or called “gun”). The tungsten filaments (now rarely) or lanthanum hexaboride (LaB_6) tips (now commonly) are used in thermionic source. The field emitters are fine tungsten needles. The type of electron gun determines the brightness, the source size, energy spread and so on. Table 3.1 gives an overview of the characteristic of the different electron sources. Field emission guns (FEG) operate in ultra-high vacuum conditions and are around twice as expensive as thermionic electron guns. They are available for applications in which a high brightness and low energy spread of incident electrons.

The electrons from the gun are accelerated by the high voltage, typically the final beam energy is between 60 and 200 keV in our microscope. The condenser system consists of two lenses (C1 and C2) and transfers electrons to the specimen giving either a broad beam or a focused beam. For the first condenser C1 (*spot size* in control software) produces a demagnification of the source, while the second condenser C2 (*intensity* on control panels) controls the size of the spot on the sample and hence produces a parallel, divergence or convergence incident beam. Deflection coils ensure that the beam remains parallel to the optic axis. EELS can be recorded at different scattering angle in diffraction condition by tilting the beam using the dark-field

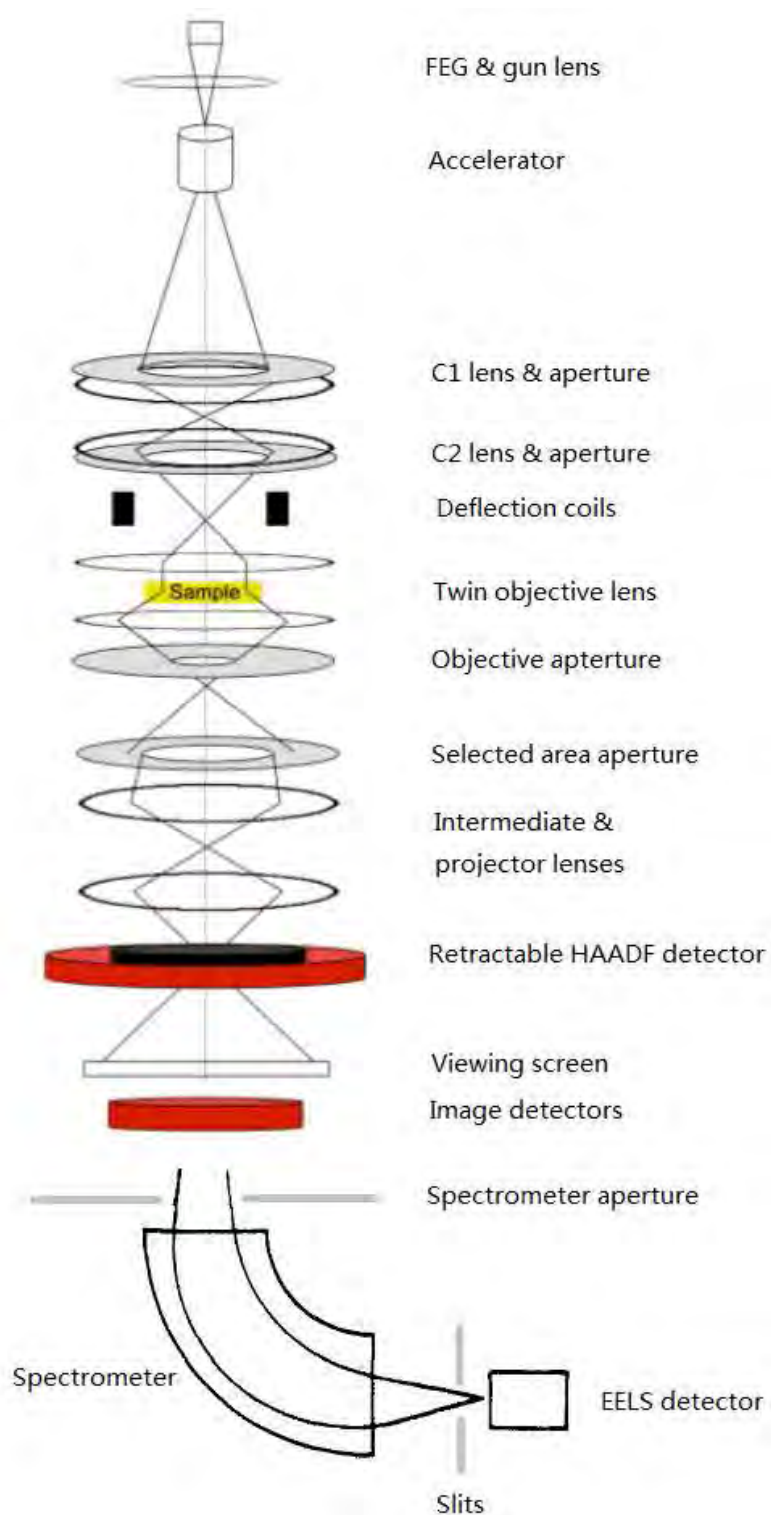


Figure 3.1 Schematic diagram of the basic components within the Tecnai F20 microscope. Figure adapted from Pearmain [51].

Table 3.1 Characteristic of different electron sources (at 100 kV) [52].

	Units	Tungsten	LaB ₆	Schottky FEG	Cold FEG
Work function	eV	4.5	2.4	3.0	4.5
Current density	A/m ²	5	10 ²	10 ⁵	10 ⁶
Brightness	A/m ² sr	10 ¹⁰	5×10 ¹¹	5×10 ¹²	10 ¹³
Crossover size	nm	>10 ⁵	10 ⁴	15	3
Energy spread	eV	3	1.5	0.7	0.3
Emission current stability	%hr	<1	<1	<1	5
Vacuum	Pa	10 ⁻²	10 ⁻⁴	10 ⁻⁶	10 ⁻⁹
Temperature	K	2700	1700	1700	300
lifetime	hr	100	1000	>5000	>500

deflection coils. The objective lens can form images (in the image plane of the lens) and the corresponding reciprocal space diffraction pattern (in the back focal plane of the lens). The objective aperture is placed in the back focal plane of the objective lens. Its function is to select which electrons (transmitted electrons or diffracted beams) to form image and improve the contrast of the final image. The selected area aperture can be inserted in the image plane of the objective lens to limit the area from which diffraction pattern is acquired. The intermediate and projector lens system is used to magnify image or the electron diffraction pattern formed by the objective lens. The camera and EELS spectrometer (even lower) are attached to the end of the microscope column.

3.1.2 Electron-specimen interaction

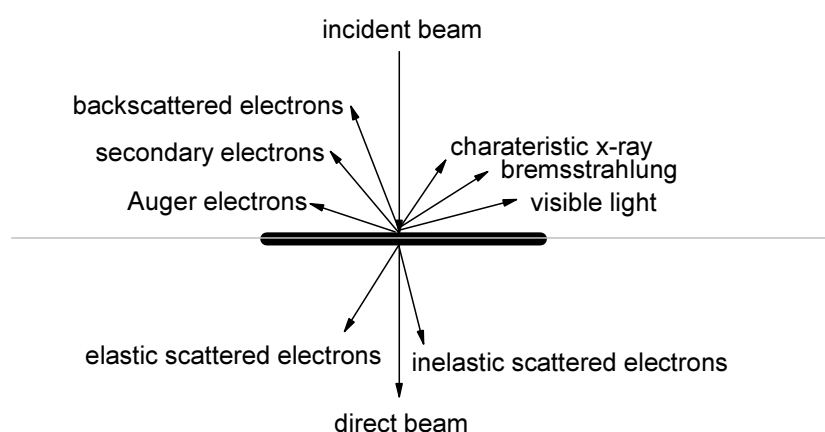


Figure 3.2 Different kinds of electron scattering when transmission high energy electron beam pass through a thin solid sample

When an electron beam interacts with the atoms in the specimen, the incident electrons will produce various effects resulting in a range of signals being emitted. These effects are mainly the various electrons or electromagnetic radiation shown in Fig. 3.2. Scattering can be either forward scattering or back scattering. In our work, we will focus on the forward scattering electrons (incident beam goes through a specimen). The scattering of the incident beam electrons were divided into elastic and inelastic components. Elastic scattered electrons can be thought as only changed their original path, but with no loss of energy. Inelastic scattered electrons are the same but with loss energy. Inelastic scattering distribution is analyzed by EELS technique. Bragg's law describes the condition for elastic scattering, i.e., the diffraction patterns of elastic scattered electrons from crystal shown in Fig. 3.3.

$$n\lambda = 2d \sin \theta_B, \quad (3.1)$$

where n is an integer number, λ is wave length of incident beam, d is the lattice plane distance and θ_B is the Bragg angle. The diffraction patterns provide information of the crystal structure, orientation etc. of materials. Bragg angle provides an accurate scaleplate in recording EELS at chosen scattering angle. The electron Compton peak can be found at an scattering angle about 60mrad in the higher energy loss region of EELS.

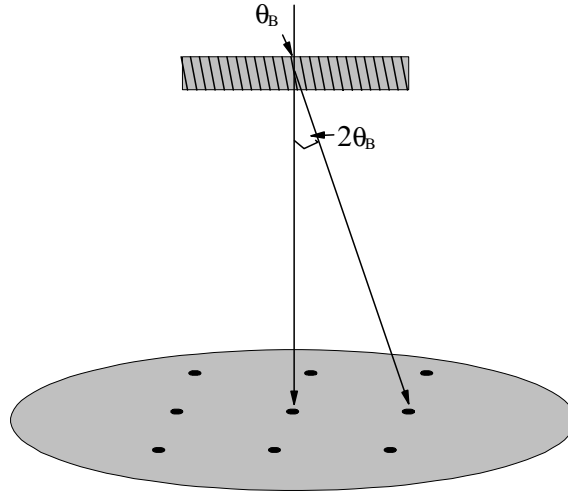


Figure 3.3 Elastic scattering of the incident electron beam from crystal in a TEM.

3.2 EELS instrumentation

Electron energy-loss spectroscopy involves analyzing the energy distribution of electrons after they have interacted with a specimen. These inelastic scattering

electrons with different energy can be separated by the magnetic-prism spectrometer. EELS experiment can be carried out with a conventional TEM operating either in imaging mode or in diffraction mode.

3.2.1 The magnetic-prism spectrometer

In this thesis, the EELSs were acquired with a Gatan Imaging Filter (GIF), Tridie -m spectrometer on Tecnai F20 microscope. The primary of the GIF spectrometer is the magnetic-prism, see Fig. 3.4. In the magnetic-prism spectrometer, electrons with a speed v travel through a magnetic field B , which is generated by an electromagnet with particular shaped polepieces. Within this field, electrons follow a circular orbit of radius R and are deflected through an approximate 90° angle. The force exert on an electron is

$$F = Bev = mv^2/R, \quad (3.2)$$

where e and m are charge and relativistic mass of electron. The bend radius depends on velocity or in other word, on electron energy:

$$R = (m/e) Bv. \quad (3.3)$$

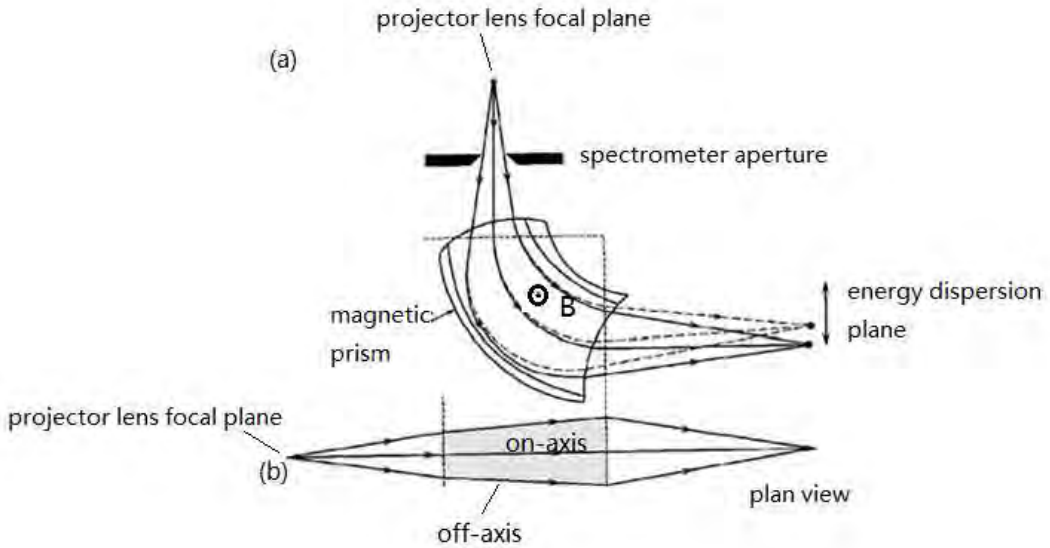


Figure 3.4 Schematic diagram showing the dispersive and focusing principle of a magnetic-prism. (a) the plane perpendicular to the magnetic field (b) in the plane parallel to the magnetic field. Figure adapted from Egerton [33].

The primary electrons suffer the large energy loss will be deflected the greater angle, whilst the electrons without loss energy will be deflected the smallest angle. Electrons suffer the same energy loss but travel in on-axis or off axis path, the magnetic field also brought them back to a focus in the energy dispersion plane of the spectrometer (Fig.3.4 (b)). Finally, the dispersion of the electron beam is recorded by

the CCD array.

3.2.2 Operation modes

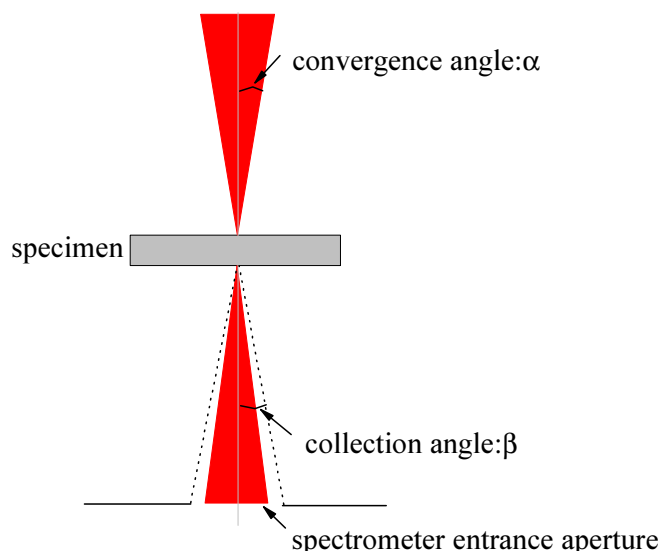


Figure 3.5 The definition convergence angle α and collection angle β in a TEM. Figure adapted from Maigne [53].

EELS measurements can be performed either in image mode or in diffraction mode. Here we deal with experimental parameters directly relevant to EELS, the convergence angle α and the collection angle β (we really mean semi-angle). The definition of α and β is shown in Fig. 3.5. In any EELS analysis and comparison with theory, these two angles must be clear and given. The convergence angle governs the condition of the incident beam on the specimen. Use of parallel or focused illumination by adjusting the condenser lens—this controls the collection angle and the analysis area of the specimen. The convergence angle α can be determined by measuring the angular width of diffraction discs from a specimen with a known Bragg angle θ_B , as shown in Fig. 3.6. The collection angle is affected by your choice of operating mode, and so we will briefly introduce how to determine β under different operations.

EELS in diffraction mode

This mode is the most useful way to measure EELS spectra. In TEM diffraction mode, EELS can be recorded at chosen scattering angle with small collection angle. In this

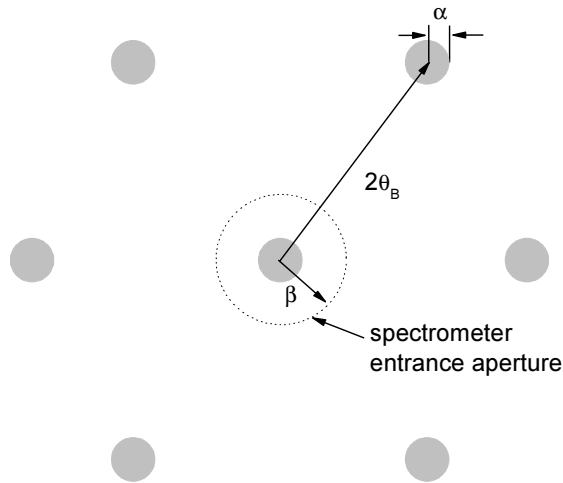


Figure 3.6 Determination of angles with a GIF camera [53].

case, the collection angle β is governed by the size of the entrance aperture and the camera length. The EELS in diffraction mode allows the regions of diameter down to 1 nm on sample can be investigated by using a very small probe. Alternatively, diffraction mode provides high intensity (useful for core loss and Compton spectroscopy) because the spectrometer entrance aperture doesn't limit the entire beam. In diffraction mode, usually, the direct beam of the diffraction pattern must be aligned to the center of the spectrometer entrance aperture.

EELS in image mode

In TEM image mode, a magnified image of the specimen is presented on the viewing screen. The angular distribution of electrons entering the spectrometer is independent of the size of entrance aperture. This is because the angular distribution of electrons contributing to image governs by the objective aperture. The objective aperture determines the collection angle in this mode. In TEM image mode, it is easy to align and can be used for quick inspection of a specimen.

3.3 ECOSS in TEM

If we measure EELS at large scattering angle, the electron Compton scattering peak appears at high energy loss region which lies far away from ionization edge as shown in Fig. 3.7. This broad peak is known as the electron Compton scattering from solid (ECOSS) in TEM [32]. The momentum resolution and background subtraction of

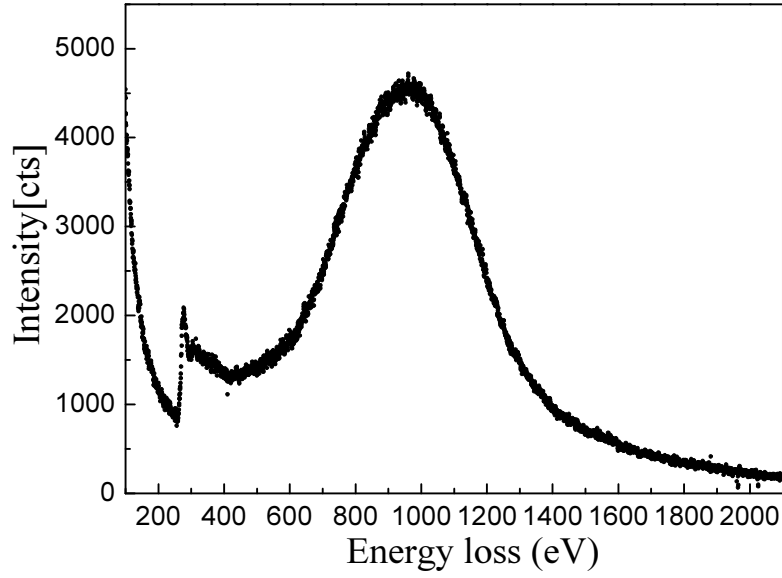


Figure 3.7 Experimental EELS of graphite at scattering angle $\theta = 64 \text{ mrad}$. The convergence angle $\alpha = 3.5 \text{ mrad}$, the collection angle $\beta = 1.2 \text{ mrad}$, the thickness of sample is 20 nm and total exposure time is 50 s. The carbon K-edge is also clearly visible at 284 eV.

ECOSS will be discussed in the following section.

3.3.1 Momentum resolution

Momentum resolution is a critical factor which invariably governs the quality of the Compton scattering experiment. The total momentum resolution Δp in ECOSS experiment is governed not only by the energy resolution of EELS, but also by the convergence angle of the incident beam and by the collection angle of measurement. Here we only describe how the energy resolution affects the momentum resolution in the ECOSS experiment. Details of these can be found in literature of P. Jonas et al [34, 54].

Energy resolution

The energy resolution of EELS is defined as the full width at half maximum (FWHM) of the focused zero-loss peak, as shown in Fig. 3.8. The type of electron source of TEM determines the resolution. At 100 keV, a tungsten filament source has the worst resolution (the best resolution $\sim 3 \text{ eV}$), a LaB₆ tips is slightly better $\sim 1.5 \text{ eV}$ (the best resolution), a Schottky field emission source can give $\sim 0.7 \text{ eV}$ (the best resolution) and a cold FEG gives the best resolution $\sim 0.3 \text{ eV}$ [52]. In our ECOSS measurement, the energy resolution is 2.5 eV at the energy dispersion of 0.5 eV/channel. The momentum resolution due to energy resolution can be determined by differentiating Eq. (2.25):

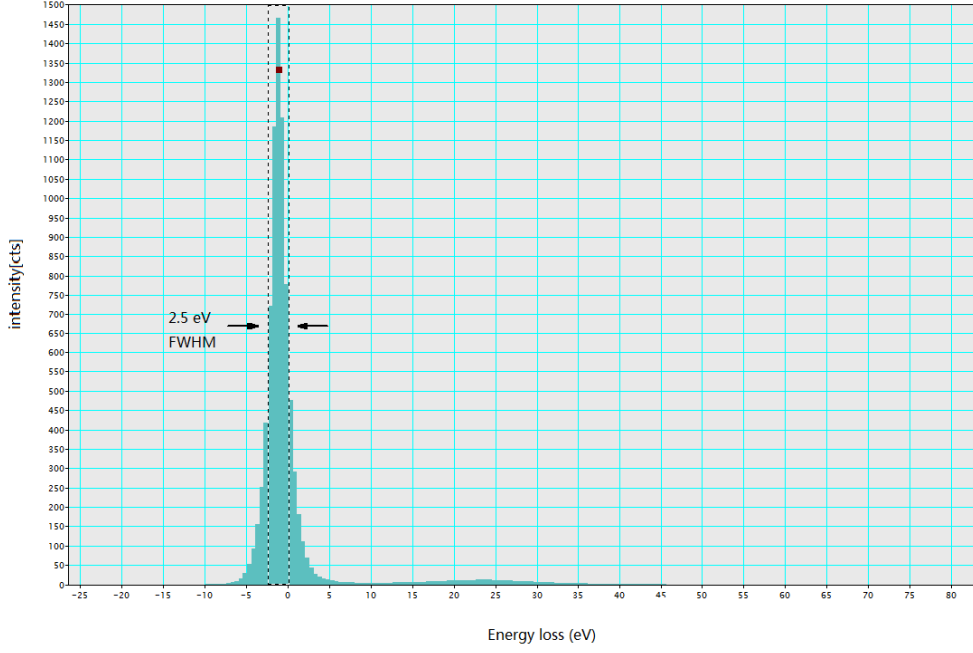


Figure 3.8 The energy resolution of EELS for ECOSS measurement. The energy dispersion of 0.5 eV/channel was chosen.

$$\delta p_q = \delta E \left[\frac{2E_{\max}}{m_e} \right]^{-1/2}. \quad (3.4)$$

So the momentum resolution which is obtained from energy resolution also depends on the energy loss of Compton peak. δp_q decreases with increasing the recording scattering angle (E_{\max} becoming larger). For an energy loss to the Compton peak of 1000 eV, the momentum resolution due to energy resolution is $\delta p_q = 0.01 a.u.$

3.3.2 Background subtraction

As is well known, proper background subtraction is a critical process in EELS analysis. Usually, a power-law type background is removed for EELS in near edge region. It is assumed that the energy dependence of background follows the form

$$B = A E^{-r}, \quad (3.5)$$

where B represents background, E is the energy loss, and A and r are two free parameters. It is found that the exponent r is related to experimental conditions like specimen thickness, collection angle, width and location of the energy window. The fitting parameters (A and r) can be determined by least-squares methods or the by two-area method. The r is typically in the range 2~5, but amplitude A can be very tremendously. The experimental raw data for carbon K-edge in graphite along with the power-law background are shown in Fig. 3.9.

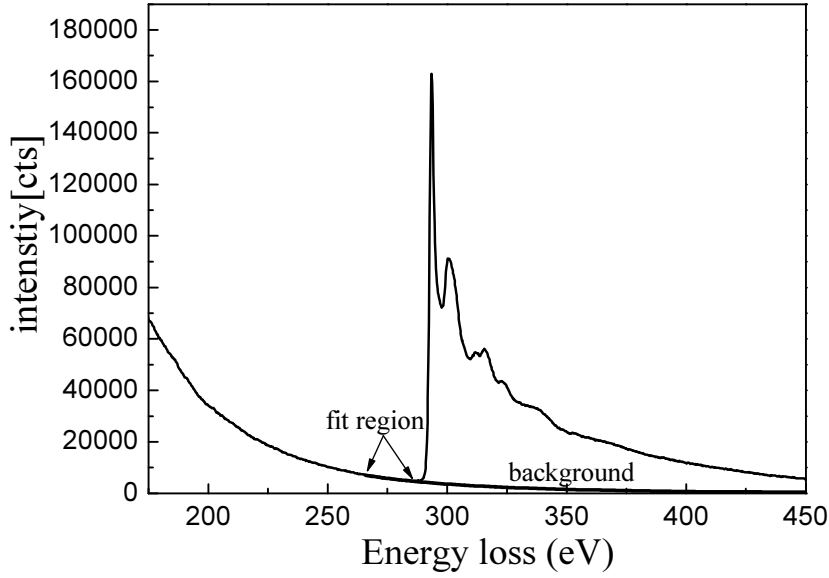


Figure 3.9 The measured carbon K-edge in graphite in the direction along c axis along with power-law type bakground. The specimen thickness 20 nm, collection angle $\alpha = 0.3 \text{ mrad}$. The fitting parameter $r \approx 4$ for background subtraction.

However, the quality of the power-law background decreases with increasing the distance from the fitting window, the fitting parameters A and r are only valid over ~ 100 eV. In ECOSS, the energy loss region of the electron Compton scattering extends over some 100 eV, so the power-law tape background will not work. On the other hand, the large cross section for electron Compton scattering also brings a huge background which easily submerges the Compton signal. The background problem is the major disadvantage of ECOSS measurement compared to photon Compton scattering experiment.

The background results from all the possible scattering events whose energy loss less than the Compton scattering profile and the combination of all those events, including multiple scattering and channeling of different scattering events. Multiple scattering of electrons in the sample after passing a layer of thickness t of a homogeneous medium can be described by the Wentzel summation method in the form of a single scattering function $f(E, \theta)$ [55]. The Poissonian probability distribution for n -fold scattering events can be used for the further calculation[56]. The probability of an electron to be scattered is

$$P(E, \theta) = \sum_{n_1=0}^{\infty} \sum_{n_2=0}^{\infty} \dots \sum_{n_m=0}^{\infty} P_{n_1, n_2, \dots, n_m} F_{n_1, n_2, \dots, n_m}(E, \theta), \quad (3.6a)$$

$$P_{n_1, n_2, \dots, n_m} = \left(\frac{D_1^{n_1}}{n_1!} e^{-D_1} \right) \left(\frac{D_2^{n_2}}{n_2!} e^{-D_2} \right) \dots \left(\frac{D_m^{n_m}}{n_m!} e^{-D_m} \right), \quad (3.6b)$$

$$F_{n_1, n_2, \dots, n_m} = \underbrace{f_1 * f_1 * \dots * f_1}_{n_1} * \underbrace{f_2 * f_2 * \dots * f_2}_{n_2} * \dots * \underbrace{f_m * f_m * \dots * f_m}_{n_m}. \quad (3.6c)$$

The integers 1 to m denote the different single scattering events under consideration, D_m is the thickness of specimen in the units of the mean free path length λ_m of the scattering event m , P_{n_1, n_2, \dots, n_m} is the respective partial scattering probability, and $*$ means convolution.

In Fourier space, a total energy and angular distribution of the scattered electrons in an isotropic medium can be written

$$\tilde{P}(\omega, \rho) = e^{D \cdot (\tilde{f}(\omega, \rho) - 1)}, \quad (3.7a)$$

$$\tilde{f}(\omega, \rho) = \int_0^\infty \int_0^\pi f(E, \theta) e^{-iE\omega} J_0(\theta\rho) dE d\theta. \quad (3.7b)$$

The procedure is a Fourier transform with respect to the energy variable ($E \rightarrow \omega$) and a Hankel transform of zero order with respect to the angular variable ($\theta \rightarrow \rho$). Where J_0 is the zero-order Bessel function of the first kind, and D is the specimen thickness t in the units of total mean free path length

$$D = \sum_{i=1}^m D_i = \sum_{i=1}^m \frac{t}{\lambda_i}. \quad (3.8)$$

To perform an more detailed analysis of the different scattering events taking place, it is convenient to separate the above solution into components according to the properties of each scattering process and rewrite Eq. (3.6a)

$$\tilde{P}(\omega, \rho) = \tilde{P}_0 + \tilde{P}_e + \tilde{P}_i + \tilde{P}_{i,e}, \quad (3.9)$$

where

$$\tilde{P}_0 = e^{-(D_e + D_i)}, \quad (3.10a)$$

$$\tilde{P}_e(\rho) = e^{-(D_e + D_i)} \cdot \left(e^{[D_e \tilde{f}_e(\rho)]} - 1 \right), \quad (3.10b)$$

$$\tilde{P}_i(\omega, \rho) = e^{-(D_e + D_i)} \cdot \left(e^{[D_i \tilde{f}_i(\omega, \rho)]} - 1 \right), \quad (3.10c)$$

$$\tilde{P}_{i,e}(\omega, \rho) = e^{-(D_e + D_i)} \cdot \left(e^{[D_i \tilde{f}_i(\omega, \rho)]} - 1 \right) \cdot \left(e^{[D_e \tilde{f}_e(\rho)]} - 1 \right); \quad (3.10d)$$

here P_0 describes the unscattered beam, P_e is the angular distribution of pure elastic scattering, P_i is the energy and angular distribution of pure inelastic scattering and $P_{i,e}$ is the distribution of combined elastic and inelastic scattering. Going a step further, we can separate the inelastic scattering into a low energy-loss part (plasmon scattering) and a high energy-loss part (core electrons and Compton scattering):

$$\tilde{P}_i(\omega, \rho) = \tilde{P}_p(\omega, \rho) + \tilde{P}_c(\omega, \rho) + \tilde{P}_{p,c}(\omega, \rho) \quad (3.11)$$

and similar equations as Eq. (3.10). The total scattering distribution in real space is

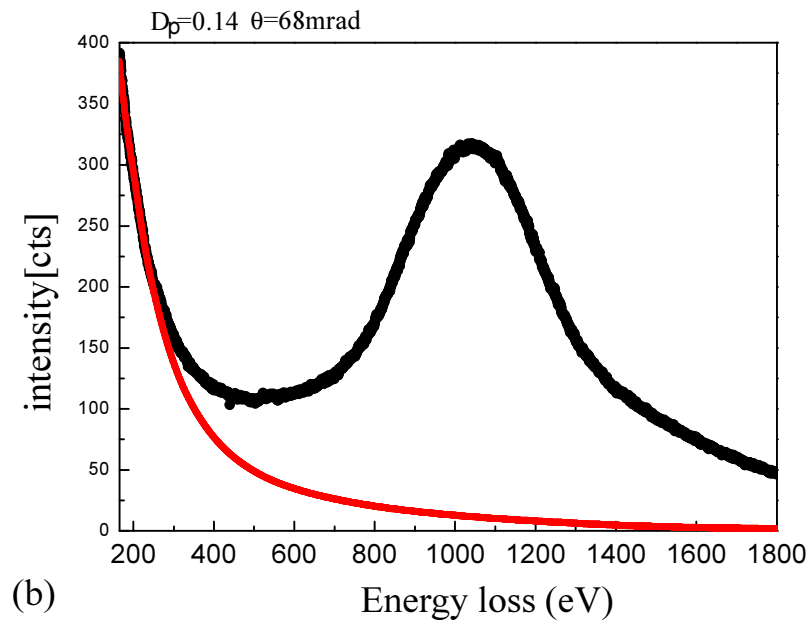
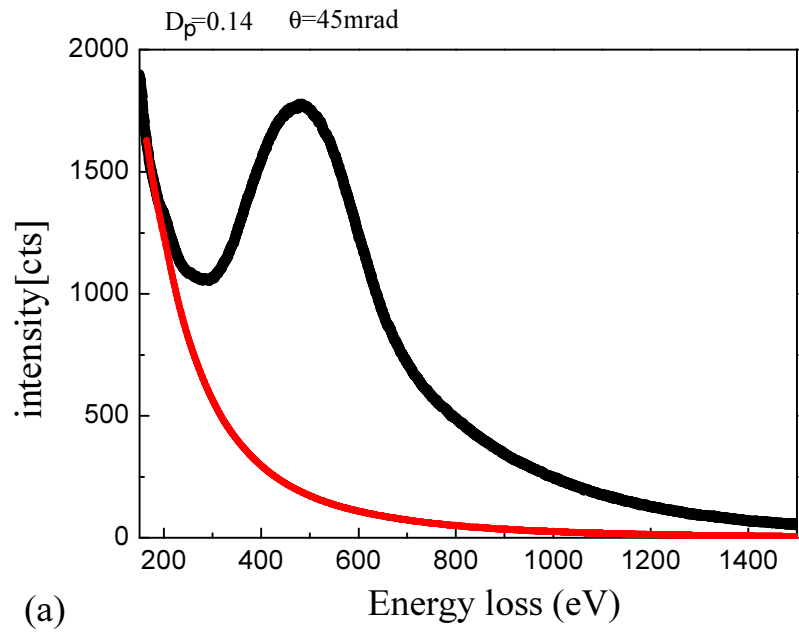


Figure 3.10 The recording ECOSS data of silicon (black) per second for the thickness of $D_p=0.14$ at scattering angles (a) 45 mrad and (b) 68 mrad. The red line is the simulated elastic background. The free parameter θ_0 was set to 30 mrad for background calculations.

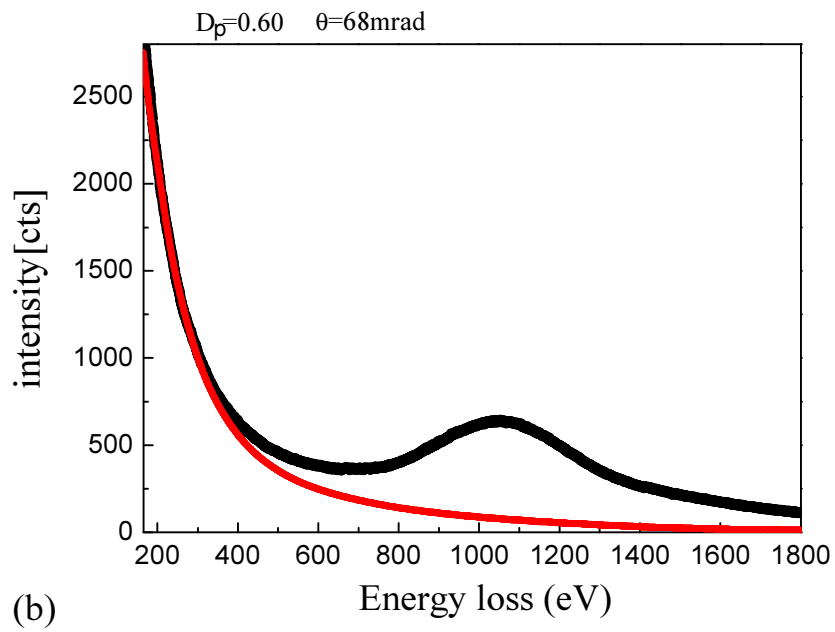
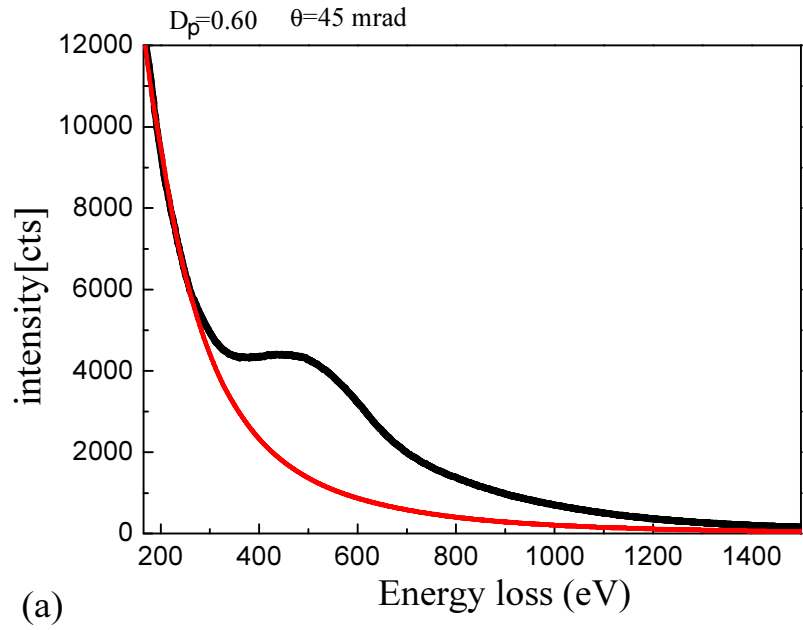


Figure 3.11 The recording ECOSS data of silicon (black) per second for the thickness of $D_p=0.60$ at scattering angles (a) 45 mrad and (b) 68 mrad. The red line is the simulated elastic background. The free parameter θ_0 was set to 30 mrad for background calculations.

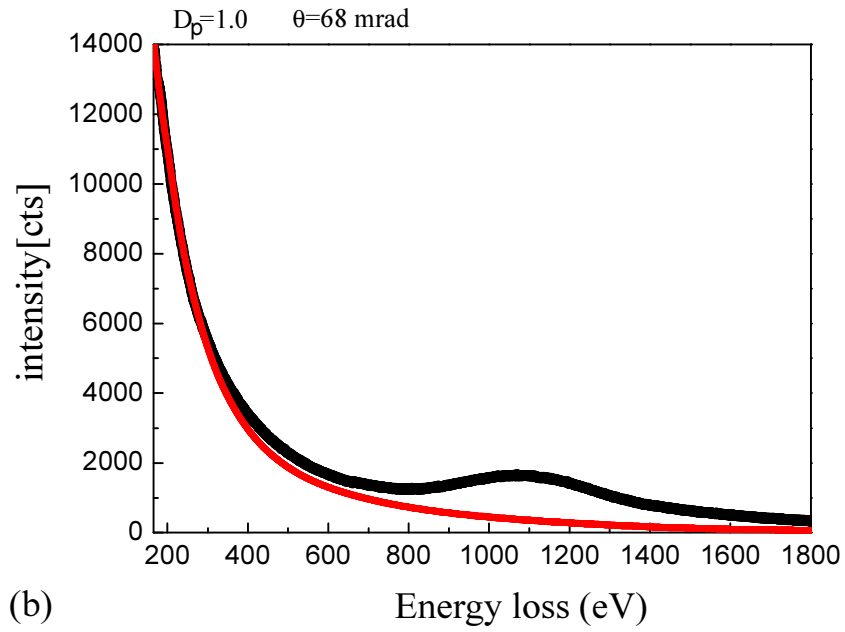
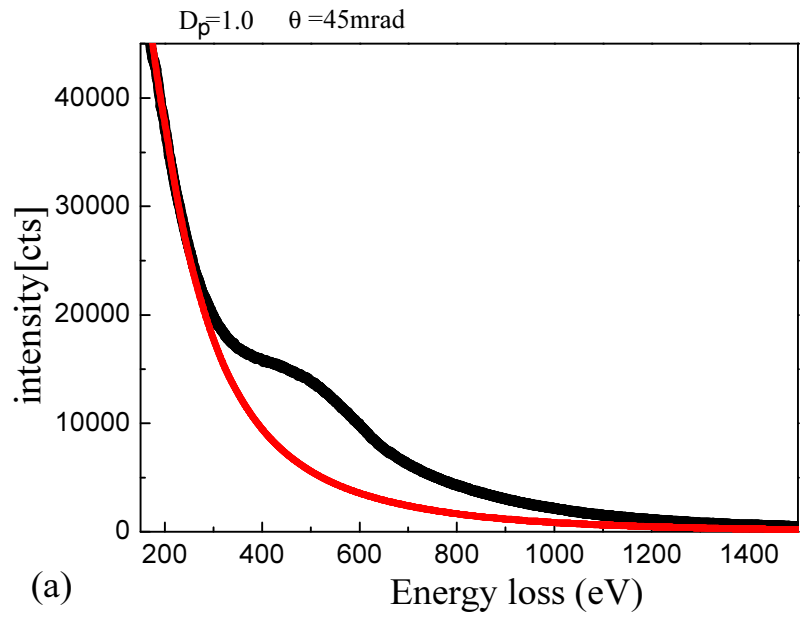


Figure 3.12 The recording ECOSS data of silicon (black) per second for the thickness of $D_p=0.60$ at scattering angles (a) 45 mrad and (b) 68 mrad. The red line is the simulated elastic background. The free parameter θ_0 was set to 30 mrad for background calculations.

obtained by taking the inverse Fourier transform of Eq. (3.7). $P_{i,e}$ can be regarded as “elastic background” in the Compton scattering region [34, 35].

A systematic overview of the scattering angle and thickness dependence of ECOSS of silicon is shown in Fig. 3.10-3.12. The background was calculated in the following procedure. The single scattering function $f(E, \theta)$ in the Eq. 3.7b is expressed by means of the double differential scattering cross section (DDSCS) $d^2\sigma/dE d\Omega$. The DDSCS for plasmon scattering in a free-electron gas model can be approximated as [33]

$$\frac{d^2\sigma_p}{d\Omega dE} \propto \frac{E(\Delta E_p) E_p^2}{(E^2 - E_p^2)^2 + (E\Delta E_p)^2} \left(\frac{1}{\theta^2 + \theta_E^2} \right) \quad (3.12)$$

where E_p is known as the plasmon energy and ΔE_p is the plasmon linewidth. For silicon, the plasmon energy was measured to be $E_p = 16.9 \text{ eV}$, the plasmon linewidth $\Delta E_p = 4 \text{ eV}$ and the characteristic scattering angle $\theta_E = 4.25 \times 10^{-5} \text{ rad}$ for 200 keV electrons.

A Lenz distribution was used for the quasi-elastic single scattering cross section which can be approximated as [33]

$$\frac{d\sigma}{d\Omega} \propto \frac{1}{(\theta^2 + \theta_0^2)^2} \quad (3.13)$$

The characteristic angle θ_0 is a free parameter in the simulation.

The energy and angular dependence of the scattering cross sections for transitions from inner shells (2s and 2p) or outer shells (3s and 3p) to continuum states were calculated by Hartree-Slater method. These calculations consider $l' = 0-11$ for core electrons transitions and $l' = 0-19$ for valence transitions. The total cross sections were calculated in the energy loss region between 165 and 2000 eV at momentum transfers from 0 to 15 a.u. in steps of 0.25 a.u.. The contributions from K-shell were not calculated due to the energy-loss of the Compton peak below 1839 eV (K-edge of Si). The cross sections of the different scattering events are matched to each other by the following ratios [57]:

$$\frac{\sigma_p}{\sigma_c} = x, \quad \frac{\sigma_e}{\sigma_p + \sigma_c} = C. \quad (3.14)$$

where σ_p , σ_c and σ_e are cross sections of plasmon, core electrons (L-shell for silicon in our experiments) and elastic scattering, respectively. In the case of silicon, the ratio $x = 5.5$, $C = Z/20$ (the atomic number $Z=14$ for silicon) [54]. Noting that $\lambda_i/\lambda_j = \sigma_j/\sigma_i$, the parameter D in Eq. (3.10) can be obtained for the different scattering events.

The free parameter θ_0 has a strong influence on the shape of the simulated elastic background, as shown in Fig. 13. This behavior can be explained in the following way. For the large θ_0 , the background distribution is dominated by the large angle elastic scattering followed by one or more small angle inelastic scattering events; this results in a smooth, monotonic decreasing function of energy loss. As θ_0

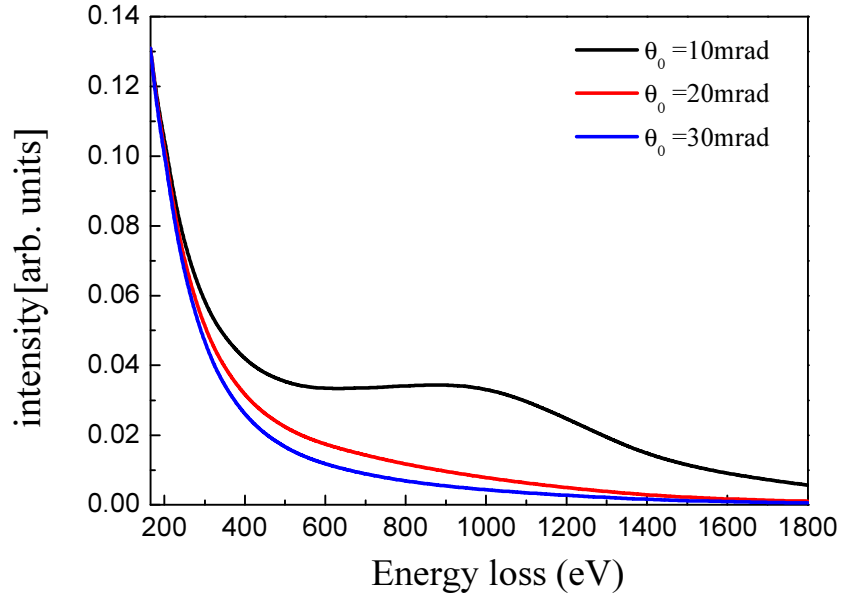


Figure 3.13. The simulated elastic background $P_{i,e}$ at $\theta_0 = 10, 20$ and 30 mrad.

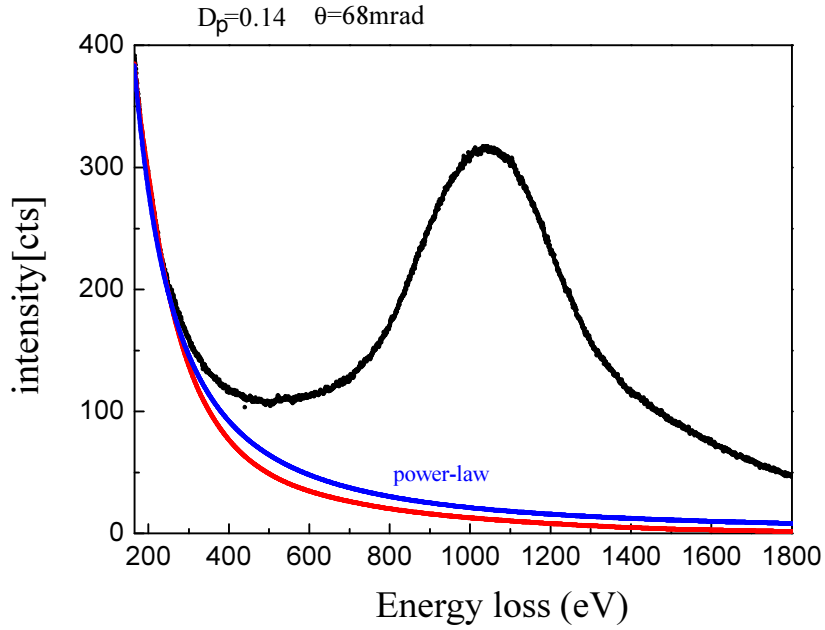


Figure 3.14. Experimental ECOSS data (black line) of silicon at scattering angle 68 mrad for thickness $D_p = 0.14$ along with a simulated elastic background (red line) and a fitted background of a power-law type (blue line). The free parameter θ_0 was set to 20 mrad for elastic background calculations; $r \approx 1.61$ for power-law type background.

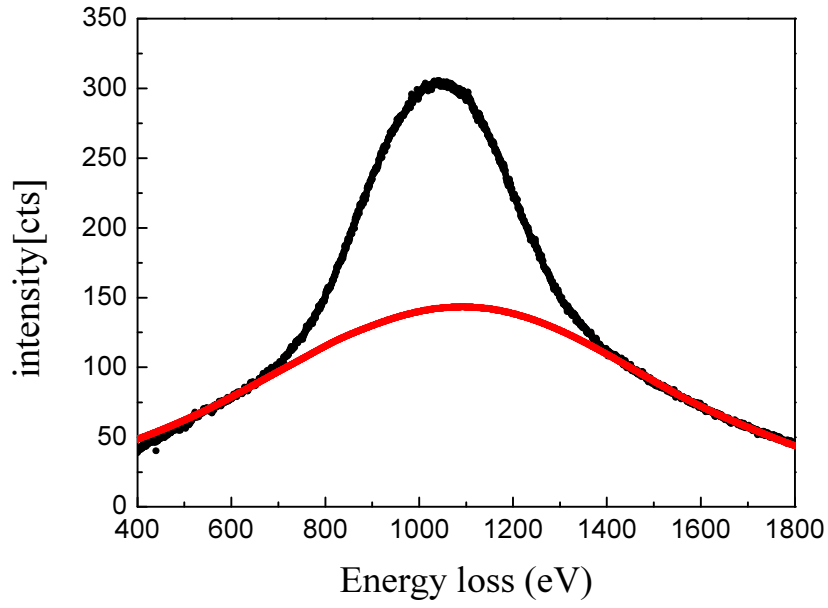


Figure 3.15. Measured ECOSS data of silicon after a simulated elastic background subtraction at scattering angle 68 mrad for thickness $D_p = 0.14$. The red line is contributions of core electrons which was calculated by Hartree-Slater method.

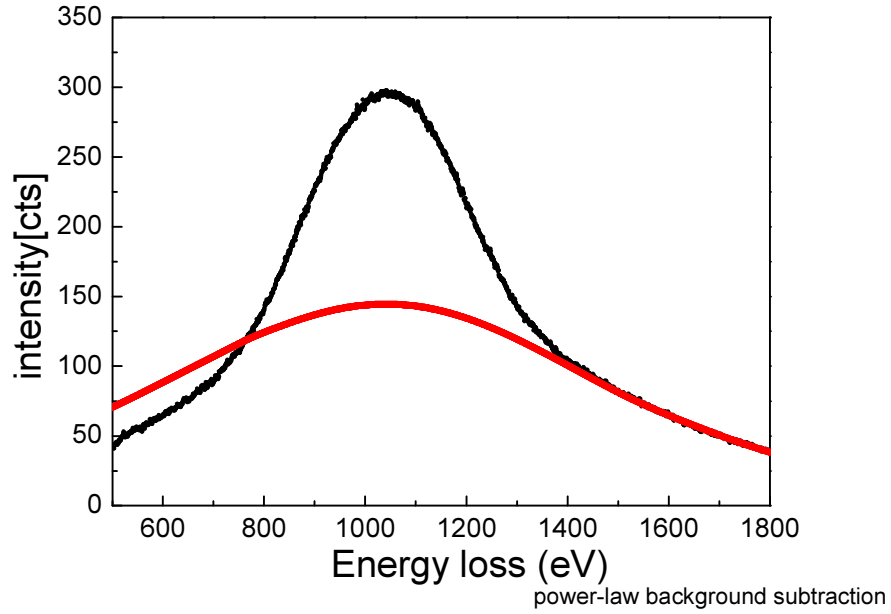


Figure 3.16. Measured ECOSS data of silicon after a power-law type background subtraction at scattering angle 68 mrad for thickness $D_p = 0.14$. The red line is contributions of core electrons which was calculated by Hartree-Slater method.

decreases, the increasing weight of large angle inelastic scattering events results in a Compton-like peak in the background. The parameter C can't alter the shape of the elastic background, but it has a strong influence on the ratio of the signal to background in the Compton scattering simulation [34].

It is obvious that the specimen should be as thin as possible to get the maximized signal/background ratio at the Compton peak, just as the conventional EELS experiment. Fig. 3.14 compares the simulated elastic background with the best fit power-law type background to the total ECOSS. Experimental data are plotted in Fig. 3.15 and 3.16 after a simulated elastic background and a power-law type background subtraction, respectively. We also calculated the contributions of core electrons by Hartree-Slater method. We see that the agreement is good at the tails of total spectrum for a elastic background subtraction in Fig. 3.15. We observed that the power-law type function overestimate background from both Fig. 3.14 and Fig. 3.16.

Chapter 4

Application on Solids

In this Chapter we shall focus on experimental results by means of electron energy-loss spectroscopy in the Compton scattering region. Electron Compton profiles of silicon (cubic), graphite (hexagonal) and amorphous carbon (structureless) were obtained in the TEM. Much short recording time makes it possible to study the momentum dependence of the Compton profile from solids. A much better intensity and signal-to-noise ratio give us an opportunity to study the momentum transfer dependence and anisotropy of ECOSS from the crystal specimens. The valence Compton profiles were got after core Compton spectra subtraction by a Hartree-Slater wave functions calculation. The results were compared with profiles using photon Compton scattering.

4.1 Silicon

The crystal silicon is the most common sample for the TEM. It is easy to prepare for the microscope and quite inert to radiation damage by the incident electron beam. The electron Compton profile of silicon has already been obtained using the TEM in 1993 [34]. At the time, it would take more than 10 mins to get one available Compton profile of silicon. Parallel-recording spectrometer reduces the exposure time for measuring Compton scattering spectra from hours to minutes, but this is still a rather long time for a microscopist. On the modern electron microscopes, one can get an electron Compton profile from solid in the TEM in tens of seconds which is much shorter than several hundred seconds required 20 years ago. The contribution of core electrons in the total ECOSS is also subtracted by Hartree-Slater method.

4.1.1 Experimental details

The silicon flake was prepared by mechanical polishing up to the level of 20 microns using an ESC 300 GTL polishing machine. We then glued the flake to a copper grid and milled it using the precision ion polishing system (PIPS) until a small hole appeared in the sample, with incident energy of 4 kV and at an incident angle of $\pm 6^\circ$. A region around the hole in the sample with the thickness of 25 nm was chosen in this study. The measurements were performed in diffraction mode on a FEI TECNAI F20 microscope equipped with a GIF Tridiem with 200 kV acceleration voltage. The convergence semi-angle is 3.5 mrad and the collection angle is 1.2 mrad for the ECOSS measurements. All the spectra were acquired in the sharp Bragg spots plane by adjusting the diffraction focus.

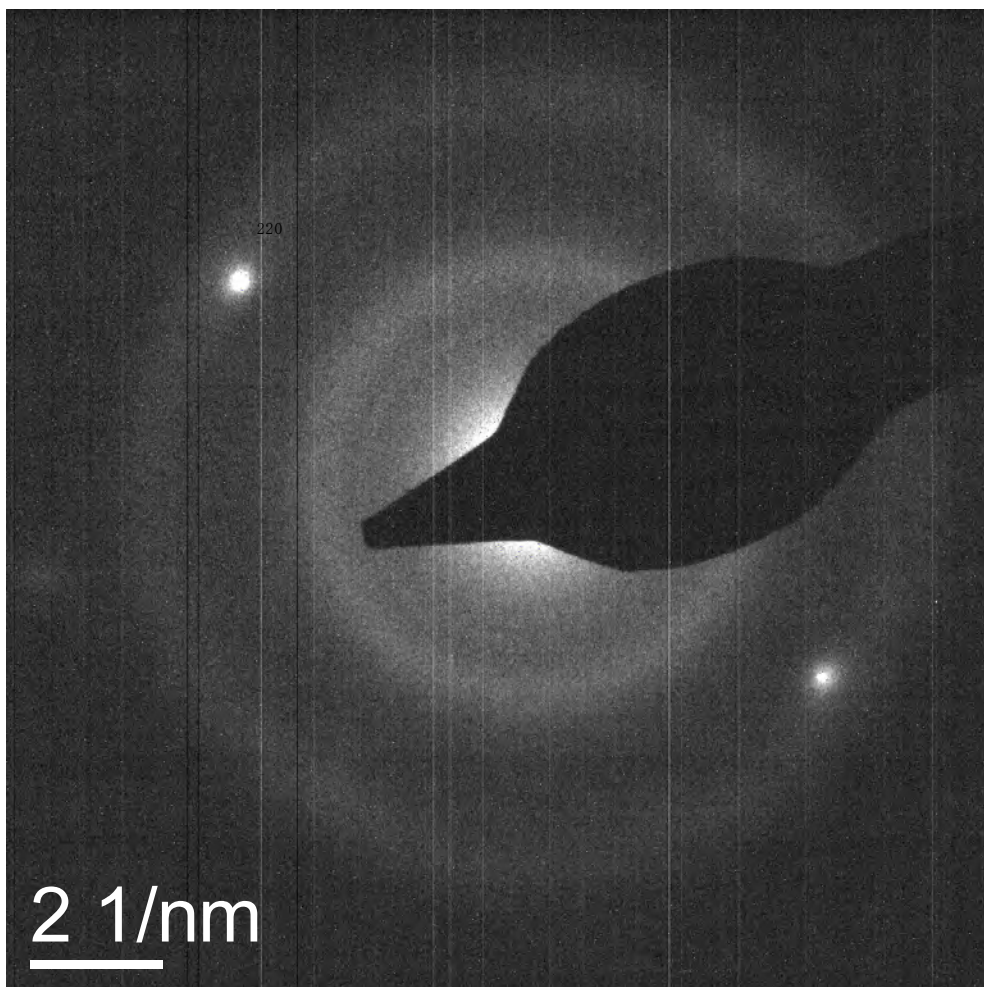


Figure 4.1 The diffraction pattern of the three-beam case from silicon.

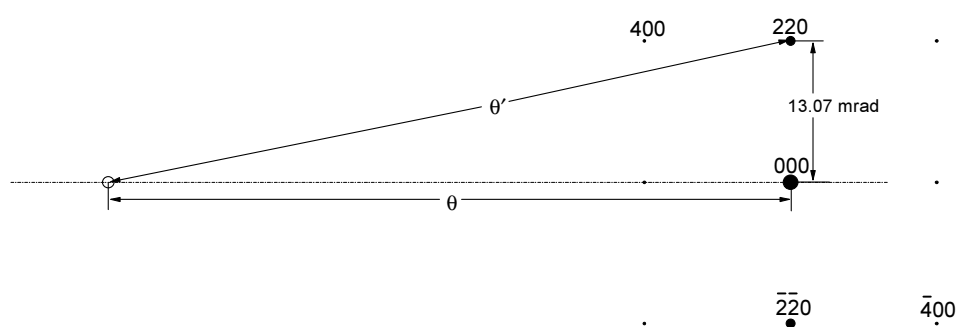


Figure 4.2 Symmetric 3-beam scattering geometry for measurements

Using single crystals to carry out ECOSS experiment, it is important to choose a proper scattering geometry. The reason is that strong contributions from diffracted beams (Bragg beams) may overlap the directly scattered Compton distribution and alter the Compton lineshape dramatically. Each diffracted beam can be regarded as a source of Compton scattering [58]. It's impossible to get an available result for a single crystal sample in a zone axis orientation. Because the scattering cross section of electron inelastic scattering decreases as the fourth power of the scattering angle. So the goal is to attenuate the contributions from diffracted beams by reducing the intensity of diffracted beams which lying between the detector and the directed beam. This can be achieved by tilting the sample away from the zone-axis to get a systematic row condition of the diffraction pattern (three-beam case), as shown in Fig. 4.1. Then, the diffraction pattern was shifted perpendicular to the systematic row with respect to the GIF detector to record EELS at chosen scattering angles as represented schematically in Fig. 4.2. A systematic row including (220) diffraction spot for silicon, when $\theta = 65 \text{ mrad}$, the scattering angle of Compton scattering from (220) diffraction spot is $\theta' \approx 66 \text{ mrad}$. The measured ECOSS data at scattering angles $\theta = 65 \text{ mrad}$ and 66 mrad are shown in Fig. 4.3. We conclude that the contributions from diffracted spot (220) are more strongly at the low energy-loss side (between zero-loss peak and the Compton scattering regime) than the high energy-loss side of the Compton lineshape. In addition, the intensity of diffracted spots is much weaker than the direct beam and cross section of inelastic electron scattering decreases as the fourth power of the scattering angle [40]. So the contributions from diffracted beams for this three-beam case alter the Compton profile very finitely in the higher energy-loss side.

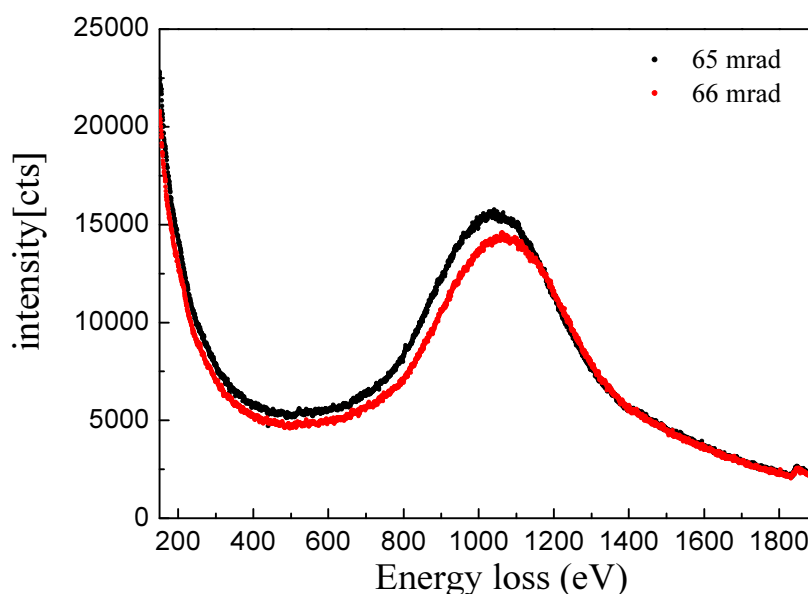


Figure 4.3. Measured electron Compton scattering spectra of silicon at scattering angle 65 mrad (black) and at scattering 66 mrad (red).

4.1.2 Results

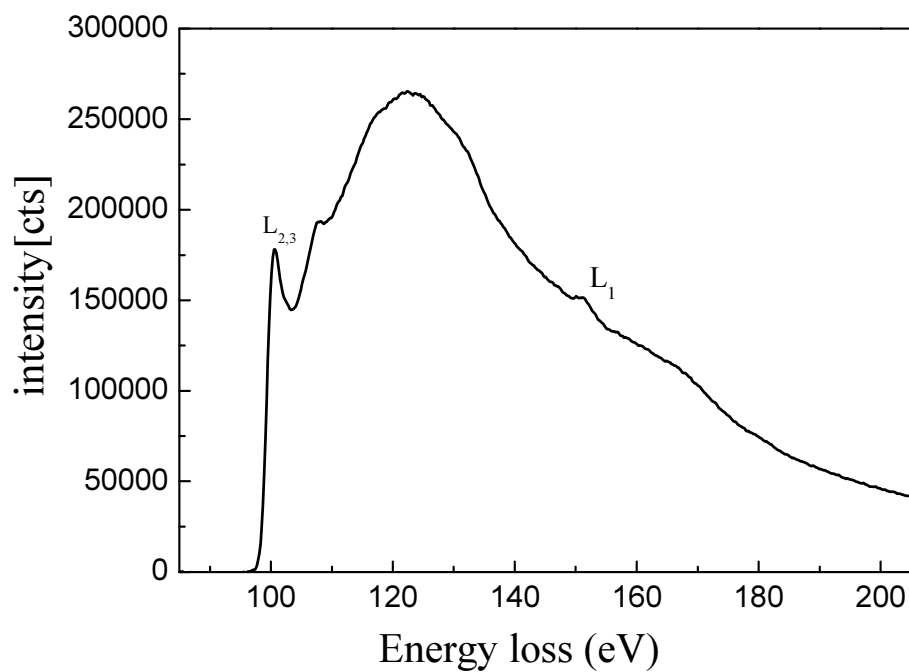


Figure 4.4 The ELNES of the silicon-L edge recorded in the forward direction.

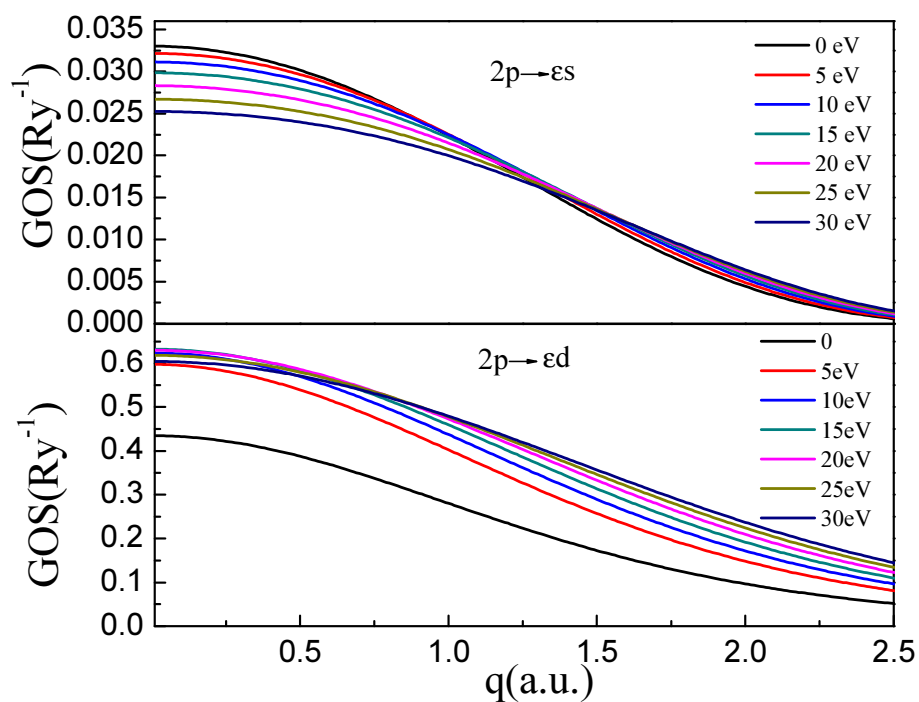


Figure 4.5 The GOS for 2p dipole transitions of the silicon at a series of continuum energies. Calculations were performed by Hartree-Slater method.

Fig. 4.4 shows ELNES of silicon-L edge at the collection angle 0.3 mrad in the forward direction. The $L_{2,3}$ edge corresponds mainly to the transitions from the ground $2p$ states to the unoccupied ϵs states[44, 59]. The delayed maximum arises from d -like final states. The GOS of silicon for the dipole transitions $2p \rightarrow \epsilon s$ and $2p \rightarrow \epsilon d$ at a series continuum energies are shown in Fig. 4.5. The values of the GOS at $q=0$ for the transitions $2p \rightarrow \epsilon s$ decrease monotonously with increase energy loss. This results in a sharp peak at energy loss around 100 eV in Fig. 4.4. The GOS at $q=0$ for the transitions $2p \rightarrow \epsilon d$ rises till $\epsilon=15\text{ eV}$, it exhibits a delayed maximum in ELNES.

Electron energy-loss spectra of silicon have been recorded for 9 scattering angles in the range from 35 mrad to 64 mrad (momentum transfers $4.5\text{ a.u.} \leq q \leq 8.5\text{ a.u.}$) as shown in Fig. 4.6. Those spectra are original data from the TEM and corresponding exposure time is from 10s to 60s. The electron Compton peak shifts to higher energy loss with increasing scattering angle. The large scattering angle means the large momentum transfer results in higher energy loss. The Bethe surface of silicon can be obtained in experiment if one transfers those spectra to the generalized oscillator strengths (GOS) by means of Eq. (2.39). The Compton lineshape is broadened, reflecting the fact that the scatterer (the electron of silicon in the ground state) is not rest. The Compton lineshapes become more and more symmetry and obvious with the Compton peaks away from the ionization edge. In order to obtain useful Compton profile in the TEM, it requires the Compton peak far away from any ionization edge in ECOSS experiment.

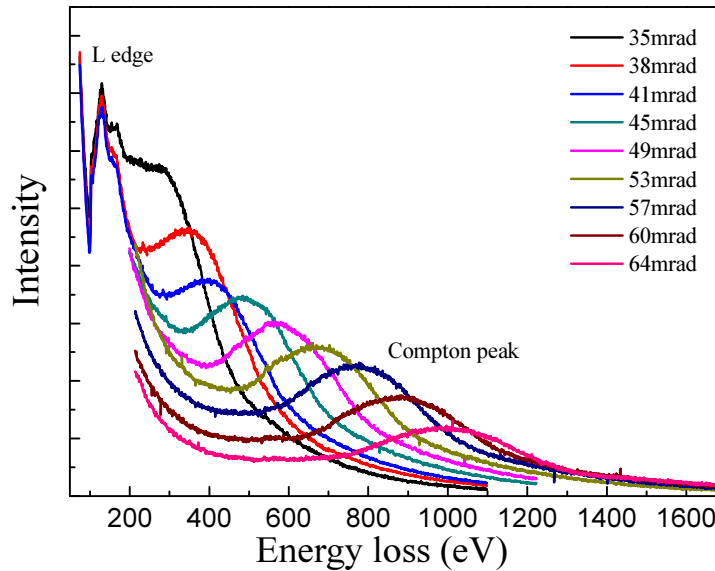


Figure 4.6 The recorded EELS of silicon in the TEM at a series of scattering angles from 35 mrad to 64mras. The exposure time is 10s to 60 s. The thickness of silicon is 22 nm.

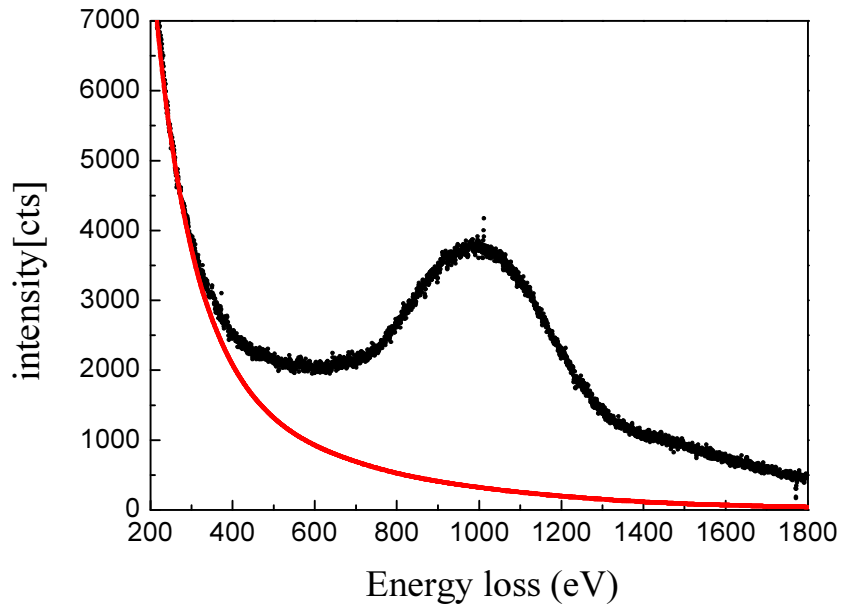


Figure 4.7 The recorded ECOSS (dark dots) of silicon at a momentum transfer $q=8.5$ a.u. along with our simulated background (the red line).

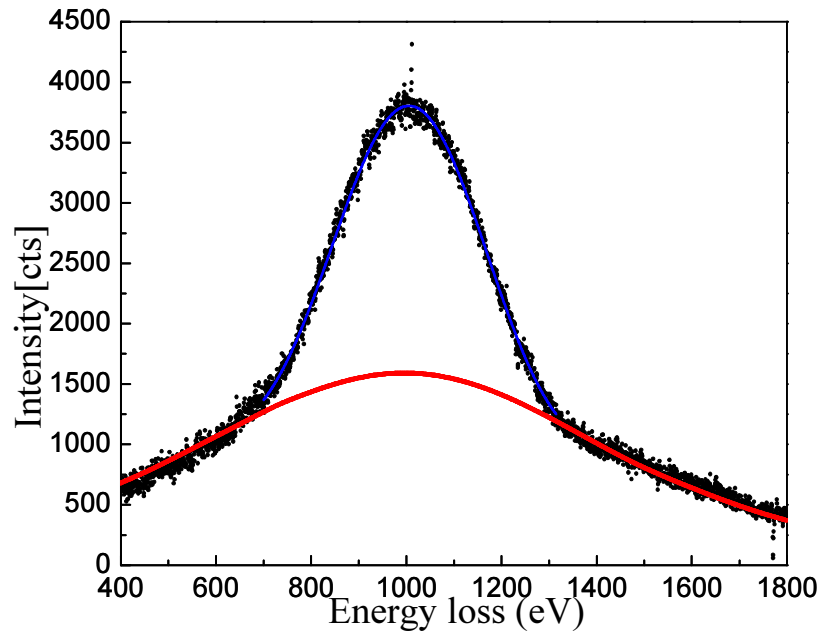


Figure 4.8 The ECOSS (dark dots) of silicon after background subtraction at a momentum transfer $q=8.5$ a.u.. The contributions from core electrons ($2s^2$ and $2p^6$ of silicon) were calculated by the Hartree-Slater method (red line). The precise energy loss of the Compton peak was decided by fitting a parabola (blue line).

The background subtraction is a critical step in any spectroscopy analysis. Usually, a power-law type background is removed in the near edge structure of the EELS. For the ECOSS, the power-law type background won't work due to the Compton lineshape extends several hundreds eV. The problem was solved by using parameterized simulation of combined inelastic and elastic events in 1992 [35]. Fig. 4.7 shows the measured electron Compton spectrum at the scattering angle 64 mrad (momentum transfer $q=8.5$ a.u.) along with the simulated elastic background. The exposure time is 60s which is much shorter than 900s required 20 years ago [34].

Since we focused on the valence Compton profile, the contribution from core electrons ($2s^2 2p^6$ for silicon) has to be subtracted first in theory. The behavior of core electrons changes very little in the procedure of the free atoms form solid. So that a Hartree-Slater free atom calculation for core electrons should be suffice to determine their contribution to the total Compton profile of the solid. The electron Compton spectrum after background subtraction for the momentum transfer $q=8.5$ a.u. together with our calculated contributions from core electrons by the Hartree-Slater method are shown in Fig. 4.8. The core Compton spectrum was determined by fitting the theoretical core spectrum for the momentum transfer $q=8.5$ a.u. at the tail region (1400eV-1800eV) of the experimental spectrum. The agreement of the theoretical core contributions at the wings of the experimental spectrum is very well. This agreement also indicates that the correctness of our background subtraction and Hartree-Slater model for the Compton scattering calculation.

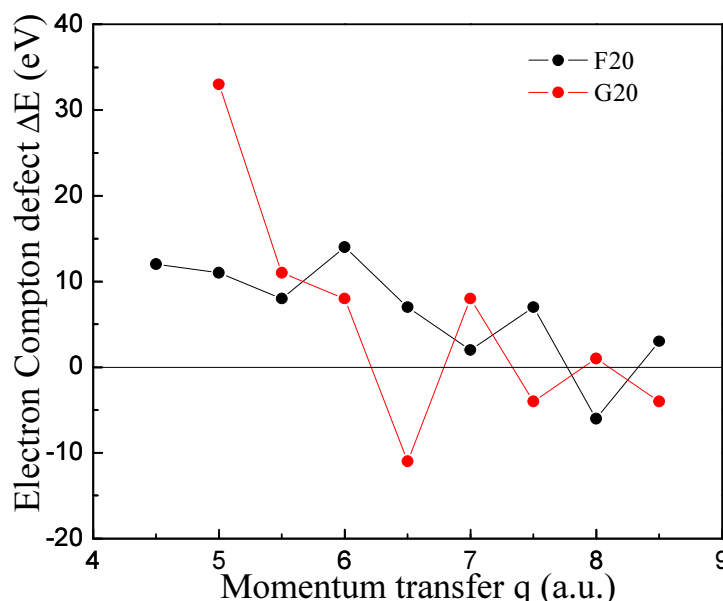


Figure 4.9 The momentum transfer dependence of the electron Compton defect of silicon in our ECOSS experiments. F20 represents the experiment was carried on field emission microscope (FEI TECNAI F20), G20 represents the results come from the filament emission microscope (FEI TECNAI G20).

The energy loss of the Compton peak was determined by fitting a parabola to the valence Compton lineshape as shown the blue line in Fig. 4.8. The energy loss of

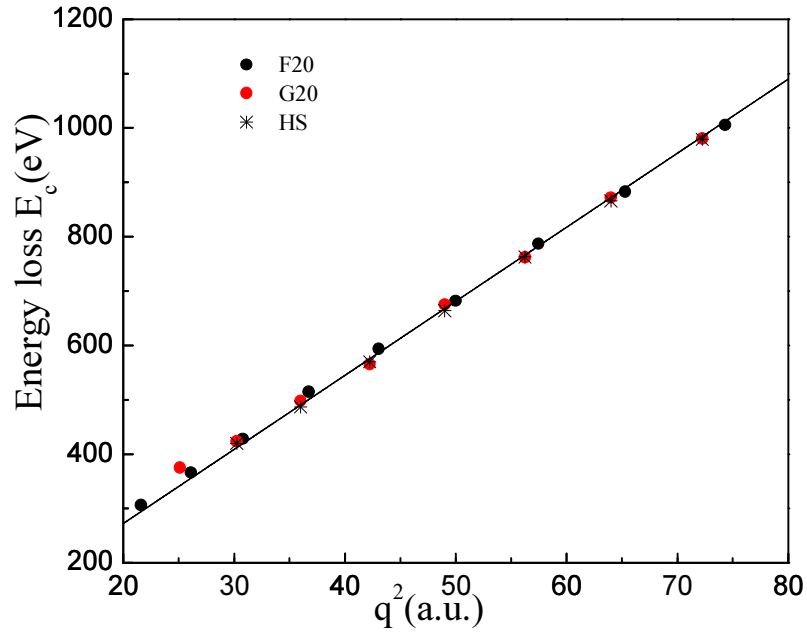


Figure 4.10 The energy loss of electron Compton peaks with respect the square of the momentum transfers. F20 and G20 represent the same thing in Figure 4.9, HS represents the results obtained from our Hartree-Slater calculations. The line comes from free electron model $E = q^2 / 2m_e$.

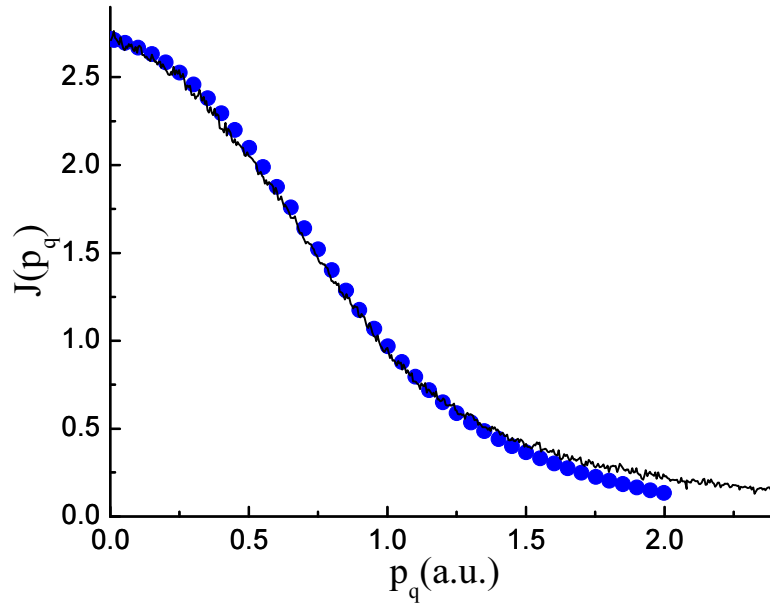


Figure 4.11 Experimental valence electron Compton profile of Si in the TEM (black solid line) compared to the data from X-ray (blue dots) [60]. The data of X-ray has been broadened by a Lorentzian.

the Compton peak can be obtained by using Eq. (2.25) in the impulse approximation (IA). The shift of the Compton peak can be expressed by the quantity $\Delta E = E_{obs} - E_{IA}$, E_{obs} is the energy loss at the Compton peak in ECOSS and E_{IA} is the energy loss predicted by using Eq. (2.25). This difference is known as the Compton defect. The momentum transfer dependence of the Compton defect of silicon in our experiment is shown in Fig. 4.9. The large Compton defect at small momentum transfers may be due to the effect of the ionization edge (L edge of silicon). The energy loss of the Compton peaks with respect to the square of the momentum transfers is plotted in Fig. 4.10. The position of the Compton peak in ECOSS lies almost exactly on the free electron parabola both in electron Compton scattering experiment and the Hartree-Slater calculation.

The valence electron Compton spectrum was transformed to GOS by means of Eq. (2.39). Then, the GOS was normalized to the number of electrons in outer shells ($3s^2 3p^2$), according to the Bethe sum rule [61]. Finally, the absolute GOS was converted to a Compton profile by means of Eqs (2.40 and 2.41) within the binary encounter approximation [28, 30]. The data of the valence electron Compton profile at the scattering angle 64 mrad was plotted in Fig. 4.11, where they were compared with the most recent results of X-ray [62]. The data of X-ray have been convoluted with the resolution function in our experiment. The data from ECOSS are in reasonably good agreement with X-ray data.

4.2 Graphite

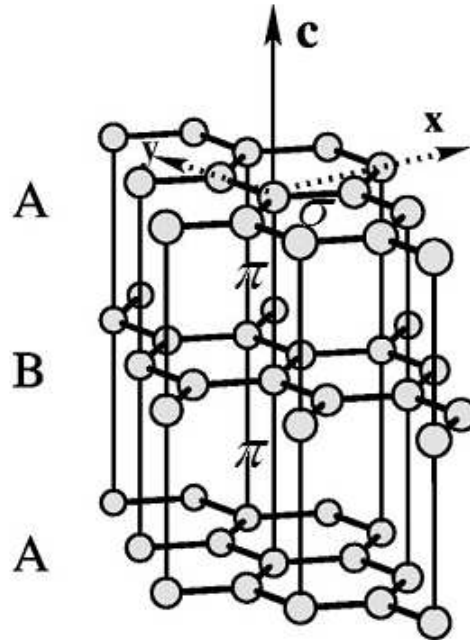


Figure 4.12 The structure of graphite. ABA stacking of hexagonal planes of carbon. σ and π orbitals are also shown. The Figure adapted from Marinopoulos [63].

Graphite has long been interest as a prototypical two-dimensional anisotropic material (see Fig. 4.12) with very strong sp^2 covalent in the basal plane and weak van der Waals interlayer bond. This two-dimensional nature of graphite results in a strong directionality of the bonds: σ (sp^2 orbitals) bonds lie within the basal plane, while π (p_z orbitals) bonds are directed perpendicular to the basal plane [64]. The separation of unoccupied states into π^* and σ^* bands has been verified with many techniques over the years [64, 65]. Peaks in the ELNES of graphite are very sensitive to the magnitude and the direction of the momentum transfer [66]. We further explore the nature of the C-C bonding of graphite by measuring electron Compton scattering profiles at large momentum transfers. Until now, to our knowledge, no combined study of the ground and unoccupied electronic states of graphite has been performed to examine the dependence of the cross sections on the momentum transfer. In addition, knowledge of the electronic properties of graphite is a beginning point for understanding carbon materials (graphene [67], carbon nanotube [68], intercalated graphite [69] etc.), which is an active research field.

In this thesis, both the unoccupied and ground electronic states of graphite have been studied by electron energy-loss spectroscopy in a transmission electron microscope. Electron energy-loss near-edge structures (ELNES) of the K-edge of carbon have been investigated in detail for scattering angles from 0 to 2.8 mrad. The π^* and σ^* components were separated. Electron energy loss Compton spectra of graphite were recorded at scattering angles from 45 to 68 mrad. One Compton scattering spectrum was obtained in 1 min compared with several hours or days using photons. The contributions of core electrons were calculated by the exact Hartree-Slater method in the Compton scattering region. And the anisotropy of the electron Compton profiles of the graphite in the TEM was first studies in this work. The electron Compton profile for graphite is in good agreement with other conventional Compton profile measurements, as well as with theory, thus establishing the validity of the technique.

4.2.1 TEM sample preparation

Samples of graphite for the TEM were prepared by cleaving with adhesive tape and transferred to the TEM grids using J.C. Meyer's method [70]. The preparation process can be divided into two procedures: mechanical cleavage and sample transfer to the TEM grid.

4.2.1.1 Mechanical cleavage

Graphite layers are bonded by weak van der Waals forces. It is easier to overcome the forces of these interlayers by cleaving the graphite using the scotch tape. This method is known as "scotch tape method".

Materials (see Fig. 4.13): Natural graphite, Scotch tape, Silicon substrate (There is

300 nm thickness of SiO₂ on one surface).

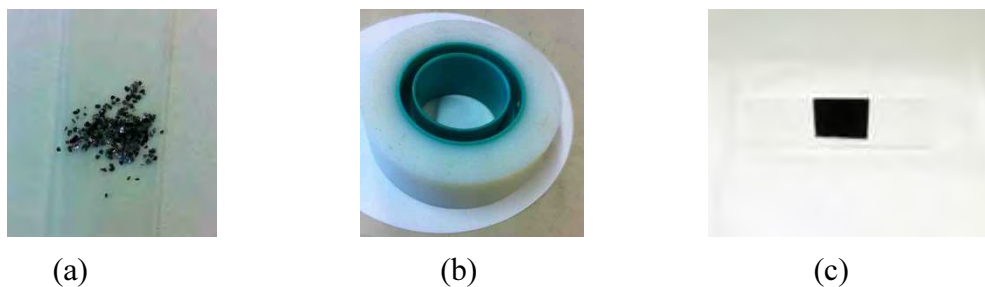


Figure 4.13 Materials of (a) natural graphite (b) scotch tape and (c) SiO₂/Si substrate

Steps:

1. Take a piece of scotch tape about 15-20 cm long and fold over about 1 cm of each end of the tape to make a “handles” for holding the tape.



2. A small amount of natural graphite is poured on the one end of the tape. For the purpose of description, I will refer to this end of the tape as the “*left side*”, while the other end is referred as “*right side*”.



3. Fold the tape in half, the “*right side*” of the tape is folded over the graphite area, sticky sides together, then slowly separated them. Through this first folding, graphite samples are cleaved for the first time.



4. The graphite area is then pressed against the right side by an unused area next to the first cleaved area. Do this several more times until the middle of the tape has reached.



5. Now all graphite samples covered the right side half of the tape. Fold the tape in half over the graphite area, pressed and separated. This process is repeated 3-5 times.



6. Take another piece of scotch tape just like step 1. I will refer the second tape as “tape 2”. Then the tape 2 is placed onto the first one, pressed and separated slowly.



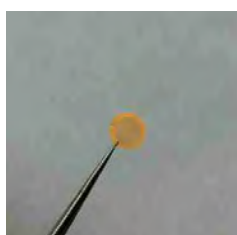
7. The region of tape 2 with thin graphite flakes is selected for being transferred to the substrate. The substrate of SiO_2 surface is placed over the selected flakes. It is pressed gently for about 5 minutes to transfer the graphite/graphene to the SiO_2 surface. The tape is carefully peeled from the substrate. Thin layers of graphite/graphene will leave on the surface of SiO_2 .



4.2.1.2 Graphite transfer to TEM grids.

Materials (see Fig. 4.14):

- We have used quantifoil TEM grids. The quantifoil perforated amorphous carbon film with $1.3\ \mu\text{m}$ (diameter) holes on 200 mesh gold grids.
- Isopropanol $\text{C}_3\text{H}_8\text{O}$, Potassium hydroxide (KOH)



(a)



(b)



(c)

Figure 4.14 (a) Quantifoil TEM grids : Au 200 mesh, (b) Isopropanol $\text{C}_3\text{H}_8\text{O}$, (c) Potassium hydroxide (KOH)

Steps:

1. With an optical microscope, one can identify the thin graphite or graphene flakes as selected area to transfer to TEM grids on surface of the substrate, see Fig.4.15.
2. The quantifoil TEM grids is placed onto the selected flake, being aware that the selected piece must match one of the holes in the amorphous carbon film and it is must near to the center of the quantifoil grid.
3. A small drop of isopropanol is added on the quantifoil grid cautiously and left to

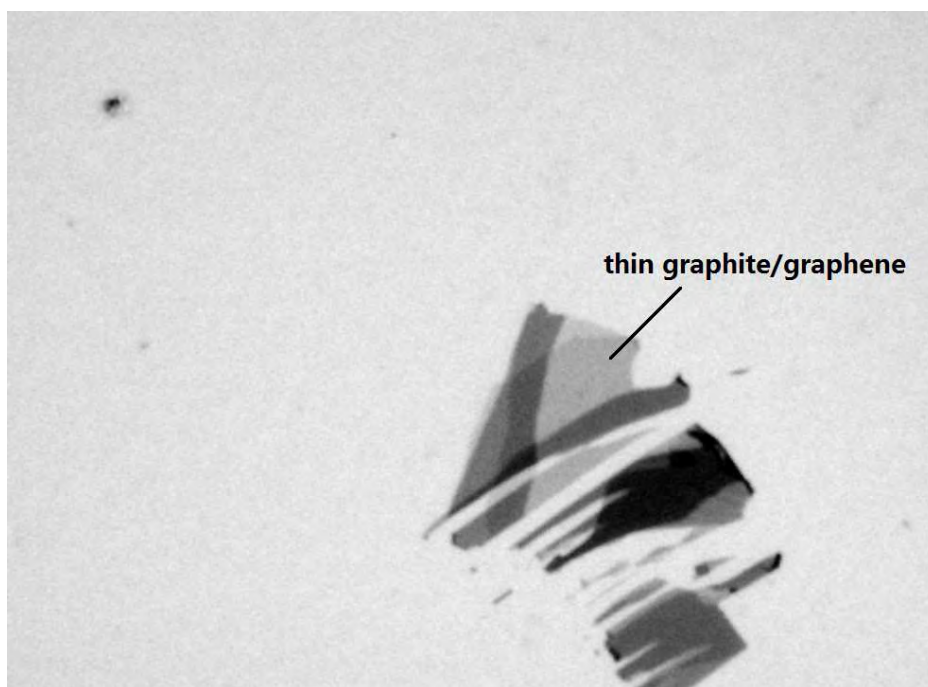


Figure 4.15 Thin graphite on the SiO₂ surface of the substrate in the optical microscope

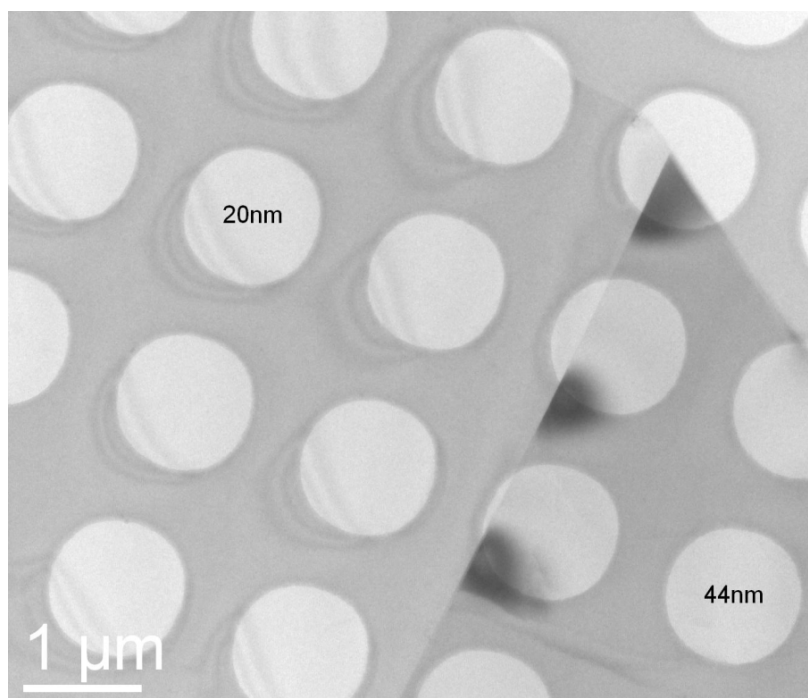


Figure 4.16 The graphite sample in the TEM. 20nm and 44nm is the thickness of the sample.

evaporate. As it evaporates, the surface tension pulls the carbon film into contact to the substrate and the selected graphite sample.

4. The substrate with the quantifoil is then heated at 200 °C for 3 min to improve the adhesion and left to cool.
5. Again the substrate is placed under the optical microscope. Drops of isopropanol and potassium hydroxide are dripped on the bare SiO₂ surface which is near to the quantifoil. The liquids spread into the space between the grid and the substrate. This process will transfer the graphite/graphene from the substrate to grid.
6. Finally, the grid is carefully dried in air.

Fig. 4.16 shows large, uniform and thin graphite samples can be found on the TEM grid in the transmission electron microscope.

4.2.2 Experimental details

Specimen thickness

In order to minimize the multiple scattering and so enhance the visibility of the features corresponding to single transitions, a thin (approximately 20 nm) area of graphite was chosen for the experiment.

Beam energy

It is probably best to use the highest incident energy, unless doing this results in the radiation damage [52]. The EELS (ELNES and ECOS) of graphite were recorded at 60, 120 and 200kV, as shown in Figs. 4.17 and 4.18. The ELNES of graphite don't have substantial changes in the long time for the incident energy 60 and 120 kV. This indicates that the structure of sample is undamaged. It is true that the graphite can be safely studied at tensions below the threshold voltage for the displacement damage, which is 130 kV for graphite. However, the ECOS signals are too low. We find the ELNES of graphite don't have obvious changes in 20 mins for the incident energy 200 kV, while one available ECOS can be obtained in 1 min in this case. To get low noise, stable and smooth signal of ECOS, We chose the 200 kV incident beam energy in this thesis. An extraction voltage of 4.25 kV for the operation of the electron gun was used in our experiments.

Convergence angle

The convergent beam mode was chosen to ensure consistency in the results at large scattering angles. The convergence semi-angle was about 3.5 mrad, resulting a beam diameter in the range 700~800 nm. By spreading the dose over this large area, radiation damage is not expected to be significant even though the electron energy is well above the knock-on threshold [71]. All the spectra were collected in the sharp Bragg spots plane by adjusting the diffraction focus.

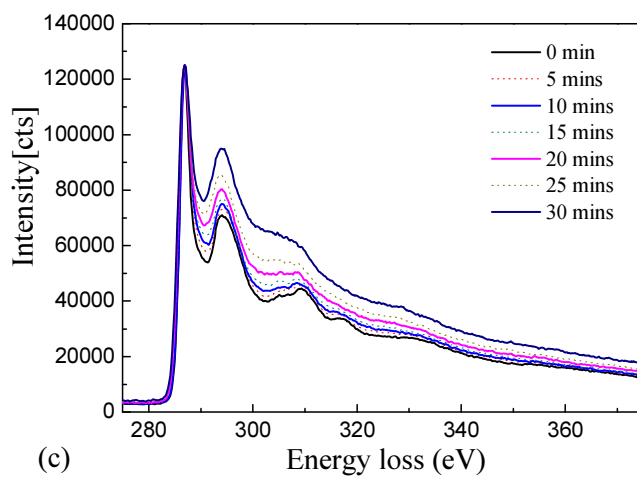
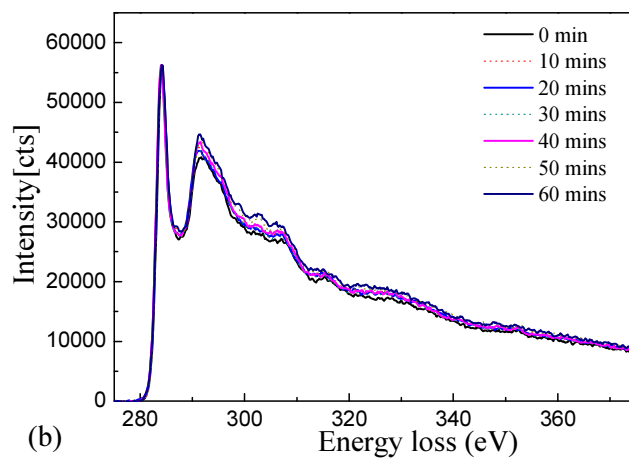
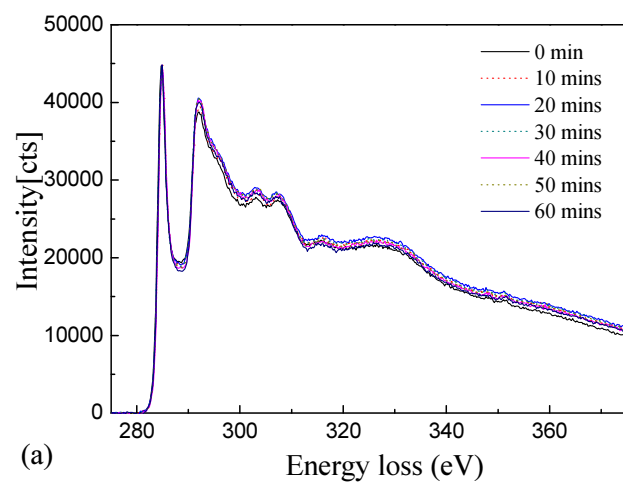


Figure 4.17 The carbon K-edge ELNES of the graphite with the irradiation time at the incident energy (a)60 kV, (b) 120 kV and 200 kV. Some of the data have been normalized so that the intensity of peaks at 284.5 eV are the same.

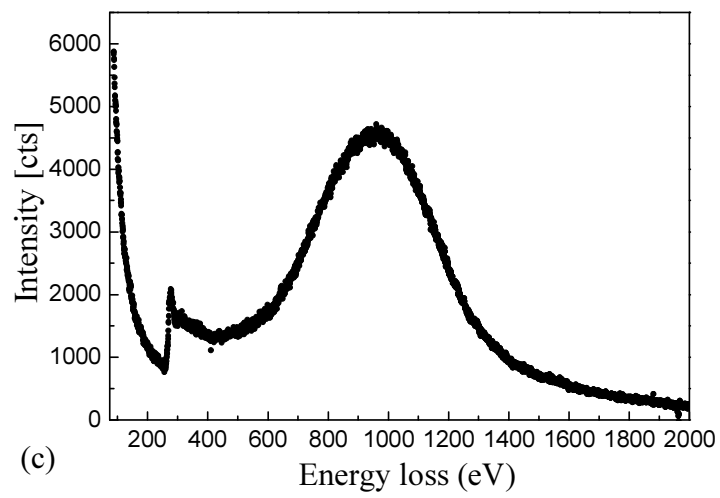
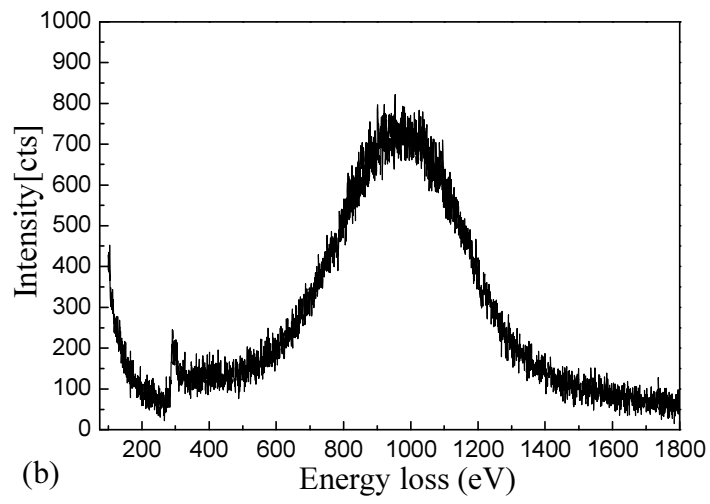
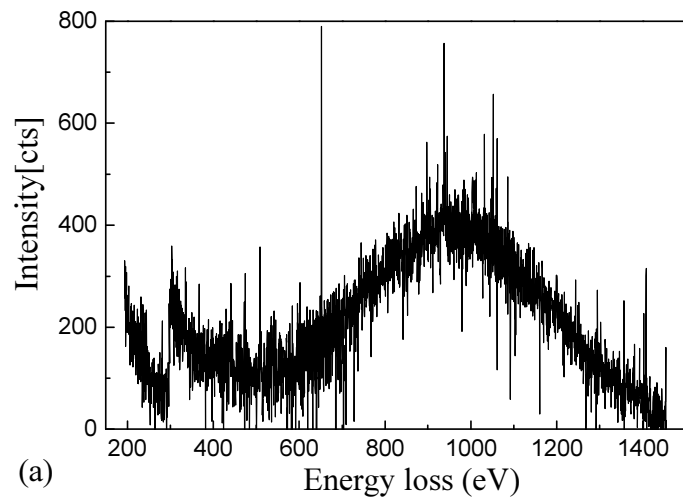


Figure 4.18 The best ECOSS signal at the incident energy (a)60 kV, (b)120 kV and (c) 200 kV.

Collection angle

For ELNES acquisition, the spectrometer entrance aperture was set to 1mm. The camera length was 970 mm. The collection semi-angle was 0.3 mrad. Spectra were acquired at 0.2 eV per channel and the exposure time was 1~20s. The energy resolution (measured as the full width at half maximum (FWHM) of the zero loss peak) was typically around 1.2 eV. In the ECOSS acquisition, the spectrometer entrance aperture was set to 2 mm. The spectra were obtained with an energy dispersion of 0.5 eV/channel. The collection semi-angle was 1.2 mrad. In this configuration the energy resolution was approximately 2 eV.

Scattering geometry

The graphite crystal was oriented with the c-axis parallel to the incident electron beam. In order to study the momentum dependence (in the low momentum transfers region) of the ELNES, the spectra were obtained in diffraction mode with the central beam shifted in dark field with respect to the entrance aperture of the spectrometer as shown in Fig. 4.20 (a). Each Bragg scattering beam can be regarded as a new source of scattering. A set of various Compton scattering spectra with different maximum and width will submerge the single Compton scattering profile. This can be avoided by titling the specimen to get a three-beam condition (see Fig. 4.19). The ECOSS were obtained at seven different momentum transfers in the direction perpendicular to the three-beam line as shown in Fig. 4.20 (b).

4.2.3 Data analysis and results

4.2.3.1 ELNES

ELNES of graphite has been investigated by many researchers in terms of anisotropy [66, 72]. In addition to previous work, here we separate the experimental spectra to obtain not only the strength but the entire π^* and σ^* component spectra. The results agree with Leapman *et al.*'s prediction in theory [66]. Fig. 4.21 shows the C-K edge ELNES recorded with the entrance aperture centered on the optic axis ($\theta = 0$) for the parallel and convergent incident beam, respectively. The sharp peak at the edge (284.5eV) stems from excitations to π^* states whereas the broader peak (291.5eV) about 7 eV above the threshold stems from transitions $1s \rightarrow \sigma^*$ [65]. The results are consistent with existing studies [66, 73]. There is no substantial change for the convergent incident beam at our collection conditions.

The momentum transfer dependence of the C-K edge ELNES of graphite is presented in Fig. 4.22 for five scattering angles. In order to get strong intensity we used a convergent beam for recording the spectra at the chosen scattering angles. The most dramatic trend of the ELNES in Fig. 4.22 is the decrease in intensity of the π^*

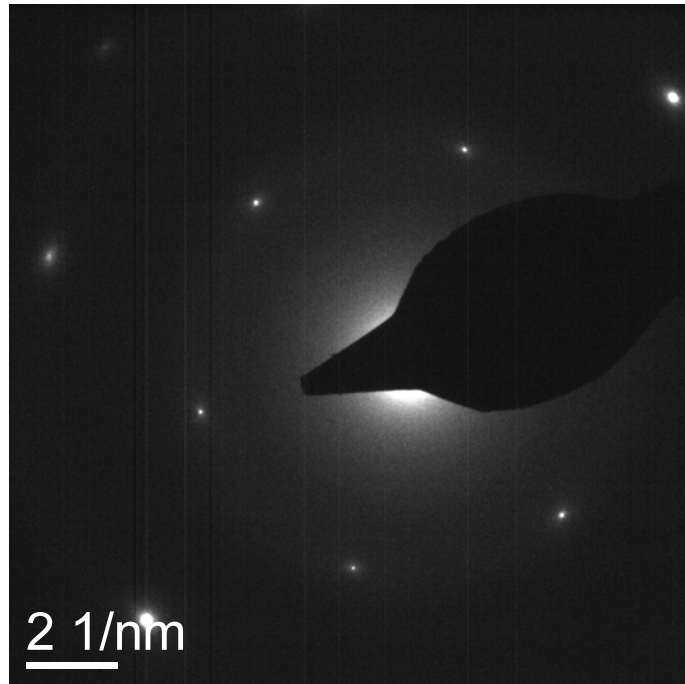


Figure 4.19 The diffraction pattern of three-beam condition from graphite.

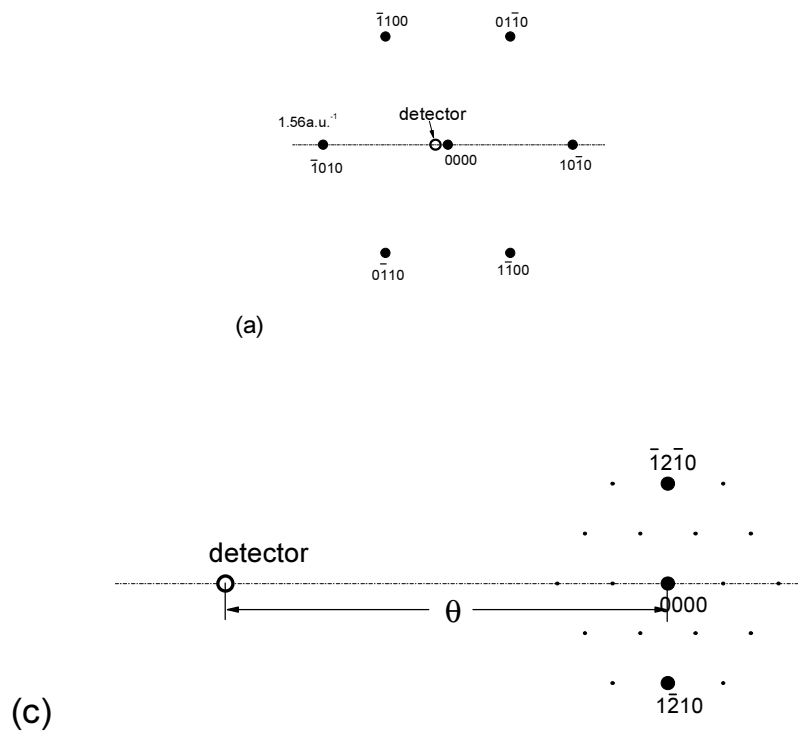


Figure 4.20. Sketch of the measurement geometry in the diffraction plane. The diffraction pattern was shifted with respect to the detector to measure spectra at different momentum transfers (a) for ELNES measurements, (b) for ECOS measurements.

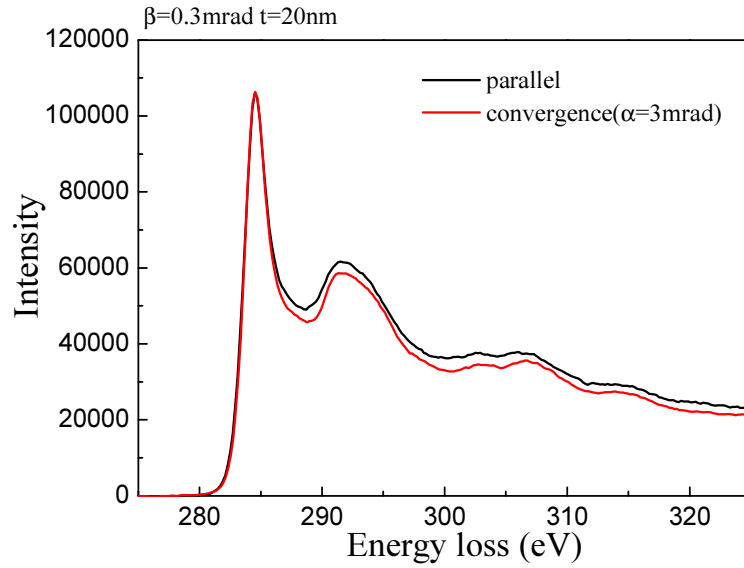


Figure 4.21 ELNES of carbon K-edge in graphite for momentum transfer in the forward direction after a power-law type background subtraction. The collection angle $\beta = 0.3 \text{ mrad}$. A nearly parallel incident beam was used for the black line. For the red line, a convergent incident beam was used, convergence angle $\alpha = 3.5 \text{ mrad}$.

peak as the scattering angle increases. For $\theta = 2.8 \text{ mrad}$, the π^* peak has virtually disappeared. R. Klie *et al.* [74] have calculated the fractional contribution from π^* and σ^* as a function of scattering angle with the incident beam parallel to the c axis for a uniaxial crystal. The variation in relative intensity with increasing momentum transfer is explained by noting that transitions to the π^* band are driven by the longitudinal component of momentum transfer that is parallel to the c axis. The σ^* transitions are coupled to the perpendicular momentum transfer q_{\perp} (see Fig. 2.3). At a given magnitude of energy loss, the direction of the momentum transfer changes rapidly from parallel to perpendicular to the incident beam as the electron scattering angle increases, due to the conservation of momentum [75]. In this experiment, there is a minimum momentum transfer q_{\min} , which has the form $q_{\min} \cong k_0 \theta_E$, and q_{\min} is essentially along the incident beam direction. For a 200 keV incident electron beam and an energy loss of roughly 300 eV, we have $\theta_E = 0.83 \text{ mrad}$. It is worth noting that the collection angle $\beta = 0.3 \text{ mrad}$ was used in our ELNES measurements, which is much smaller than the characteristic angle. For the spectrum obtained at $\theta = 0$, the momentum transfer $q \approx q_{\min}$ only has a component that is parallel to the incident beam direction—in this case along the graphite c axis. So the C K-edge ELNES at scattering angle $\theta = 0$ is the $1s \rightarrow \pi^*$ transition in our experiments. The ELNES for $\theta = 0$ is shown in Figure 4.23 along with theoretical calculations for the π^* component [72]. A good agreement between experiment and calculation is obtained especially in the edge region below 295 eV.

Further, since there is no contribution from σ^* transitions at the π^* peak, we may normalize the π^* result to the large scattering angle result at 284.5 eV (see Figure

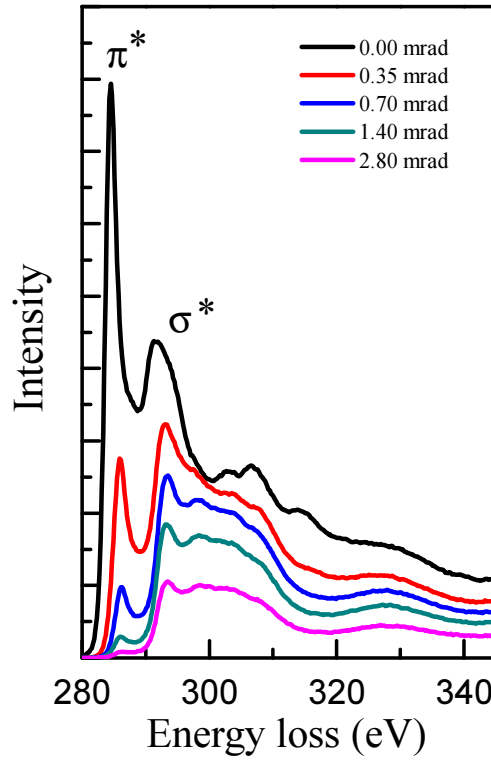


Figure 4.22 Experimental ELNES of the carbon K-edge in graphite at five scattering angles after a power-law type background subtraction.

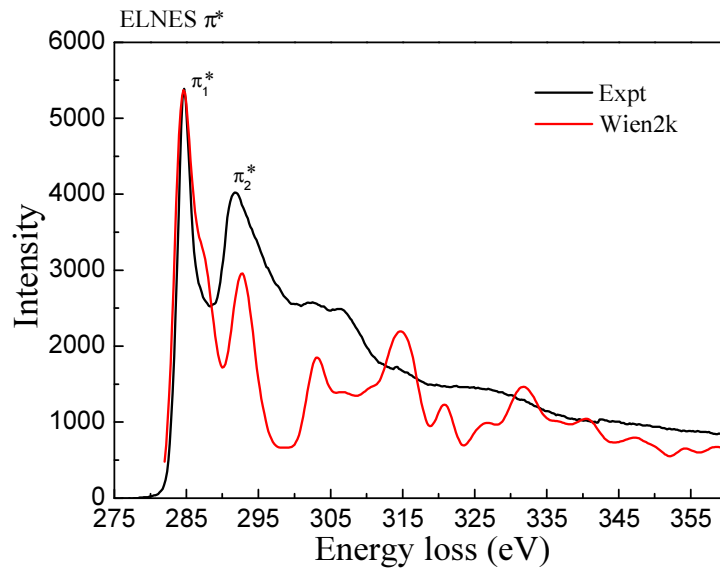


Figure 4.23 The π^* component of C K-edge ELNES along with theoretical calculation from WIEN2K package[72]. The experimental result was obtained at scattering angle $\theta = 0$.

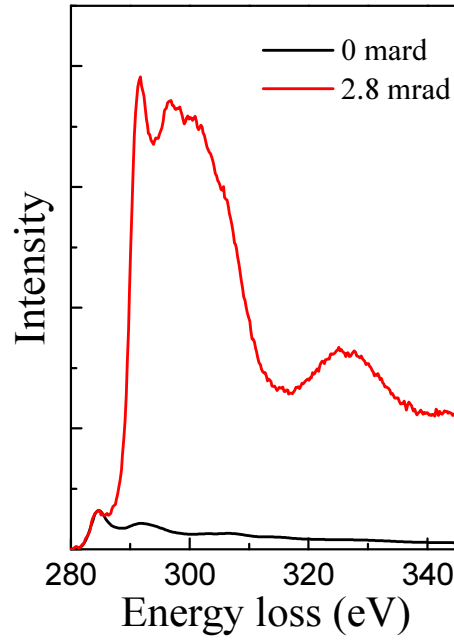


Figure 4.24 The carbon K-edge ELNES of the graphite at scattering angle $\theta = 2.8 \text{ mrad}$ along with the contribution from π^* transitions.

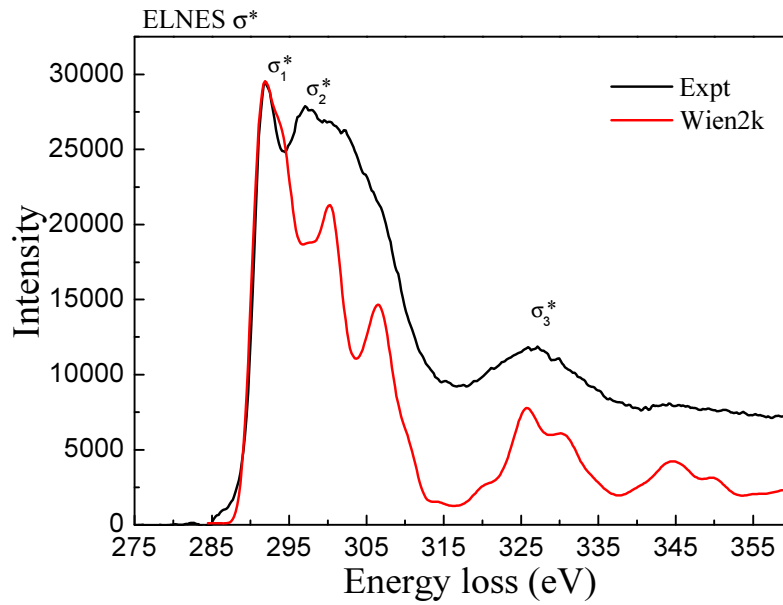


Figure 4.25 The σ^* component of C K-edge ELNES along with theoretical calculation from WIEN2K package[72]. The σ^* component was obtained at $\theta = 2.8 \text{ mrad}$ after the appropriate π^* contribution was subtracted.

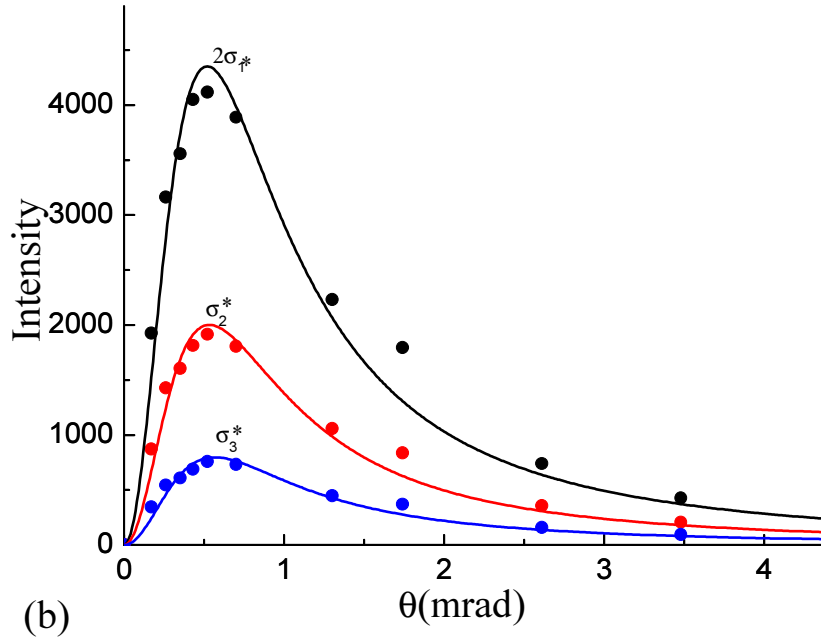
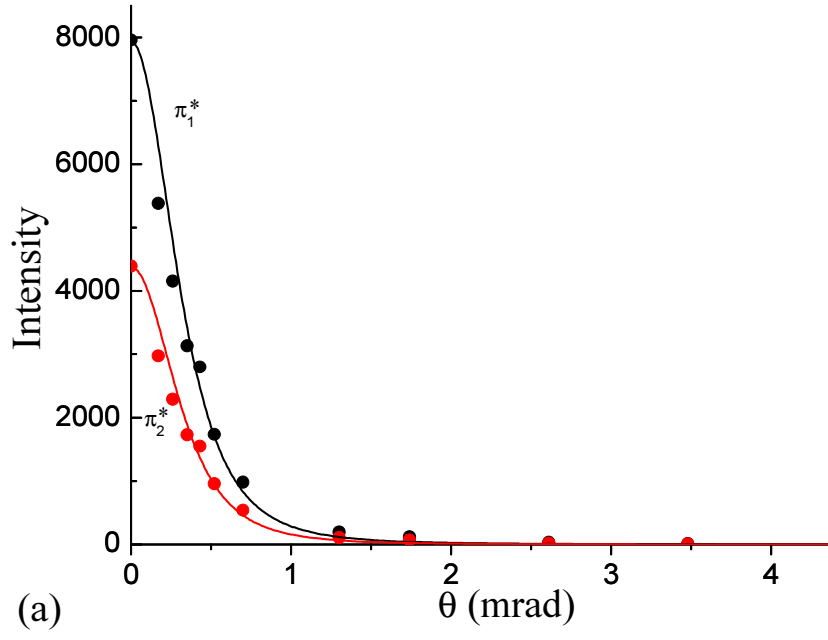


Figure 4.26. Theoretical and experimental angular distributions of (a) π^* and (b) σ^* intensities of the peaks in the ELNES of graphite[66]. The σ_1^* curve has been magnified by a factor of 2.

4.24) and subtract this data to obtain the scattering intensity that is only due to the σ^* final states. This procedure completely separates the π^* and σ^* components. The results for the σ^* component is shown in Fig. 4.25 also along with the theoretical calculation [72]. The overall agreement between experiment and theory is good. The calculated spectra have been convolved with a Gaussian to take into account the experimental energy resolution.

Leapman *et al* [66] give the expressions for the angular dependence of these two components. When the specimen is oriented so that the c -axis is parallel to the incident beam, $I(\pi^*) \propto \theta_E^2 / (\theta^2 + \theta_E^2)^2$ and $I(\sigma^*) \propto \theta^2 / (\theta^2 + \theta_E^2)^2$. The π^* ELNES has a narrow forward-peaked angular distribution; conversely, the σ^* ELNES is zero at $\theta = 0$ and rises to a maximum at $\theta = \theta_E$; the sum of these two components is a Lorentzian. Fig. 4.26 (a) and (b) show the angular distributions of π^* and σ^* peaks in ELNES after separation. The agreement is good, within the experimental uncertainty.

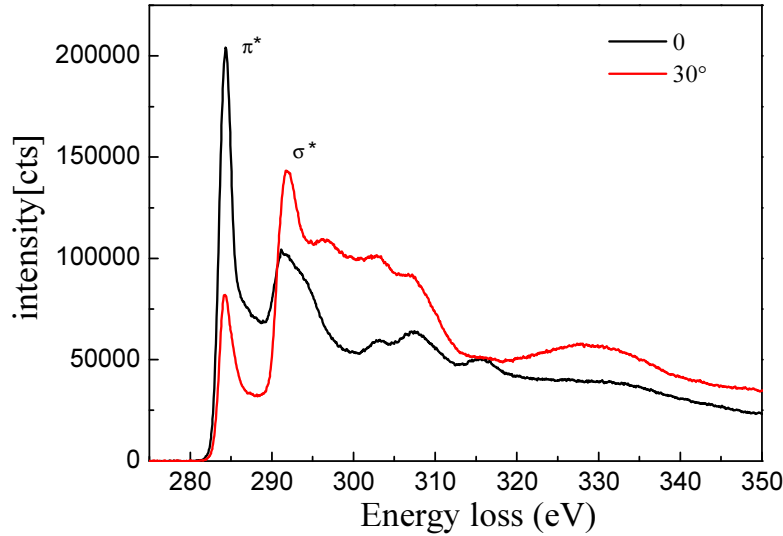


Figure 4.27 The carbon K-edge of the graphite in the direction of the incident beam. The black line was obtained at the incident beam parallel to the c axis. The red line was obtained at the angle 30° between the incident beam and the c axis.

The π^* and σ^* component of C K-edge ELNES in graphite can be also separated by tilting sample. Fig. 4.27 shows the ELNES of graphite by tilting specimen recorded in the direct beam direction. The principle is the same as tilting incident beam direction. We found the relative intensities of π^* and σ^* peaks change slowly with increasing the tilting angles not as increasing momentum transfers. In the case, we increased the momentum transfer (Fig. 2.3):

$$q_{\perp} = k_b \sin \theta, \quad (4.1)$$

$$q_{\parallel} = k_a - k_b \cos \theta + k_a \theta_E, \quad (4.2)$$

while $k_b \approx k_a$, so

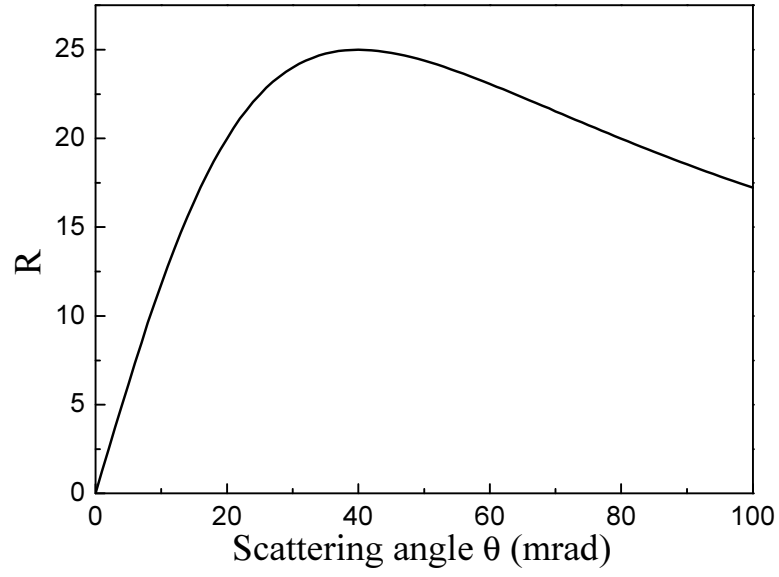


Figure 4.28 The scattering angle dependence of the ratio $R = q_{\perp}/q_{\parallel}$.

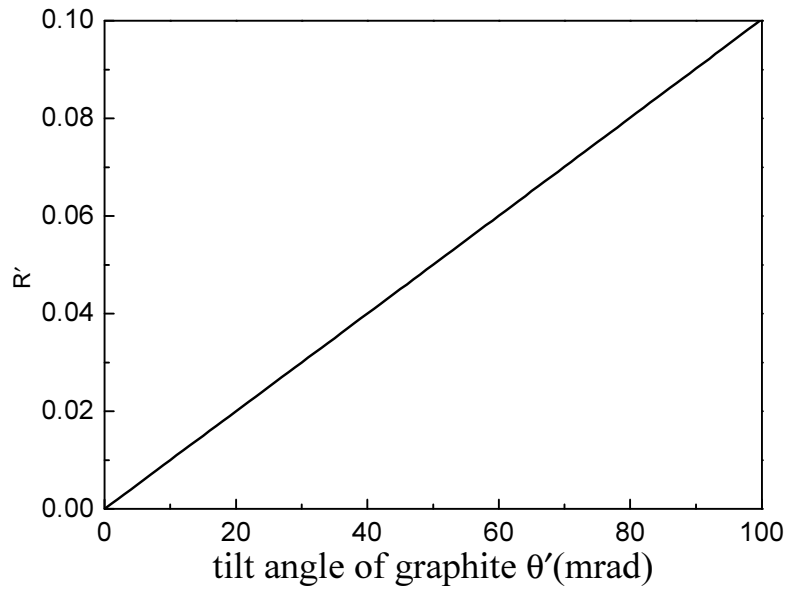


Figure 4.29 The tilt angle dependence of the ratio $R = q_{\perp}/q_{\parallel}$

$$R = \frac{q_{\perp}}{q_{\parallel}} = \frac{\sin \theta}{1 - \cos \theta + \theta_E}. \quad (4.3)$$

The ratio of q_{\perp} to q_{\parallel} with respect to scattering angle is plotted in Fig. 4.28. The momentum transfer changes rapidly from parallel to perpendicular to the incident beam as scattering angle increases.

In the case of tilting sample, the momentum transfer is a constant $q \approx q_{\min}$,

$$q_{\perp} = q_{\min} \sin \theta', \quad (4.4)$$

$$q_{\parallel} = q_{\min} \cos \theta', \quad (4.5)$$

here θ' is the tilt angle of the graphite, so,

$$R' = \frac{q_{\perp}}{q_{\parallel}} = \frac{\sin \theta'}{\cos \theta'} = \tan \theta'. \quad (4.6)$$

The ratio R' with respect to the tilt angle is plotted in Fig. 4.29.

From Figs. 4.28 and 4.29, we obtain the the ratio of q_{\perp} to q_{\parallel} changes much slower for tilting sample than increasing scattering angle in the moderate angle region. That's why we can still observe large contributions from π^* transitions even at we tilt sample 30° .

4.2.3.2 ECOSS

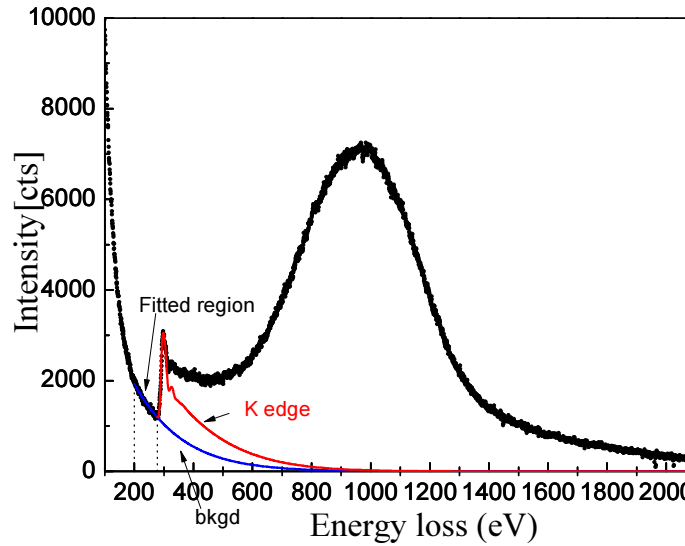


Figure 4.30 Measured raw data (black line) for Compton scattering of graphite at a scattering angle $\theta = 64 \text{ mrad}$, and a total exposure time $t = 50 \text{ s}$; the simulated elastic background (blue line) and the component of the C-K edge (red line) are also shown.

When recording the electron energy-loss spectrum at large scattering angle, the electron Compton scattering peak will present. This is the electron Compton scattering spectrum in the electron microscope, which can be used to obtain the

ground-state momentum wave function of the electrons in the sample. Fig. 4.30 shows the measured raw ECOSS data from graphite at a scattering angle of 64 mrad. Two spectra with an exposure time of 25 seconds each were taken under the same experimental conditions except for different recorded energy loss window and subsequently spliced together. The carbon K-edge is clearly visible. The momentum transfer was determined separately by Eq (2.24). This gave a momentum transfer of $q = 8.5$ a.u.

The background subtraction was achieved by parameterized simulations of combined elastic and inelastic scattering events [35, 76]. The principle of this method has been introduced in the Chapter 3. A full description of the procedure is also given by Su et al [35, 36]. For the plasmon scattering, the plasmon energy E_p , which was measured (at $\theta \approx 0$) to be $E_p^\pi = 5.8$ eV and $E_p^\sigma = 26.6$ eV, and the plasmon linewidth ΔE_p , which was measured to be $\Delta E_p^\pi = 3.6$ eV and $\Delta E_p^\sigma = 11.5$ eV, respectively. The simulated elastic background is shown in Fig. 4.30. To define the background proportionality factor, a range starting at 100 eV before the carbon K edge was fitted in our simulations.

We have got the angular and energy dependence of π^* ELNES and σ^* ELNES components in the preceding section. This made it possible to determine the contributions of the K-edge in the measured ECOSS data. The simulated contribution of the K-edge in ECOSS is also shown in Fig. 4.30.

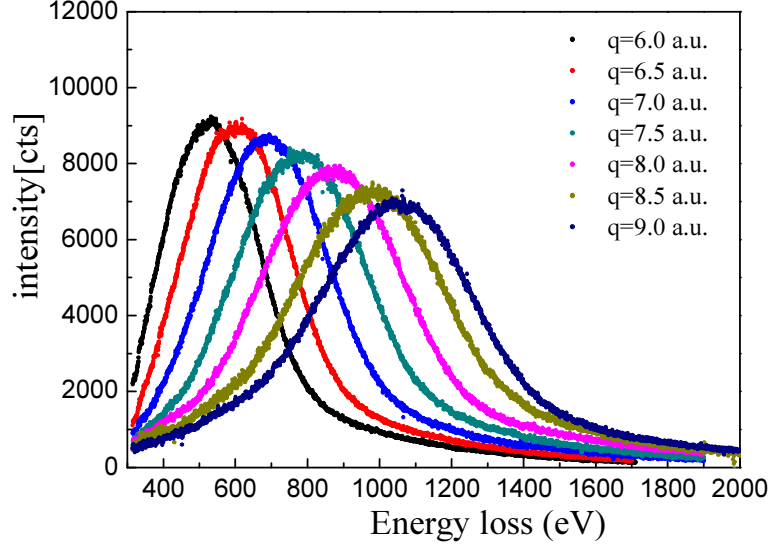


Figure 4.31 Experimental electron energy loss Compton spectra for graphite taken at scattering angles from 45 to 68 mrad corresponding momentum transfer from 6.0 to 9.0 a.u. after background and K edge subtraction.

In Fig. 4.31, we show experimental electron energy loss Compton spectra for graphite taken at 7 different scattering angles after the background and K-edge were subtracted. It is worth to point out that the directions of momentum transfers predominantly lay in the basal plan at these large scattering angles. We thus

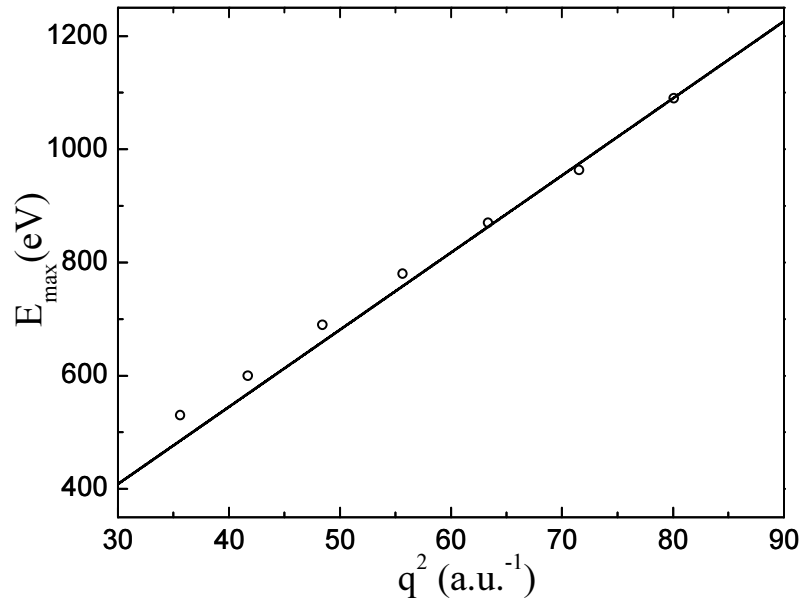


Figure 4.32 The momentum transfer dependence of electron Compton peak. The circles are experimental results and the line comes from free electron model $E = \frac{q^2}{2m_e}$.

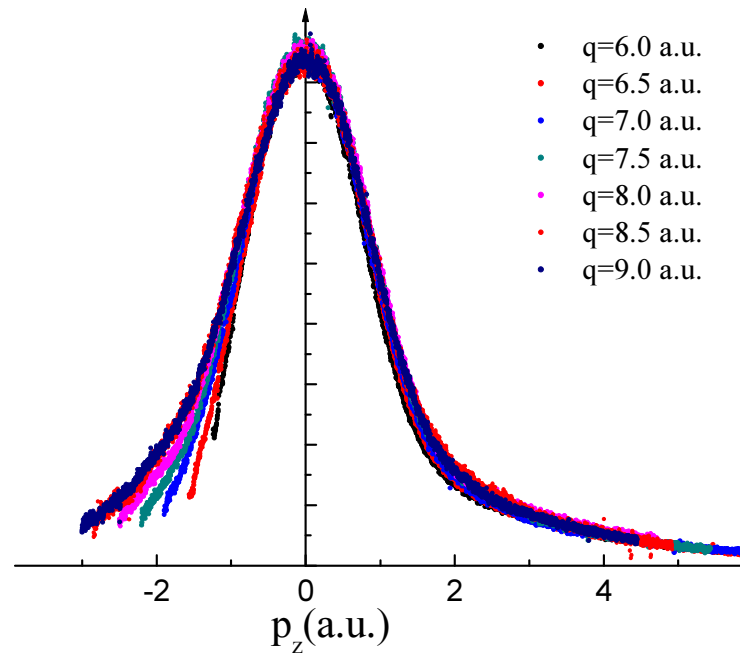


Figure 4.33 The total electron Compton profiles in momentum scale at seven momentum transfers.

predominantly probed the σ ground state of graphite in this experiment. As the scattering angle increases, the spectrum shifts to higher energy losses. The energy loss at the electron Compton scattering peak, E_{\max} , was determined by polynomial fitting to the top of the spectrum. The dependence of E_{\max} on the momentum transfer is shown in Fig. 4.32. Note that the dispersion relation looks much like that of a free electron for the momentum transfers larger than $q = 8.0 \text{ a.u.}$

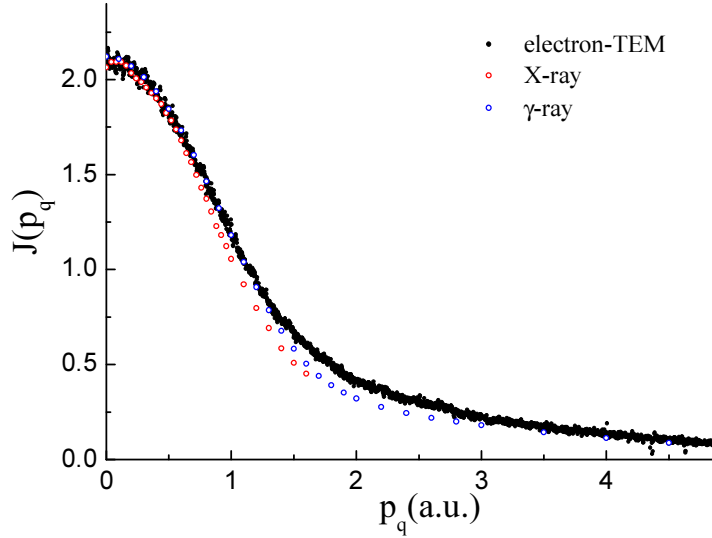


Figure 4.34. Experimental total electron Compton profile at a momentum transfer 8.5 a.u. in a TEM along with data from X-ray and γ -ray photon sources [77, 78].

The spectrum was then converted to momentum scale using Eq. (2.25). Fig. 4.33 shows the experimental ECOSS of graphite in momentum scale. The spectra have been normalized at zero momentum so that the peak height of each profile is the same. The center of the peak is largely determined by the narrow momentum distribution of the valence electrons, whereas the tails are mainly due to the broad core shell distribution [79]. The profiles become broader and more symmetric with increasing momentum transfer. This is mainly due to the fact that the contributions from core electrons increase with increasing momentum transfer. The positive ($p_q \geq 0$) components of the profiles don't show substantial changes after momentum transfers larger than $q = 7.0 \text{ a.u.}$ The negative components of the profiles broaden with increasing momentum transfer until $q = 8.5 \text{ a.u.}$ This can be explained in the following, for momentum transfers larger than $q = 8.5 \text{ a.u.}$, the energy transfer is large enough relative to the binding energy of the core electrons and the Compton peak is so far away from core ionization edge, the impulse approximation works. So to do ECOSS experiment in the TEM required recording EELS at the scattering angle as large as possible and avoiding the core ionization edge in the Compton scattering region. On the other hand, the cross section for inelastic electron scattering decreases with the fourth power of the scattering angle [40]. It is important to keep the

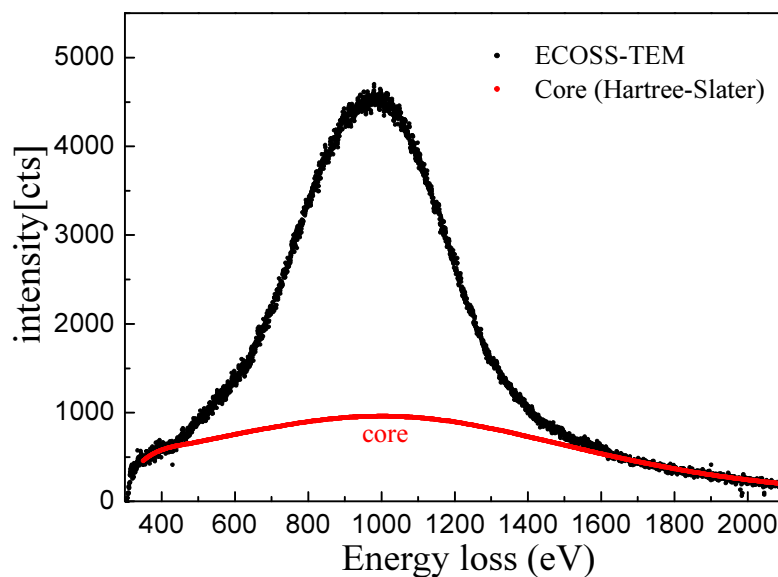


Figure 4.35 The measured ECOSS (black) at a momentum transfer of $q=8.5$ a.u. as a function of energy loss in TEM. Theoretical core contributions (red) were calculated by the Hartree-Slater method.

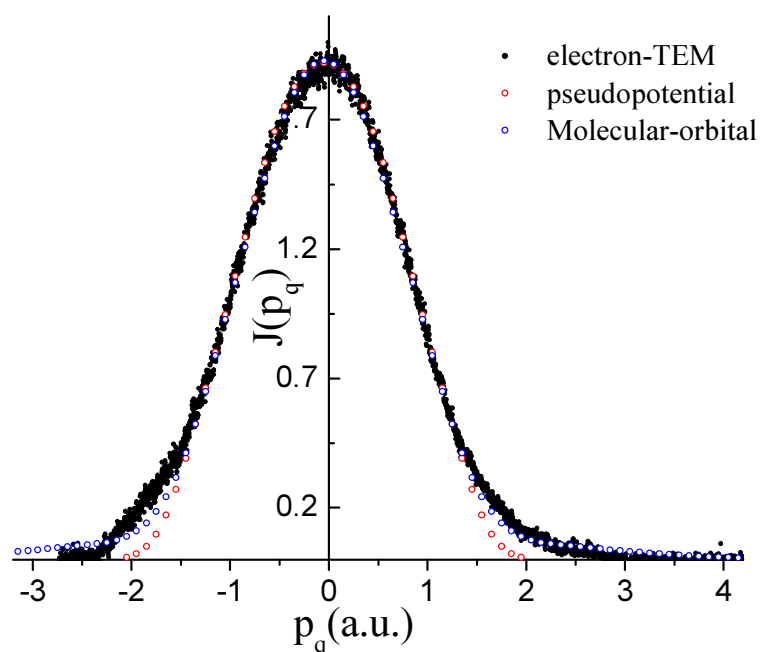


Figure 4.36 The experimental valence electron Compton profile at a momentum transfer of $q=8.5$ a.u. in a TEM, compared to theoretical results of W.A. Reed et al [80]. The theoretical data have been convolved with the experimental broadening 0.4 a.u. FWHM Gaussian curve for comparison.

scattering angle as low as possible to maximize the recorded intensity and reduce the exposure time. For carbon materials, one can get a reasonable ECOSS signal at a scattering angle of 64 mrad ($q = 8.5\text{ a.u.}$). This satisfies the conditions that (i) the energy transfer is large compared to the binding energy of the atomic electron and (ii) the momentum transfer is large compared to the relevant momentum of the atomic electron.

For comparison with normalized values measured with photons scattering by U. Bonse *et al.*[77] and R. Tyk *et al.*[78]. The total electron Compton profile along with the photon Compton profile are plotted in Fig. 4.34. U. Bonse *et al.*[77] used 22.1 KeV X-rays and high efficiency solid-state detectors (SSDs). R. Tyk *et al.*[78] employed an intrinsic Ge detector, using 60 keV γ rays. It is seen that the electron Compton scattering technique in TEM gives a reasonably good agreement with the conventional photon technique.

Since our interest is in the valence Compton profile, the core contribution has to be subtracted by theoretical calculations. A Hartree-Slater central field model is used for calculating them [42]. In solids, the momentum distribution of the valence electrons is substantially different from that of electrons in a free atom. The momentum distributions of the core electrons, however, are very similar for solids and free atoms. Therefore, a Hartree-Slater free atom calculation is sufficient to determine the contributions of the core electrons to the total Compton spectrum. The theoretical core contribution is then normalized by fitting at the tails of the total ECOSS profile where the valence contributions are negligible. The experimental ECOSS profile at a momentum transfer of $q = 8.5\text{ a.u.}$ along with the simulated core contribution is shown in Fig. 4.35.

The valence electron energy loss Compton spectrum was transformed to the generalized oscillator strength (GOS). Then, the GOS was normalized to the number of electrons in outer shells, according to the Bethe sum rule[61]. Finally, the absolute GOS was converted to a Compton profile within the binary encounter approximation [28, 30]. In Fig. 4.36, we compare the experimental and theoretical valence Compton profile of graphite in the basal plane [80]. The resulting profiles are in good agreement with our data.

4.2.4 Anisotropy of ECOSS in graphite

Compton profile is reasonably sensitive to the state of the valence electrons of the atoms which combined to form solid [38]. The anisotropy of directional Compton profiles reflects differences of bonds in solid at specific crystallographic directions and provides valuable information about the electronic state of outer electrons which is responsible to create solids and their properties. In addition, anisotropy measurement is a useful test of the quality of a theoretical model as during anisotropy studies effects of experimental factors (multiple scattering, background, detectors, theoretical core Compton scattering contribution and so on) can be reduced or eliminated. Nowadays, most high-resolution Compton scattering measurements based

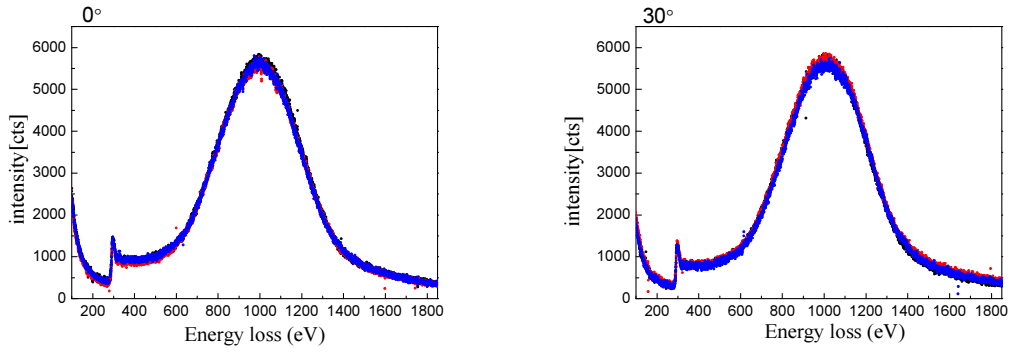


Figure 4.37 The ECOSS data of graphite were measured three times with exposure time 100s each. The graphite was tilted (a) 0° and (b) 30° with respect to the incident beam. The collection angle $\beta = 1.2 \text{ mrad}$.

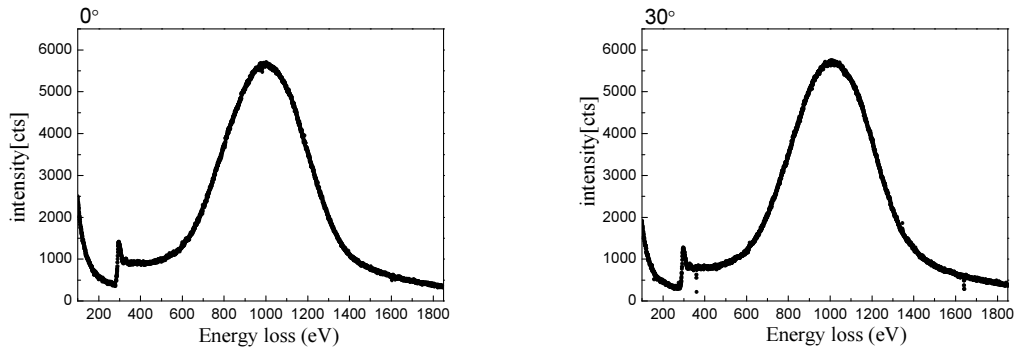


Figure 4.38 Experimental ECOSS data of graphite after average three raw spectra. The graphite was tilted (a) 0° and (b) 30° with respect to the incident beam. The collection angle $\beta = 1.2 \text{ mrad}$.

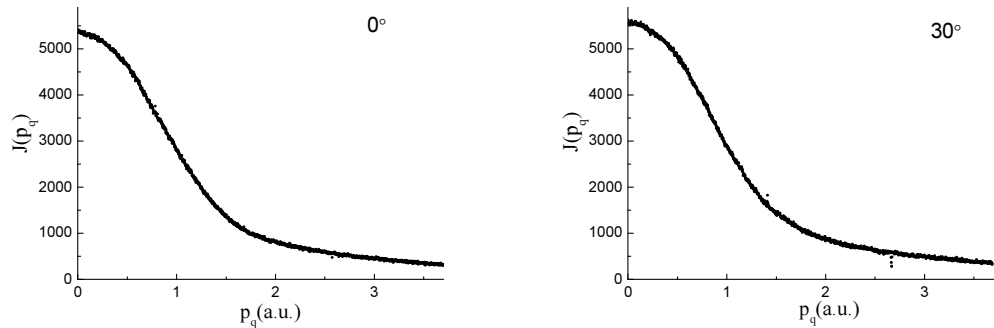


Figure 4.39 Experimental electron Compton profile of graphite after background and K edge were subtracted. The graphite was tilted (a) 0° and (b) 30° with respect to the incident beam. The collection angle $\beta = 1.2 \text{ mrad}$.

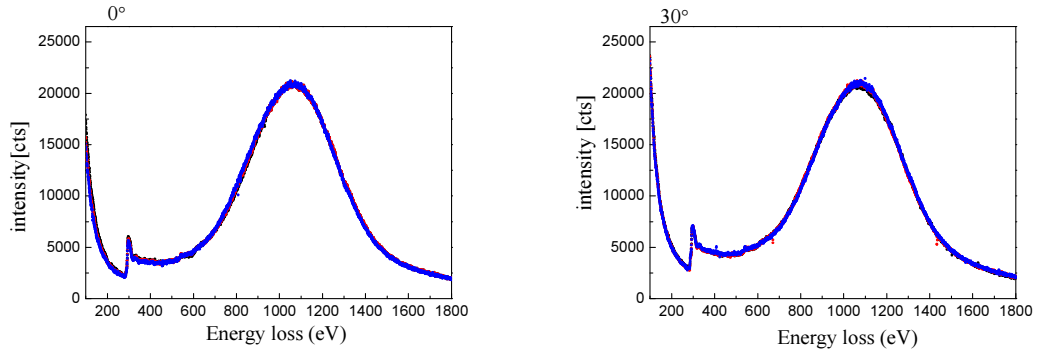


Figure 4.40 The ECOSS data of graphite were measured three times with exposure time 100s each. The graphite was tilted (a) 0° and (b) 30° with respect to the incident beam. The collection angle $\beta = 2.0 \text{ mrad}$.

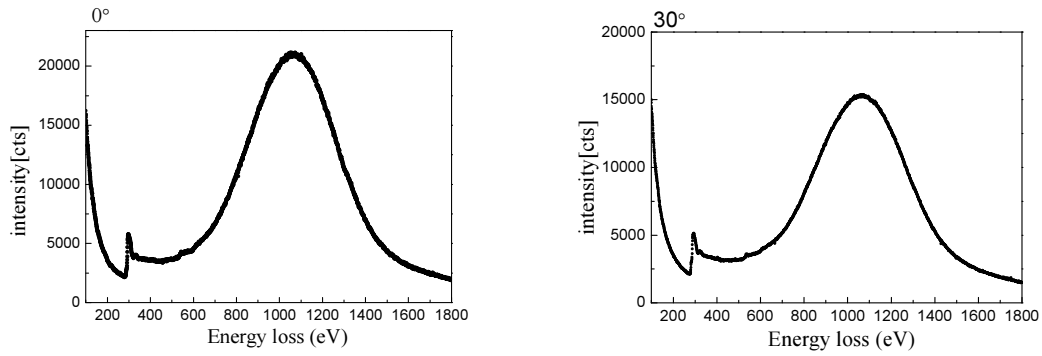


Figure 4.41 Experimental ECOSS data of graphite after average three raw data. The graphite was tilted (a) 0° and (b) 30° with respect to the incident beam. The collection angle $\beta = 2.0 \text{ mrad}$.

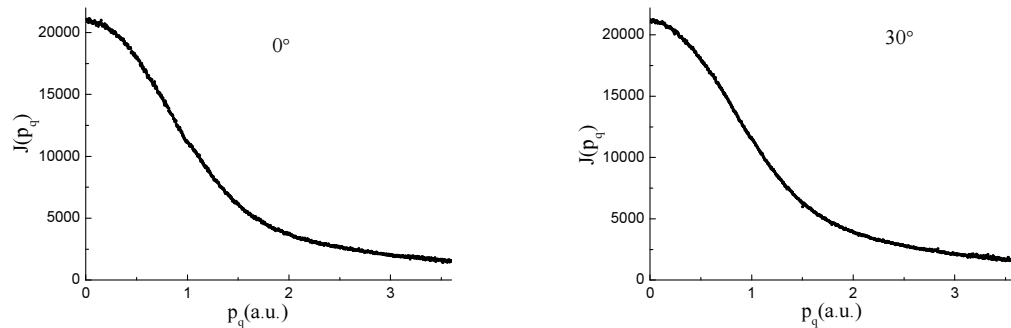


Figure 4.42 Experimental electron Compton profile of graphite after background and K edge were subtracted. The graphite was tilted (a) 0° and (b) 30° with respect to the incident beam. The collection angle $\beta = 2.0 \text{ mrad}$.

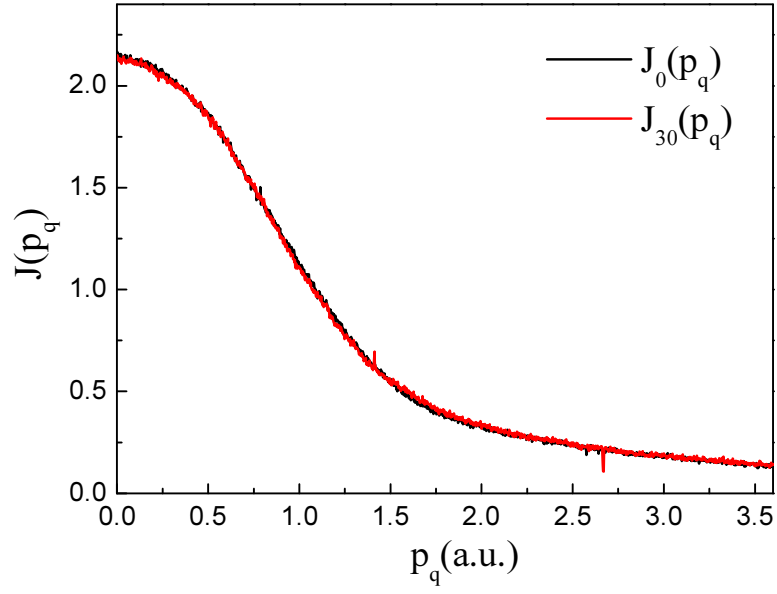


Figure 4.43 Experimental electron Compton profiles of graphite with collection angle $\beta = 1.2 \text{ mrad}$.

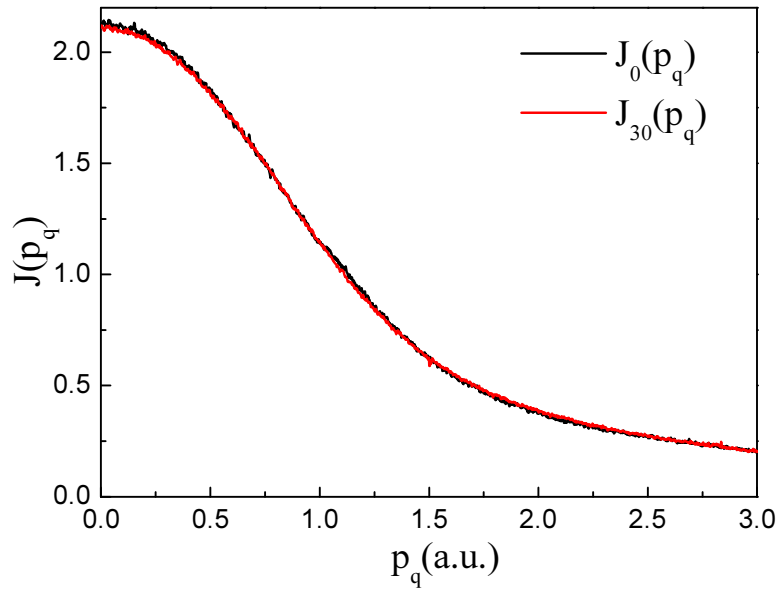


Figure 4.44 Experimental electron Compton profiles of graphite with collection angle $\beta = 2.0 \text{ mrad}$.

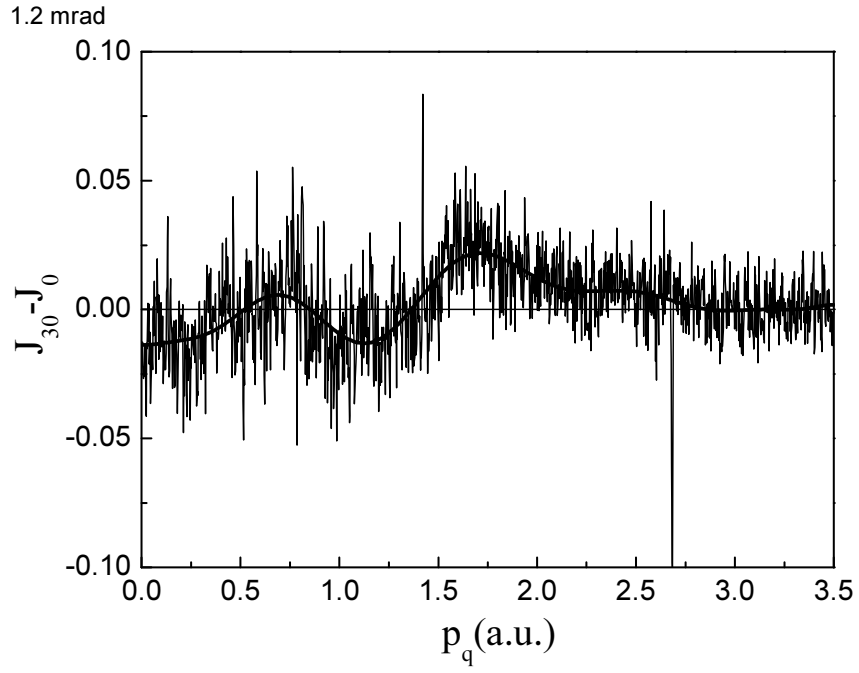


Figure 4.45 The electron Compton profile anisotropy of the graphite in ECOSS experiment with collection angle $\beta = 1.2 \text{ mrad}$. The solid line was obtained by polynomial fit.

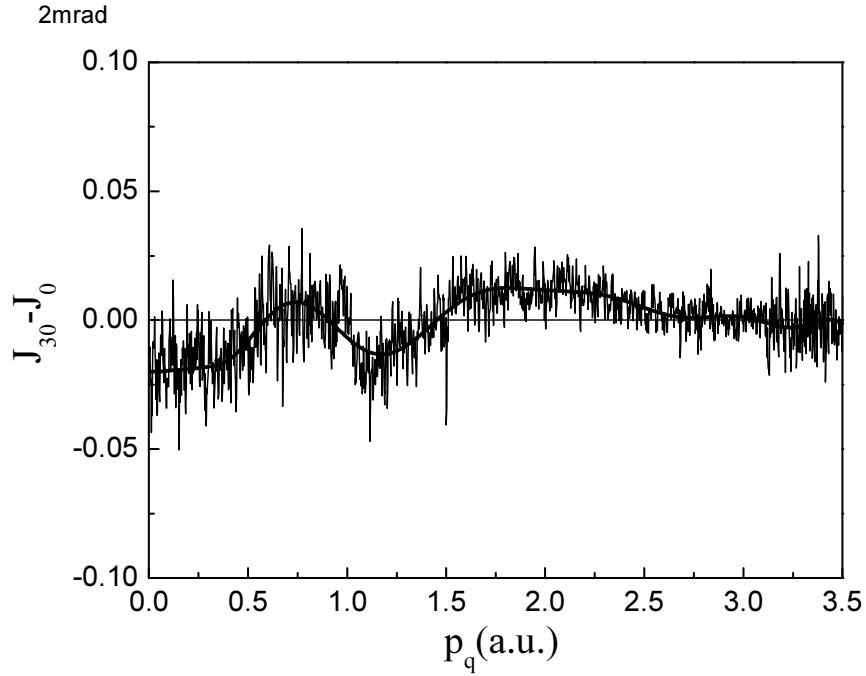


Figure 4.46 The electron Compton profile anisotropy of the graphite in ECOSS experiment with collection angle $\beta = 2.0 \text{ mrad}$. The solid line was obtained by polynomial fit.

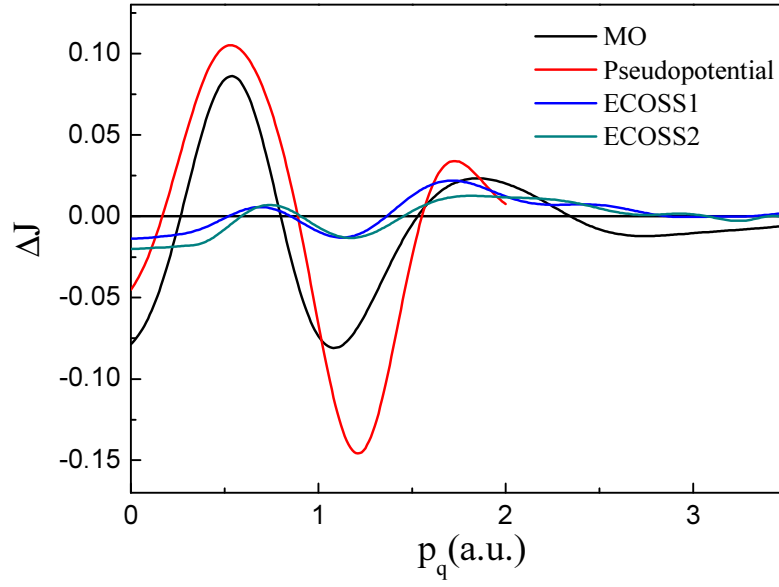


Figure 4.47 Compton profile anisotropy of graphite. MO and Pseudopotential represent the molecular-orbital and pseudopotential calculation respectively [80]. ECOSS1 and ECOSS2 are our measurement with collection $\beta = 1.2 \text{ mrad}$ and $\beta = 2.0 \text{ mrad}$, respectively.

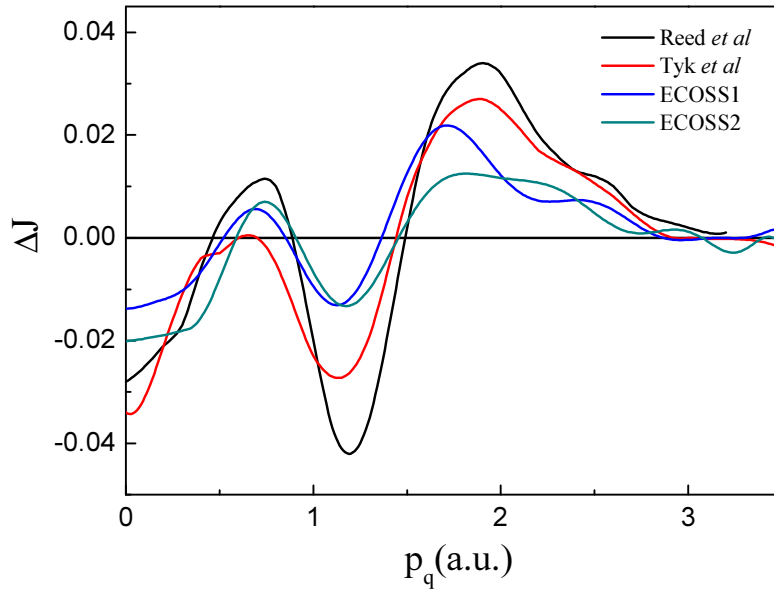


Figure 4.48 Compton profile anisotropy of graphite. The black line is from Reed *et al* [80] measurement with 159-keV γ rays. The red line is from Tyk *et al* [78] measurement with 59.54-keV γ rays. ECOSS1 and ECOSS2 are our measurements with collection $\beta = 1.2 \text{ mrad}$ and $\beta = 2.0 \text{ mrad}$ respectively.

on synchrotron radiation sources have been devoted to determine the directional Compton profiles [18, 81-84]. The synchrotron-based Compton scattering experiment is very large and expensive. ECOSS with high-resolution yields results equivalent to photon Compton scattering on the momentum distribution of the scatter. The improvements of ECOSS technique in intensity, resolution and statistical accuracy make anisotropy measurements of electron Compton profile possible to carry out in the TEM.

Anisotropy of Compton profile in graphite has been studied by a number of groups in both theory and experiment [14, 78, 80, 85-87]. In all previous measurements, they found the Compton profile in the c axis direction (J_{\parallel}) is smaller than the Compton profile in the direction of perpendicular to the c axis (J_{\perp}) near zero momentum [78, 87]. The sample can be tilted $0^{\circ} \sim 35^{\circ}$ in the TEM. Directional ECOSS was measured in two cases: the incident beam was parallel to c axis (J_0) or the sample was tilted about 30° with respect to the incident beam (J_{30}). Three spectra were measured for each case to get a better signal-to-noise ratio and statistical accuracy, as shown in Figs 4.37 and 4.40. One spectrum was obtained by recording two times with different energy loss window with an exposure time of 55s each. For Figs 4.37-4.39, the collection angle $\beta = 1.2 \text{ mrad}$ was used. For Figs 4.40-4.42, the collection angle is $\beta = 2.0 \text{ mrad}$. The electron Compton profiles of graphite for two cases are shown in Figs 4.43 and 4.44.

In Figs 4.45 and 4.46, the experimental anisotropy of $J_{30}-J_0$ along with fitting results by polynomial fit is shown. In the previous section, we pointed out the J_0 mainly probed the electron momentum distribution in the basal plane of graphite in this experiment (so J_0 equals the J_{\perp} in the previous anisotropy measurements [20, 25-28]). The largest tilt angle cannot exceed 35° in the TEM, so it is impossible to obtain the J_{\parallel} directly in our ECOSS experiment. In Figure 4.47 and 4.48, we compare our measured electron Compton profile anisotropy $J_{30}-J_0$ in graphite with the previous works of $J_{\parallel}-J_{\perp}$ in theory and experiment, respectively. The first peak at $p_q \approx 0.7 \text{ a.u.}$ arises from the π bonding anisotropy along the c axis in graphite [80, 85]. The anisotropy curves appear to have same features in all of them. The amplitudes of ECOSS measurements are smaller compared to other measurements. This may be due to variations in tilt angle, and to mixing of J_{\parallel} and J_{\perp} component via different scattering.

4.3 Amorphous carbon film

Amorphous carbon is a material which has been increasingly important in recent years, due to its superior mechanical properties. The amorphous carbon materials can be as hard as diamond or has elasticities closer to the material alumina or wolfram[88]. The mechanical, optical, electrical, thermo-electric and chemical properties of carbon materials depend on the type of bonding between carbon atoms. Usually, amorphous carbon films comprise a combination of sp^2 and sp^3 hybrids type of bonds [89]. Hardness mostly depends on the concentration of sp^3 hybrids bond or tetrahedrally

bonded atoms [88, 90]. In the past years, the electron energy-loss near edge structure (ELNES) and near edge X-ray absorption fine structure (NEXAFS) have been the most used techniques to probe unoccupied electronic states and determine the proportion of sp^3 bonded atoms of the amorphous carbon films [72, 90-92]. Unlike the graphite, the ground-state electronic properties of the amorphous carbon films were not characterized by the Compton profile using photons. The first electron Compton profile of the amorphous carbon film was obtained in the TEM by B.G. Williams in 1981 [32]. In this work, the ECOSS of the amorphous carbon film was measured in several minutes which is much shorter than 1 hour used in 30 years ago.

4.3.1 Experimental details

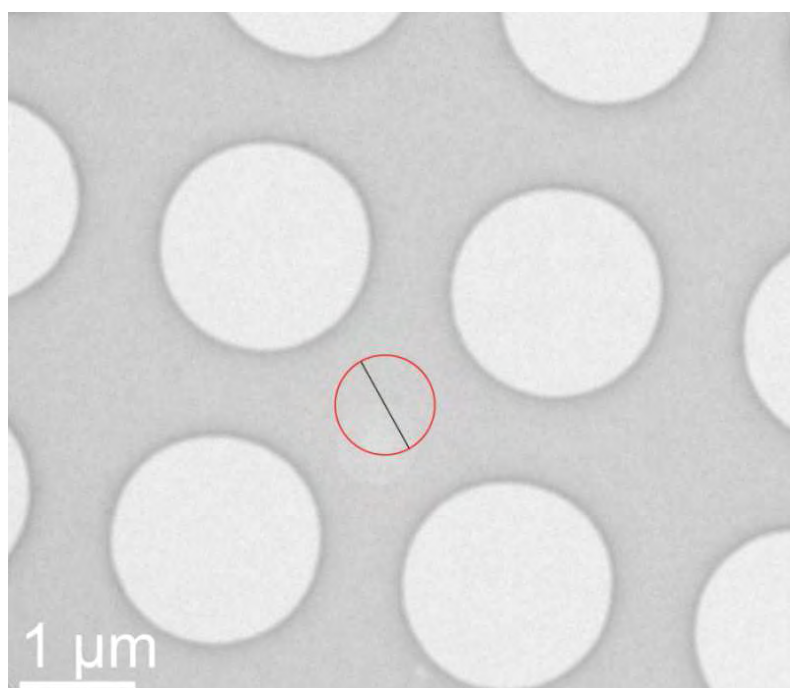


Figure 4.49 The image of the amorphous carbon film in this experiment. 800nm in diameter was chosen (red circle).

First, the amorphous carbon films of a quantifoil TEM grid (Quantifoil Micro Tools GmbH, Jena, Germany) which was used in graphite or graphene sample preparation were chosen in this experiment as shown in Fig. 4.49. The thickness of the sample was about 20nm with a 800nm diameter probe. All the experimental conditions are the same as graphite in section 4.2 except the scattering geometry. Films of this sample yields rings in electron diffraction, see Fig. 4.50. It's impossible to reduce the effects from diffuse by tilting sample. The scattering angle was firstly determined by using the diffraction pattern of the graphite. Then the electron beam was shifted to the chosen amorphous carbon film. The spectra were recorded in arbitrary direction away from the incident beam with exposure time 60s.

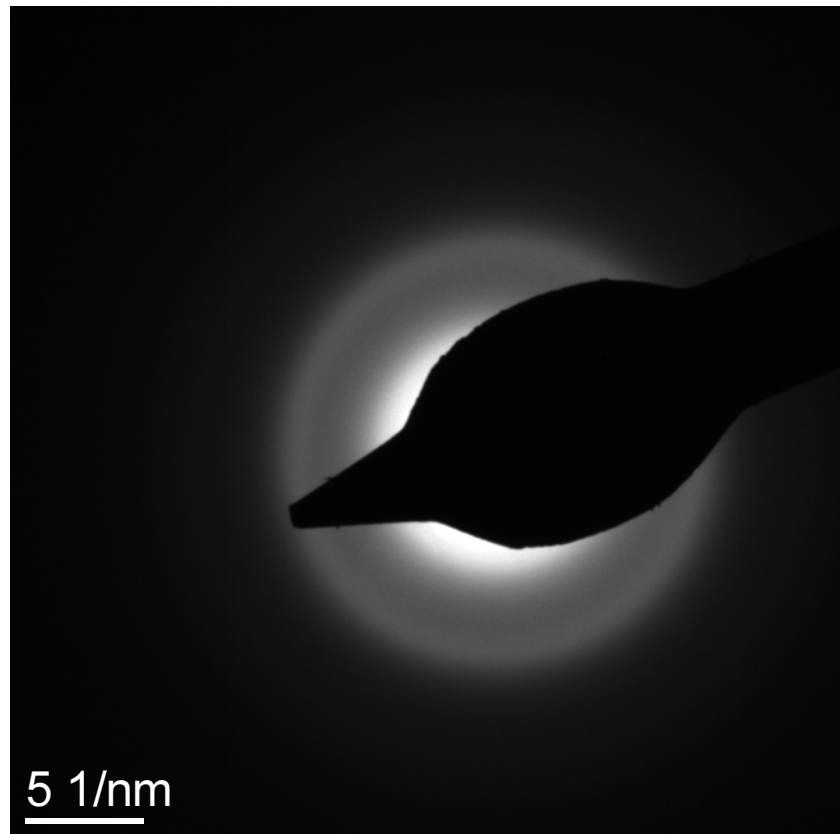


Figure 4.50 The diffraction pattern of the amorphous carbon film.

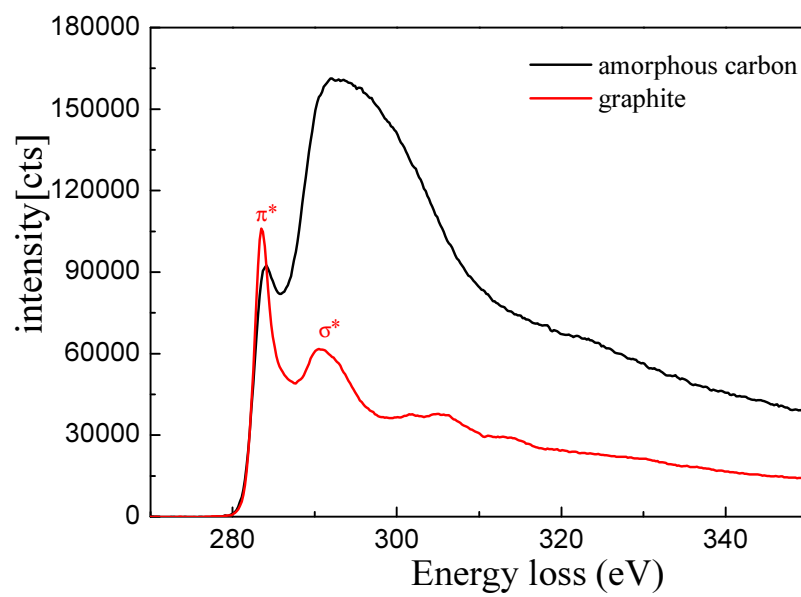


Figure 4.51 The measured electron energy-loss spectra in the carbon K-edge region from (a) amorphous carbon and (b) graphite in the forward direction.

4.3.2 Results

The measured K-edge of carbon from the amorphous carbon film together with data from graphite in the c axis direction are shown in Fig. 4.51 after a power-law type background was removed. There is still a broadening π^* peak in spectrum of the amorphous carbon film. This feature indicates that the amorphous carbon contains a small fraction of sp^2 bonded carbon atoms [93]. A comparison of the K-edge ELNES of the graphite with the amorphous carbon can be used to calculate the proportion of the sp^2/sp^3 hybrids in amorphous carbon materials [72, 93, 94].

The measured electron Compton profile of the amorphous carbon film at the scattering angle 64 mrad (the corresponding momentum transfer $q=8.5$ a.u.) is plotted in Fig. 4.52. The electron Compton profile of the graphite with the incident beam is parallel to the c axis is also shown in Fig. 4.52. The discrepancy occurs at low momentum range ($0 \leq p_q \leq 2$ a.u.). Profiles overlap each other after the momentum larger than 2 a.u. This behavior is expected as the low momentum region of profiles represent the bonding electrons while the tails of spectra mainly come from core electrons (1s orbitals in carbon). The obvious difference at momentum around 1 a.u. may be due to the π electrons in graphite. The theoretical calculation has shown that the peak of π electrons Compton profile of the graphite occurs at momentum

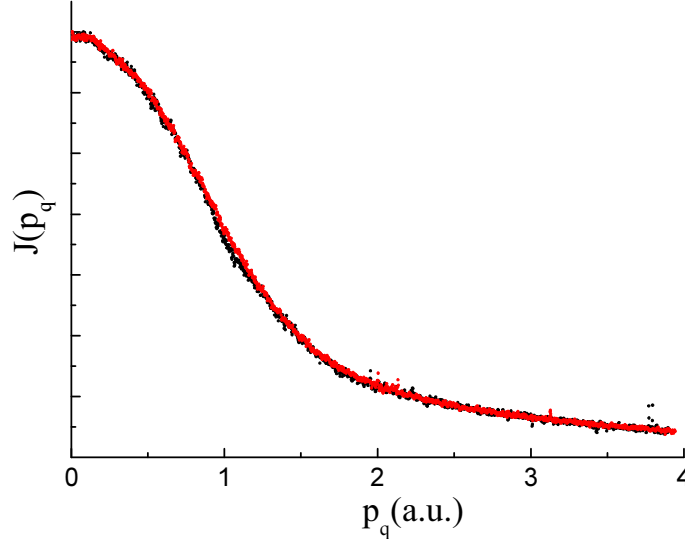


Figure 4.52 The electron Compton profile of (a) the amorphous carbon film (black dots), (b) the graphite with the incident beam is parallel to c axis (red dots).

around 1 a.u.[85]. It is convenient to obtain the valence Compton profile for the amorphous carbon film as graphite in previous section. However, there is no experimental Compton profile for the amorphous carbon using photons. The electron Compton scattering technique provides a useful tool for studying the electron momentum distribution in amorphous materials.

4.4 Summary

Electron energy-loss near edge structure (ELNES) and electron Compton scattering from solids (ECOSS) were obtained from silicon (cubic crystal), natural graphite (hexagonal crystal) and amorphous carbon film (structureless) in the transmission electron microscope (TEM) by recording electron energy-loss spectroscopy (EELS) at different scattering angles. Therefore, both the ground states and unoccupied states of solids were studied in one experiment. Much shorter recording time for ECOSS measurements makes it possible to study the momentum transfer dependence of the Compton profile and Compton defect. The electron Compton profile from solids is in good agreement with other conventional Compton profile measurements, as well as with theory, thus establishing the validity of the technique.

Since we are interested in valence Compton profile, it requires calculating the core contribution to separate the valence Compton profile from the experimental results. Calculations of the core contributions were performed by Hartree-Slater method. Good agreements at both wings of the total Compton spectrum are found. The results in this thesis indicate that the Hartree-Slater method not only can be used to interpret the core edge shapes at low momentum transfer but also works well in Compton scattering region.

The difference of Compton profiles measured at two different crystallographic directions reflects the anisotropy of the electron momentum density distribution in a material under study. Anisotropy of the electron momentum distribution provides information about the behaviour of the valence electrons which is responsible for formation of the condensed phase of the material and its properties. Anisotropy measurements require a much higher statistical accuracy and resolution. In recent years, most high-resolution Compton scattering experiments based on synchrotron radiation sources have been devoted to study the anisotropies of profiles. The synchrotron-based Compton scattering experiment is long and expensive. The improvements in intensity, resolution and statistical accuracy of recent years make anisotropy measurements of electron Compton profile possible to carry out in the TEM. The Compton profiles of graphite were recorded in two directions in the anisotropy measurement. 3 spectra with an exposure time 55s each were acquired to give one spectrum with reasonable statistics and high signal-to-noise ratio. A significant anisotropy is found. The amplitude of anisotropy in our ECOSS experiment is smaller compared to previous measurements. This may be due to variations in tilt angle and thickness of sample, as well as mixing of in-plane and out-of-plane component via different scattering.

Chapter 5

Conclusions and Outlook

Electron energy-loss spectroscopy (EELS) has been studied both at small and large scattering angles. The momentum transfer dependence of the ELNES at relatively small scattering angles provides an opportunity to investigate all the unoccupied states. The Compton profile provides information about the momentum distribution of the electrons in the ground state. Therefore, both occupied and unoccupied states of a solid can be studied in one experiment by means of EELS measurements using the TEM. In addition to the EELS measurement, one obtains images, diffraction pattern as well as energy dispersive X-ray spectroscopy (EDX), each of them may be used to further examine the nature of the material.

It was demonstrated that Compton profiles from solids can be obtained in a time less than 1 min by means of electron energy-loss spectroscopy in the transmission electron microscope. The validity of this technique was confirmed by comparing the electron Compton scattering results with profiles using photon scattering. Time taken is the most striking difference, one electron Compton profile can be measured in minutes compared with hours or days using photons. The recording time was usually weeks and months with radioisotope. The high flux of synchrotron radiation reduces the passage of time to hours and days [95]. Short recording time opens up new possibilities for systematic studies.

The second advantage is resolution. The energy resolution of 2 eV (FWHM, zero loss peak) corresponds to a momentum resolution of approximately 0.01 a.u. Considering the collection conditions (such as beam divergence, collection angles, etc.) [34], the effective momentum resolution can be estimated to be of the order of 0.15 a.u. It is only possible to get such good momentum resolution for photon Compton profiles by using a synchrotron radiation source. However, TEM ECOS is much cheaper and more available than synchrotrons.

In addition, electron Compton profiles can be measured from nano- and micro-scale regions of a specimen in the transmission electron microscope. Obtaining high-precision Compton profile from microscopic solids with short exposure time opens up many possibilities for obtaining physical and chemical information. Notably, the Fourier transform of the electron momentum density distribution contains information on the phase of the ground state wavefunctions in real space [32].

In a typical Compton scattering experiment, the valence Compton profile is obtained only after the contribution from core electrons was subtracted. The results show that the Hartree-Slater method not only can be used to interpret the ionization edge but also works well in the Compton scattering region in the EELS measurement. The good agreement of the calculated core contribution at both wings of the total Compton spectrum also indicates the correctness of background subtraction in this experiment.

The enormous cross-section advantage of electron scattering rapidly diminishes as the momentum transfer increases above 14 a.u. [21]. Usually, we concentrate on spectra with energy loss below 2000 eV, which are more easily recorded by EELS. Therefore, for an available electron Compton scattering spectrum, the energy loss of the Compton peak should be no more than 1500 eV and be located far away from any core ionization edge. At the moment, we don't need to consider the beam damage problem as the measurement takes in such a short time. Perhaps the most serious problem associated with ECOSS is how to avoid the effect of Bragg diffraction. In this work we use a three-beam scattering geometry in order to suppress most of the subsidiary Compton profiles.

Compton scattering measurements can give valuable information about the electronic structure of matters due to the fact that the Compton profile is sensitive to the state of the valence electrons of the atoms which is responsible for the properties of solids. The Compton profile can be obtained in a very short time; this opens up new possibilities: systematic studies become feasible. For example, a series of Compton profiles can be obtained from graphite to graphene with decreasing layers to study the evolution of the valence electron momentum density distributions of the in-plane. Directional electron Compton profile measurements of single crystals give more information than measurements on gases, liquids and powder samples which obtain only the spherical average of the electron momentum density distributions. The anisotropy of directional ECOSS measurements from crystals will play an important role in the future in this field.

At the moment, an increasing number of transmission electron microscopes with aberration correctors, monochromators and new energy filters can be found in laboratories. ECOSS measurements based on these new instruments can be obtained with momentum resolution 0.1 a.u. or better. This is an important consideration in many Compton scattering experiments since this momentum resolution is generally needed for studying the Fermi momentum in Compton spectra [2]. In the TEM, EELS analysis can be coupled with structural analysis from electron diffraction pattern and composition analysis by energy dispersive X-ray spectroscopy (EDS or EDX) as well as high resolution images. These combined analyses can be carried out in one experiment, each of which may be used to give an important insight into the chemical and physical properties to better understand the nature of materials.

Bibliography

1. N. Zettili, *Quantum Mechanics Concepts and Applications*. Wiley, 2009.
2. P.E. Mijnarends and A. Bansil, "Scattering techniques, Compton" in Encyclopedia of condensed matter physics, edited by G.F. Bassani, G.L. Liedl, and P. Wyder. Elsevier, 2005.
3. M.J. Cooper, *Compton-Scattering and Electron Momentum Determination*. Reports on Progress in Physics, 1985. **48**(4): pp. 415-481.
4. A.H. Compton, *A quantum theory of the scattering of x-rays by light elements*. Physical Review, 1923. **21**(5): pp. 0483-0502.
5. A.H. Compton, *The spectrum of scattered x-rays*. Physical Review, 1923. **22**(5): pp. 0409-0413.
6. G.E.M. Jauncey, *Quantum theory of the intensity of the modified band in the compton effect*. Physical Review, 1925. **25**(6): pp. 723-736.
7. Du Mond, J.W.M., *Compton modified line structure and its relation to the electron theory of solid bodies*. Physical Review, 1929. **33**(5): pp. 0643-0658.
8. J.W.M. DuMond, *Breadth of compton modified line*. Physical Review, 1930. **36**(1): pp. 0146-0147.
9. J.W.M. DuMond, *The linear momenta of electrons in atoms and in solid bodies as revealed by x-ray scattering*. Reviews of Modern Physics, 1933. **5**(1): pp. 0001-0033.
10. W.A. Reed, *Comparison of Experimental Methods for Measuring Electron Momentum Distributions*. Acta Crystallographica Section A, 1976. **32**(1): pp. 676-690.
11. B.G. Williams, *Experimental-Determination of Electron Momentum Densities*. Physica Scripta, 1977. **15**(2): pp. 92-111.
12. S. Manninen, *Synchrotron-based Compton scattering studies*. Radiation Physics and Chemistry, 1998. **51**(4-6): pp. 481-486.
13. J.W.M. DuMond and H.A. Kirkpatrick, *A direct spectrum of the structure and shift of the Compton line with helium gas as the scatterer*. Physical Review, 1937. **52**(5): pp. 0419-0436.
14. J.F. Felsteiner and S. Kahane, *Compton profile anisotropy of graphite*. Physics Letters A, 1970. **33**: pp. 442-443.
15. P. Eisenber and W.A. Reed, *Gamma-Ray Compton-Scattering - Experimental Compton Profiles for He, N₂, Ar, and Kr*. Physical Review A, 1972. **5**(5): pp. 2085-2094.
16. M. Cooper, P. Pattison, and J.R. Schneider, *Compton Profile Measurements with 412 Kev Gamma-Radiation*. Philosophical Magazine, 1976. **34**(2): pp. 243-257.
17. P. Suortti, T. Buslaps, V. Honkimaki, N. Hiraoka, and U. Lienert, *Crystal spectrometers for Compton scattering studies*. Zeitschrift Fur Physikalische Chemie-International Journal of Research in Physical Chemistry & Chemical Physics, 2006. **220**(7): pp. 831-847.

18. S. Huotari, K. Hamalainen, S. Manninen, S. Kaprzyk, A. Bansil, W. Caliebe, T. Buslaps, H. V. and P. Suortti, *Energy dependence of experimental Be Compton profiles*. Physical Review B, 2000. **62**(12): pp. 7956-7963.
19. R. Verbeni, T. Pylkkanen, S. Huotari, L. Simonelli, G. Vanko, K. Martel, C. Henriquet, and G. Monaco, *Multiple-element spectrometer for non-resonant inelastic X-ray spectroscopy of electronic excitations*. Journal of Synchrotron Radiation, 2009. **16**(4): pp. 469-476.
20. S. Huotari, et al., *Momentum Distribution and Renormalization Factor in Sodium and the Electron Gas*. Physical Review Letters, 2010. **105**(8): p. 086403.
21. R.A. Bonham and H.F. Wellenstein, "Electron Scattering" in *Compton Scattering* edited by B.G. Williams. McGraw-Hill, 1977.
22. A.L. Hughes and M.M. Mann, *A new method for investigating atomic electron velocities*. Physical Review, 1938. **53**(1): pp. 50-63.
23. A.L. Hughes and M.A. Starr, *Atomic electron velocities in nitrogen and methane*. Physical Review, 1939. **55**(4): pp. 0343-0350.
24. A.L. Hughes and T. Enns, *The velocities of electrons in hydrocarbon bonds*. Physical Review, 1941. **60**(4): pp. 345-350.
25. B. Hicks, *The shape of the Compton line for helium and molecular hydrogen*. Physical Review, 1937. **52**(5): pp. 0436-0442.
26. W.E. Duncanson, *Momentum distribution in molecular systems Part VII. Momentum distribution and shape of the Compton line for Li-2 and N-2*. Proceedings of the Cambridge Philosophical Society, 1943. **39**: pp. 180-188.
27. H.F. Wellenstein and R.A. Bonham, *Compton-Scattering of High-Energy Electrons from Helium*. Physical Review A, 1973. **7**(5): pp. 1568-1572.
28. W.H.E. Rueckner, A.D. Barlas, and H.F. Wellenstein, *Electron Compton Defect Observed in He, H-2, D2, N2, and Ne Profiles*. Physical Review A, 1978. **18**(3): pp. 895-909.
29. A.L. Bennani, et al., *Measurement of Compton Profiles of CH₄ and C₂H₄ by High-Energy Electron-Impact Spectroscopy*. Chemical Physics Letters, 1976. **41**(3): pp. 470-473.
30. A.D. Barlas, W.H.E. Rueckner and H.F. Wellenstein, *Critical-Evaluation of High-Energy Electron-Impact Spectroscopy to Measure Compton Profiles*. Journal of Physics B-Atomic Molecular and Optical Physics, 1978. **11**(19): pp. 3381-3400.
31. J.M. Thomas, B.G. Williams and T.G. Sparrow, *Electron-Energy-Loss Spectroscopy and the Study of Solids*. Accounts of Chemical Research, 1985. **18**(11): pp. 324-330.
32. B.G. Williams, et al., *A New Approach to the Measurement of the Momentum Densities in Solids Using an Electron-Microscope*. Chemical Physics Letters, 1981. **78**(3): pp. 434-438.
33. R.F. Egerton,, *Electron Energy-Loss Spectroscopy in Electron Microscope*. Springer, 2011.
34. P. Jonas and P. Schattschneider, *The Experimental Conditions for Compton-Scattering in the Electron-Microscope*. Journal of Physics-Condensed Matter, 1993. **5**(39): pp. 7173-7188.

35. D.S. Su, P. Jonas and P. Schattschneider, *The Multiple-Scattering Problem in Electron Compton-Scattering on Solids*. Philosophical Magazine B, 1992. **66**(3): pp. 405-418.
36. D.S. Su and E. Zeitler, *Background Problem in Electron-Energy-Loss Spectroscopy*. Physical Review B, 1993. **47**(22): pp. 14734-14740.
37. P. Schattschneider, *Fundamentals of Inelastic Electron Scattering*. Springer-Verlag Wien, 1986
38. B.G. Williams, *Compton Scattering*. Springer, 1977.
39. P. Eisenberger and P.M. Platzman, *Compton Scattering of X-Rays from Bound Electrons*. Physical Review A, 1970. **2**(2): pp. 415-423.
40. B.G. Williams and R.F. Egerton, *Corrections to the Impulse Approximation for Use in Electron Compton-Scattering Experiments*. Chemical Physics Letters, 1982. **88**(1): pp. 95-97.
41. T.C. Wong, et al., *Compton Defects and Asymmetries in Free Atoms*. Physical Review A, 1982. **26**(1): pp. 181-185.
42. S.T. Manson, *Inelastic Collisions of Fast Charged-Particles with Atoms - Ionization of Aluminum L Shell*. Physical Review A, 1972. **6**(3): pp. 1013-1024.
43. R.D. Leapman, P. Rez, and D.F. Mayers, *K-Shell, L-Shell and M-Shell Generalized Oscillator-Strengths and Ionization Cross-Sections for Fast Electron Collisions*. Journal of Chemical Physics, 1980. **72**(2): pp. 1232-1243.
44. J.M. Auerhammer and P. Rez, *Dipole-Forbidden Excitations in Electron-Energy-Loss Spectroscopy*. Physical Review B, 1989. **40**(4): pp. 2024-2030.
45. R.D. Cowan, *The Theory of Atomic Structure and Spectra*. University of California Press, 1981.
46. C. Dwyer, *Multislice theory of fast electron scattering incorporating atomic inner-shell ionization*. Ultramicroscopy, 2005. **104**(2): pp. 141-151.
47. M.J. Cooper, P. Mijnen, N. Shiotani, N. Sakai and A. Bans, *X-ray of Compton Scattering*. Oxford University Press, 2004.
48. M.H. Krisch, et al., *Momentum transfer dependence of inelastic x-ray scattering from the Li K edge*. Physical Review Letters, 1997. **78**(14): pp. 2843-2846.
49. S. Löffler, I. Ennen, F. Tian, P. Schattschneider and N. Jaouen, *Breakdown of the dipole approximation in core losses*. Ultramicroscopy, 2011. **111**(8): pp. 1163-1167.
50. B.G. Williams, T.G. Sparrow and R.F. Egerton, *Electron Compton-Scattering from Solids*. Proceedings of the Royal Society of London Series a-Mathematical Physical and Engineering Sciences, 1984. **393**(1805): pp. 409-422.
51. D. Pearmain, *Electron Microscopy Characterisation of Size-Selected Pd Clusters and Industrial Pd Catalysts*. Thesis, University of Birmingham, 2011.
52. D.B. Williams and C.B. Carter, *Transmission Electron Microscopy : A Textbook for Materials Science*. New York: Springer, 2009.
53. A. Maigne, *How to optimize your EELS experiments by adjusting the collection angle of your spectrometer ?* Gatan,
http://www.gatan.com/resources/knowhow/kh19_eels.php.
54. P. Jonas, P., *Electron Compton Scattering in the Electron Microscope*. Thesis,

- Vienna University of Technology, 1993.
55. W.T. Scott, *Theory of Small-Angle Multiple Scattering of Fast Charged Particles*. Reviews of Modern Physics, 1963. **35**(2): pp. 231-313.
 56. A.V. Crewe and T. Groves, *Thick Specimens in Cem and Stem .1. Contrast*. Journal of Applied Physics, 1974. **45**(8): pp. 3662-3672.
 57. L. Reimer, *Calculation of the Angular and Energy-Distribution of Multiple Scattered Electrons Using Fourier-Transforms*. Ultramicroscopy, 1989. **31**(2): pp. 169-176.
 58. B.G. Williams, M.K. Uppal and R.D. Brydson, *Dynamic Scattering Effects in Electron-Scattering Measurements of the Compton Profiles of Solids*. Proceedings of the Royal Society of London Series a-Mathematical Physical and Engineering Sciences, 1987. **409**(1836): pp. 161-176.
 59. X.D. Weng, P. Rez, and P.E. Batson, *Single Electron Calculations for the Si L_{2,3} near Edge Structure*. Solid State Communications, 1990. **74**(9): pp. 1013-1015.
 60. J.O. Hansen, et al., *Studies of Nucleon Form Factors with 12 GeV CEBAF and SuperBigBite*. 19th Particles and Nuclei International Conference (Panic11), 2012. **1441**: pp. 162-164.
 61. M. Inokuti, *Inelastic Collisions of Fast Charged Particles with Atoms and Molecules - Bethe Theory Revisited*. Reviews of Modern Physics, 1971. **43**(3): pp. 297-&.
 62. J.T. Okada, et al., *Persistence of Covalent Bonding in Liquid Silicon Probed by Inelastic X-Ray Scattering*. Physical Review Letters, 2012. **108**(6): p.067402.
 63. A.G. Marinopoulos, et al., *Ab initio study of the optical absorption and wave-vector-dependent dielectric response of graphite*. Physical Review B, 2004. **69**(24): p. 245419.
 64. R.A. Rosenberg, P.J. Love and V. Rehn, *Polarization-Dependent C(K) near-Edge X-Ray-Absorption Fine-Structure of Graphite*. Physical Review B, 1986. **33**(6): pp. 4034-4037.
 65. P.E. Batson, *Carbon-1s near-Edge-Absorption Fine-Structure in Graphite*. Physical Review B, 1993. **48**(4): pp. 2608-2610.
 66. R.D. Leapman, P.L. Fejes, and J. Silcox, *Orientation Dependence of Core Edges from Anisotropic Materials Determined by Inelastic-Scattering of Fast Electrons*. Physical Review B, 1983. **28**(5): pp. 2361-2373.
 67. A.K. Geim and K.S. Novoselov, *The rise of graphene*. Nature Materials, 2007. **6**(3): pp. 183-191.
 68. D.S. Su and R. Schlogl, *Nanostructured Carbon and Carbon Nanocomposites for Electrochemical Energy Storage Applications*. ChemSusChem, 2010. **3**(2): pp. 136-168.
 69. S. Stankovich, et al., *Synthesis of graphene-based nanosheets via chemical reduction of exfoliated graphite oxide*. Carbon, 2007. **45**(7): pp. 1558-1565.
 70. J.C. Meyer, C. O. Girit, M. F. Crommie, and A. Zettl, *Hydrocarbon lithography on graphene membranes*. Applied Physics Letters, 2008. **92**(12): p. 123110.
 71. J.C. Meyer, et al. *Accurate Measurement of Electron Beam Induced Displacement Cross Sections for Single-Layer Graphene*. Physical Review Letters, 2012. **108**(19):

- p. 196102.
72. J.T. Titantah and D. Lamoen, *Technique for the $sp(2)/sp(3)$ characterization of carbon materials: Ab initio calculation of near-edge structure in electron-energy-loss spectra*. Physical Review B, 2004. **70**(7): p.075115.
 73. B.M. Kincaid, A.E. Meixner, and P.M. Platzman, *Carbon-K Edge in Graphite Measured Using Electron-Energy-Loss Spectroscopy*. Physical Review Letters, 1978. **40**(19): pp. 1296-1299.
 74. R.F. Klie, Y. Zhu, G. Schneider and J. Tafto, *Experimental probing of the anisotropy of the empty p states near the Fermi level in MgB₂*. Applied Physics Letters, 2003. **82**(24): pp. 4316-4318.
 75. N.D. Browning, J. Yuan and L.M. Brown, *Real-Space Determination of Anisotropic Electronic-Structure by Electron-Energy Loss Spectroscopy*. Ultramicroscopy, 1991. **38**(3-4): pp. 291-298.
 76. P. Schattschneider and A. Exner, *Progress in Electron Compton-Scattering*. Ultramicroscopy, 1995. **59**(1-4): pp. 241-253.
 77. U. Bonse and W. Schroder, *Compton Profile of Graphite Measured with 22.1 Kev Photons and Solid-State Detector*. Physica Status Solidi a, 1974. **23**(1): pp. 297-301.
 78. R. Tyk, et al., *Compton-Profile Anisotropies in Graphite and Hexagonal Boron-Nitride*. Physical Review B, 1985. **32**(4): pp. 2625-2627.
 79. P.M. Bergstrom and R.H. Pratt, *An overview of the theories used in Compton scattering calculations*. Radiation Physics and Chemistry, 1997. **50**(1): pp. 3-29.
 80. W.A. Reed, et al., *Electron Momentum Distributions in Graphite and Diamond and Carbon-Carbon Bonding*. Physical Review B, 1974. **10**(4): pp. 1507-1515.
 81. T. Ohata, et al., *High-resolution Compton scattering study of the electron momentum density in Al*. Physical Review B, 2000. **62**(24): pp. 16528-16535.
 82. M. Brancewicz, et al., *A need for high-resolution Compton scattering study of hcp metals with the use of synchrotron radiation*. Nuclear Instruments & Methods in Physics Research Section B-Beam Interactions with Materials and Atoms, 2007. **255**(2): pp. 395-398.
 83. M. Brancewicz, et al., *Electron momentum density of hexagonal magnesium studied by high-resolution Compton scattering*. Radiation Physics and Chemistry, 2009. **78**: pp. 137-139.
 84. C. Pisani, et al., *Anisotropy of the electron momentum distribution in alpha-quartz investigated by Compton scattering and ab initio simulations*. Physical Review B, 2011. **84**(24): p. 245102.
 85. M.J. Cooper and J.A. Leake, *Compton Profiles of Graphite and Diamond*. Philosophical Magazine, 1967. **15**(138): pp. 1201-1212.
 86. R.J. Weiss and W.C. Phillips, *X-Ray Determination of Electron Momentum Density in Diamond Graphite and Carbon Black*. Physical Review, 1968. **176**(3): pp. 900-904.
 87. R. Tyk, J. Felsteiner and I. Gertner, *Compton Profile Anisotropies in Hexagonal Boron-Nitride and Graphite*. Acta Crystallographica Section A, 1984. **40**: p. 169.
 88. J. Diaz, O.R. Monteiro and Z. Hussain, *Structure of amorphous carbon from near-edge and extended x-ray absorption spectroscopy*. Physical Review B, 2007.

- 76(9): p. 094201.
89. J. Robertson, *Amorphous-Carbon*. Advances in Physics, 1986. **35**(4): pp. 317-374.
 90. J.T. Titantah and D. Lamoen, *sp(3)/sp(2) characterization of carbon materials from first-principles calculations: X-ray photoelectron versus high energy electron energy-loss spectroscopy techniques*. Carbon, 2005. **43**(6): pp. 1311-1316.
 91. J. Diaz, et al., *Analysis of the pi* and sigma* bands of the x-ray absorption spectrum of amorphous carbon*. Physical Review B, 2001. **64**(12): p. 125204.
 92. R. Gago, et al., *Evolution of sp(2) networks with substrate temperature in amorphous carbon films: Experiment and theory*. Physical Review B, 2005. **72**(1): p. 014120.
 93. S.D. Berger, D.R. McKenzie, and P.J. Martin, *EELS Analysis of Vacuum Arc-Deposited Diamond-Like Films*. Philosophical Magazine Letters, 1988. **57**(6): p. 285-290.
 94. A.J. Papworth, et al., *Electron-energy-loss spectroscopy characterization of the sp(2) bonding fraction within carbon thin films*. Physical Review B, 2000. **62**(19): p. 12628-12631.
 95. M.J. Cooper, *Chapter 1 in X-Ray Compton Scattering*. Oxford University Press, 2004.

Acknowledgements

First of all, I would like to thank my supervisor Prof. Peter Schattschneider for providing the opportunity to do this work at Vienna University of Technology. Prof. Schattschneider has walked me through all stages of this thesis. Without his instructions, this thesis would not have been possible. I also would like to thank him for providing help for my wife came to Vienna last year.

Many thanks to Prof. Dangsheng Su who introduced me to Prof. Schattschneider. He also gave me advice and suggestions when I wrote this thesis.

Special thanks and gratitude go to Dr. Stefan Löffler for all of the time that he has spent giving advice and assistance with works.

I would like to thank everyone at the USTEM. Special thanks goes to: Prof. Johannes Bernardi and Dr. Michael Stöger-Pollach for their patient TEM training and continual help in TEM operations; Gruber Jakob and Gamerith Thomas for their assistance in TEM sample preparation.

Further, I am very grateful for the help from Prof. Jannic C. Meyer and his student Franz Eder who taught me graphite sample preparation.

In the end, I thank my parents for their constant support and love. I also wish extend my thanks to my parents in-law for their devotedly taking care of my wife and son. I want to express my special thanks to my wife Zhang Xiaoyan, I would like to thank you deep in my heart for giving me the biggest support I could get. Finally, I thank my little son for giving me lots of happiness from his cute smile.

Curriculum Vitae

Name: Zhenbao Feng

Sex: Male

Birth: Oct. 06, 1982

Nationality: P.R. China

E-mail: zbfeng@imr.ac.cn

Education and Experience

- 2002-2006 Bachelor of Science in Physics Education at Liaocheng University, Liaocheng, P.R. China.
- 2006-2009 Master of Science in Optics at Liaocheng University, Liaocheng, P.R. China.
- 2009-2010 Ph.D. at Institute of Metal Research, Chinese Academy of Sciences, Shenyang, P.R. China.
- 2010-2013 Ph.D. at Institute of Solid State Physics, Vienna University of Technology, Vienna, Austria.

International Conferences

1. The 15th European Microscopy Congress (EMC2012), September 16th to 21th, 2012, Manchester, United Kingdom.
Poster: **Z. Feng**, S. Löffler, D.S. Su and P. Schattschneider, *Determination the position of the Compton scattering in electron energy-loss spectroscopy*.
2. The 2nd International Symposium on Advanced Electron Microscopy for Catalysis and Energy Storage Materials (EMCAT 2012), February 5th to 8th, 2012, Berlin, Germany.
3. The 3rd International Conference on Theoretical Chemistry, Molecular Modeling and life science, October, 2007, Yantai, China.

Peer-Reviewed Publications:

1. **Z. Feng**, S. Löffler, F. Eder, D.S. Su, J.C. Meyer and P. Schattschneider, *Combined study of the ground and unoccupied electronic states of graphite by electron energy-loss spectroscopy*. Journal of Applied Physics, 2013. **114**(18): p.183716.
2. **Z. Feng**, H. Hu and S. Cui, *First-principles study of electronic structure, chemical bonding, and optical properties of cubic SrHfO₃*. Journal of Physics and Chemistry of solids, 2009. **70** (2): p. 412-416.
3. **Z. Feng**, H. Hu and S. Cui, *First-principles study of optical properties of SrZrO₃ in cubic phase*. Solid State Communications, 2008. **148** (9): p. 472-475.

